Perfusion, Oxygenation and Vascular Architecture of Gliomas

Noninvasive Evaluation of Tumor Physiology by Magnetic Resonance

Boudewijn P.J. van der Sanden

Cover: A ^{1}H-MR image of the 2D distribution of the Gd_DTPA concentration and an immunohistochemical image of the distribution of perfused microvessels (blue structures) and chronically hypoxic cells (green structures) in a 9L-glioma growing in a rat brain. In the center of the representation a Gd_DTPA-uptake curve and a ^{31}P-MR spectrum are shown.

Perfusion, oxygenation and vascular architecture of gliomas

Noninvasive evaluation of tumor physiology by magnetic resonance

Een wetenschappelijke proeve op het gebied van de
Medische Wetenschappen.

Proefschrift

ter verkrijging van de graad van doctor
aan de Katholieke Universiteit Nijmegen,
volgens besluit van het College van Decanen
in het openbaar te verdedigen op
maandag 21 juni 1999
des namiddags om 1.30 precies

door

Boudewijn Petrus Johannes van der Sanden

geboren op 23 februari 1965, te Tilburg

II

Promotoren

Prof. Dr. A. Heerschap
Prof. Dr. A.J. van der Kogel

Manuscriptcommissie

Prof. Dr. F. Corstens (voorzitter)
Prof. Dr. J.O. Barentsz
Dr. W.M.M.J. Bovée   Technische Universiteit Delft

Haast je niet door het leven,
geniet van elke dag,
want zijde kan eindigen in rafels.

(Cesaria Evora en dit proefschrift)

Voor Nathalie

Aan al mijn docenten
To all my teachers

List of abbreviations and symbols

$Area_{100}$: Nonperfused area fraction at a distance > 100 µm from
a nearest perfused vessel (-)

ADC : Apparent diffusion coefficient ($cm^2. s^{-1}$)

ADC_w : Apparent diffusion coefficient of water ($cm^2. s^{-1}$)

ATP : Adenosine triphosphate

D_2O : Deuterium oxide

DPF : Differential Path length Factor (-) (= related to scattering properties
of tissue, see NIRS experiments in Chapter 7)

EPI : Echo planar imaging

FID : Free induction decay

FLASH : Fast low angle shot imaging

FOV : Field of view

Gd : Gadolinium diethylenetriaminepenta acetic acid (Gd_DTPA)

HDO : Deuterated water, which results from proton-deuteron exchange with
D_2O

[HHb] : Deoxyhemoglobin concentration (mM)

icd : Intercapillary distance (µm)

icd_{200} : Intercapillary distance larger than 200 µm

k : Tracer-uptake rate constant (s^{-1})

MRS : Magnetic resonance spectroscopy

MRI : Magnetic resonance imaging

NIRS : Near Infrared spectroscopy

NITP : N-Imidazole-theophylline (bioreductive chemical probe)

NS : Number of scans

N_p : Perfused capillary density (no. mm^{-2})

NTP : Nucleoside triphosphates: adenosine -, guanosine -, uridine - and cytidine
triphosphate. ^{31}P-MRS cannot distinguish these nucleoside triphosphates,
because the phosphate groupes are all equivalent. Approximately 90 % of the
NTP signal in ^{31}P-MR spectra is due to the contribution of ATP

[O_2Hb] : Oxyhemoglobin concentration (mM)

ROI : Region of interest

P : Permeability of capillary endothelium (cm. s^{-1})

PCr : Phosphocreatine

PDE : Phosphodiesters

pH_e : Extracellular pH

pH_i : Intracellular pH

pH_{blood} : pH of blood

pH_{mrs} : pH as determined by ^{31}P-MRS (= intracellular pH)

P_i : Inorganic phosphate

P_i/NTP : Inorganic phosphate to nucleoside triphosphates ratio. Cells with a high
P_i/NTP ratio or low bioenergetic status have difficulties to maintain a steady
state NTP level

PIMO : Pimonidazole hydrochloride (bioreductive chemical probe)

PFC : Perfluorocarbon compound

PME : Phosphomonoesters

pCO_{2blood}	: Carbondioxide tension in blood (mmHg)
pO_{2blood}	: Oxygen tension in blood (mmHg)
$pO_{2electrode}$	: Oxygen tension in tissue as measured by O_2-electrodes (polarography) (mmHg)
$pO_{2relaxo}$	: Oxygen tension in tissue as measured by ^{19}F-MR relaxometry (mmHg)
$pO_{2tissue}$	: Oxygen tension in tissue (mmHg)
PS	: Permeability surface-area product (ml. s^{-1})
R_1	: Spin-lattice relaxation rate $(1/T_1)$ (s^{-1})
SaO_2	: Hemoglobin saturation (%)
SI	: Signal Intensity
SI_{pre}	: Signal Intensity before bolus adminstration of contrast agent
SI_{post}	: Signal Intensity after bolus administration of contrast agent
T_1	: Spin-lattice relaxation time (s)
T_2	: Spin-spin relaxation time (s)
T_2*	: Apparent spin-spin relaxation time (s)
TBP	: Tumor blood perfusion (ml. s^{-1})
t_{difmax}	: Maximum diffusion time (s)
TE	: Echo time
TR	: Repetition time
[tHb]	: Total hemoglobin concentration (= $[O_2Hb]$ + [HHb]) (mM)
V_e	: Extracellular volume (ml)
V_d	: Distribution volume of a contrast agent (ml)
V_v	: Vascular volume (ml)
VOI	: Volume of interest

VI

Contents

Chapter 1

Introduction and outline thesis

1.1   Physiological profiles of tumors and radiosensitivity

The physiological profile of a tumor is a term that groups different physiological parameters such as tumor blood perfusion, oxygenation status, pH of different blood and tissue compartments, and the bioenergetic status of tumor cells. But also information on the morphology of the vascular architecture is a crucial part of the physiological profile. The outcome of an anti-cancer therapy depends on the specific physiological profile of a tumor, and therefore the sensitivity of a tumor for a therapy is unique. In radiotherapy, tumor response to treatment depends among others on the local oxygen tension and indirectly on the supply of oxygen via blood perfusion. Poor supply of oxygen causing hypoxia is associated with treatment failure following radiation therapy. In the development of new treatment strategies and protocols, new methods for predicting the best treatment modality for the individual patient will help the therapist in his choice of specific protocols before the start of a therapy (prediction phase). In the last few years, magnetic resonance methods have become available, which can be used to measure different parameters of the tumor physiology (1-4). Most of these magnetic resonance techniques are noninvasive and can be performed on clinical magnetic resonance imaging (MRI) scanners.

The aim of the studies presented in this thesis is to evaluate and apply magnetic resonance techniques in the characterization of physiological profiles of gliomas (primary brain tumors) before the start of radiotherapy. This approach is applicable to various tumor types, but here we focus on gliomas, because these are among the most radioresistant tumors (5).

Radiotherapy is based on the interaction of ionizing radiation with molecules of which the tissue is composed. This interaction may lead to ionization and/or excitation of atoms followed by breakage of chemical bounds. These broken molecules or free radicals are highly reactive and they engage in a succession of reactions that eventually leads to the restoration of electronic charge equilibrium. During this succession of reactions, DNA is one of the target molecules of interest. A majority of DNA can be successfully repaired by enzymes, but some DNA repair may fail, which can lead to cell death. Most of the free radicals are produced from water, since 70 % to 80 % of the molecules in the cell is water. In the presence of oxygen, a free radical $R\bullet$ can react with O_2 to produce $RO_2\bullet$, which then undergoes further reaction ultimately to yield $ROOH$ in a target molecule. This causes a change in the chemical composition of the target and makes the damage permanent. In the absence of O_2, the free radical $R\bullet$ reacts mainly with protons of water and restores its original form. The importance of oxygen for a permanent damage to cell structures during irradiation was shown in experiments on cell cultures and solid tumors (6,7). Hypoxic cells are up to three times more radioresistant than well-oxygenated cells (6). The cell-surviving fraction decreased faster under oxic conditions than under hypoxic conditions as a function of the radiation dose. Thus, the oxygen tension in tumor tissue is one of the physiological parameters that determine the sensitivity of a tumor to radiotherapy. Therefore the introduction of noninvasive methods to measure oxygen tensions and physiological parameters related to tissue oxygen tension would be very valuable before the start of radiotherapy, and also to evaluate proposed therapy improvements.

Figure 1.1 shows different physiological parameters, which determine the oxygen tension in tissue. The regional and global oxygen tension in tissue is the result of a balance between O_2 supply and O_2 demand of cells (8). The O_2 supply depends among others on the tumor blood perfusion (8) and the oxyhemoglobin concentration in red blood cells of arterial blood and capillaries (8). In well-perfused capillaries, the oxygen carrier hemoglobin releases O_2 in tissue, which is influenced by the pH and oxygen tensions of the tumor microenvironment (8, 9). In the extravascular volume, $pO_{2tissue}$ gradients pertinent to perfused capillaries occur, which decrease monotonically until hypoxic values (< 5 mmHg) (10, 11) (see also chapter 6, Fig. 6.6). The length of these gradients depends on O_2-diffusion coefficients and O_2-consumption rates of tumor cell populations. Tumor cells beyond these O_2-gradients are regarded as chronically hypoxic (6, 12). These cells appear at the edge of necrotic cords (see chapter 3, Fig. 3.1 and 3.2). In chronically hypoxic regions, substrates (glucose, glutamine) for an anaerobic energy metabolism may still be supplied, but will run out by an intensified energy metabolism for the generation of ATP to maintain cell homeostasis. From the physiological and biochemical processes mentioned above, it can be deduced that tumors with an important fraction of large intercapillary distances may develop large populations of chronically hypoxic cells and necrotic areas. In addition, some microvessels transiently open and close in such a way that hypoxic regions may appear acutely (13, 14).
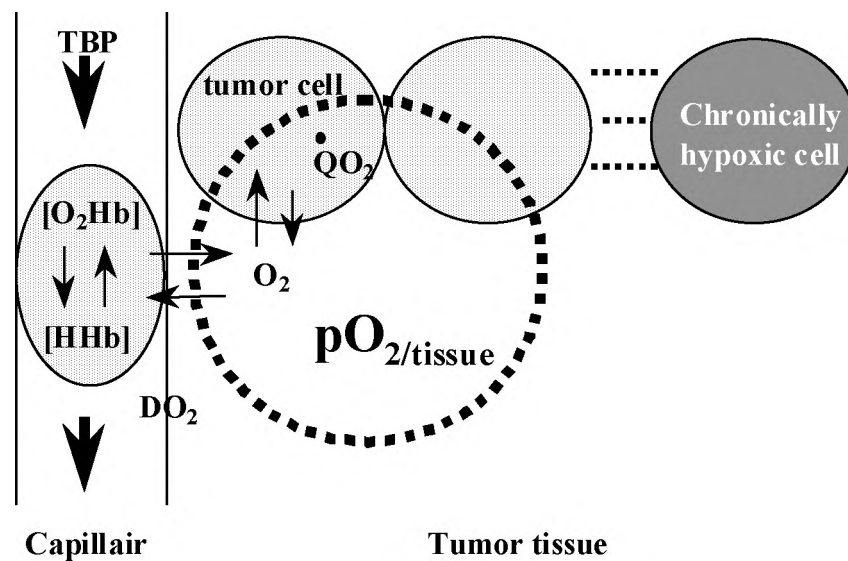
Figure 1.1 Summary of different physiological parameters, which affect the oxygen tension in tissue ($pO_{2/tissue}$): Tumor blood perfusion (TBP), oxyhemoglobin concentration [O_2Hb] in red blood cells, diffusion of oxygen across the vascular endothelium and in the extravascular volume (DO_2), the oxygen consumption rates of the tumor cells (QO_2). A combination of the latter parameters determines the critical O_2 diffusion distances pertinent to perfused vessels in tumor tissue. Beyond these distances, tumor cells are regarded as chronically hypoxic.

1.2   Outline of thesis

Most of the physiological and biochemical parameters, related to tissue oxygenation, can be assessed by magnetic resonance techniques. The MR-techniques and other methods used in this thesis for that purpose are summarized in Figure 1.2. A basic new experimental approach in these studies was to relate the MR-results to quantitative (immuno)histochemical analyses of the (functional) vascular architecture, the distribution of hypoxic cells and necrotic areas. The latter analyses permits the validation and characterization of MR-methods, and vice versa morphometric parameters of the vascular architecture and/or histological appearance of a tumor can be related to dynamic and noninvasive MR-studies of physiological and biochemical processes.

Most studies described in this thesis were performed on human glioma xenografts: surgical specimens of primary human gliomas (glioblastoma multiforme) were transplanted as xenografts in immuno-suppressed nude mice (15). The idea behind this approach was to maintain as close as possible a link with the original human tumor. Several glioma cell lines of human origin showed subcutaneous and intracerebral tumor growth retaining the morphological and cytogenetic characteristics of the original tumors (16). However, the development of the vasculature (angiogenesis) in human glioma xenografts is probably different, since the new microvessels originate from the host vessels of mouse tissue.
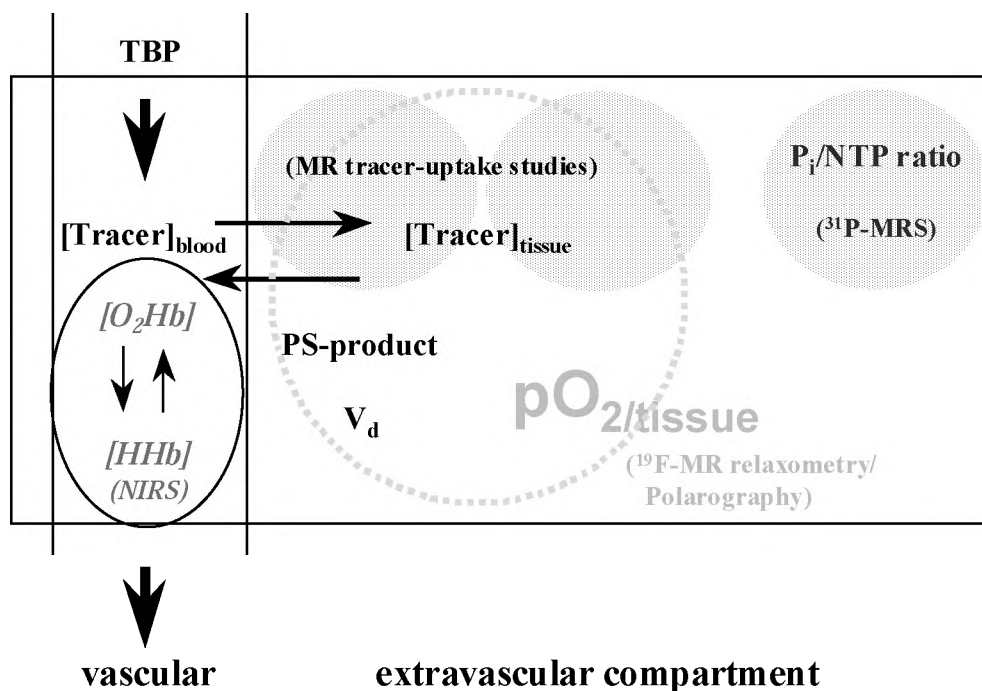

Figure 1.2 Summary of different MR and other methods, which have been used in this thesis to assess the physiological parameters of Figure 1.1. The five different methods and abbreviations represented in this figure, are explained in the text hereafter.

The tumor blood perfusion (TBP) was measured by tracer-uptake studies. In this thesis, two different tracers were used: the *freely diffusible* tracer HDO and the *diffusible* paramagnetic contrast-agent gadolinium (Gd). In previous studies, the uptake rate of HDO in tumor tissue was assumed to be limited by perfusion (17, 18), which makes this tracer a good candidate for TBP measurements. However, with respect to toxicity and MR-sensitivity, it seems unlikely that this tracer can be used for clinical purposes (19). Therefore, the use of the clinical contrast-agent Gd was explored in addition to HDO (20-23). During the research describes in this thesis, we became aware that the relation between tracer-uptake rates in tumor tissue and tumor blood perfusion was equivocal. The tracer-uptake rates were more related to parameters of the functional vascular bed in a tumor, such as the perfused vasular density, distribution, the vasular permeabilty (P) and the total surface area of the perfused blood vessel (S). The P and S factor are often taken together as the permeability surface-area product (PS-product), which determines the diffusive transport across the capillary endothelium. Furthermore, the distribution volume in the extravascular space (V_d) plays a role, since the latter determine the time to reach equilibrium between the tracer concentration in the vessels and the extravascular compartment. When V_d is large, the time for equalization of the tracer concentration may be considerable (Figure 1.2 and chapter 2). **In chapter 2,** different pharmacokinetic models will be discussed, which have been used to relate the uptake rates of HDO and Gd in tumor tissue to these physiological and vascular parameters. The content of this chapter permits a better understanding of chapters 3 and 4. **In chapter 3,** fast dynamic Gd-uptake MRI studies with a high spatial and temporal resolution in 9L-glioma growing in rat brain are presented. Gd-uptake rates were spatially correlated to morphometric parameters of the perfused vascular architecture, such as the perfused microvessel density (N_p) and vascular surface-area (S_p). The latter parameter was supposed to determine among other parameters as TBP and microvessel permeability (P), the Gd-uptake rate in perfused regions of the tumor (20). In addition to tracer-uptake experiments with the *diffusible* tracer Gd, changes in the concentration of *freely diffusible* HDO in the whole extravascular tumor volume (global) were analyzed in two subcutaneous human glioma xenografts with a different perfused vascular architecture **(chapter 4)**. The diffusion of HDO across the vascular endothelium and in the extravascular space is supposed to be fast, and not to be hindered by the vascular permeability and morphological or physiological characteristics of the extracellular matrix. Therefore it is assumed that global HDO-uptake is perfusion-limited. This assumption was tested for our glioma xenografts in chapter 4. The in vivo studies were substantiated in HDO-uptake studies on 2D in vitro models. In these models, perfusion rates and morphometric parameters of the perfused capillaries as distribution and permeability were well defined, which make a comparison between these parameters and HDO-uptake rates possible.

The oxygen tension in tumor tissue ($pO_{2/tissue}$) was probed with ^{19}F-MR relaxometry using perfluoro-15-crown-5-ether (perfluorocarbon compound) as oxygen sensor (2, 24) (Figure 1.2 and **chapter 5**). ^{19}F-MR relaxometry is a noninvasive method, which permits the determination of local or global oxygen tensions in tumors independent of the location of the tumor. Most alternative methods for the measurement of tissue oxygen tensions are invasive and limited to superficial tumors.

^{19}F-MR relaxometry is based on the linear relationship between spin-lattice relaxation rates of ^{19}F-spins of perfluorocarbon compounds and the local oxygen tension ($pO_{2/tissue}$). **In chapter 5,** the oxygen tension values obtained by this method were compared to

polarography (Eppendorf O_2-electrode measurements). Polarography is the most frequently used technique for direct measurements of local oxygen tension in (tumor) tissue (25, 26), however, this technique is invasive and studies of deep tumors are only possible with surgery. Thus, alternative methods are worthwhile and may be used in the prediction phase to test treatment modalities (chapter 7).

The bioenergetic status of a tumor is related to the supply of oxygen and nutrients for the energy metabolism of tumor cells. The P_i/NTP ratio is a measure of the bioenergetic status, and can be detected by ^{31}P-MR spectroscopy. NTP is an abbreviation for nucleoside triphosphates, which serve as principal donors of free energy in biological systems. A large amount of free energy is liberated when NTP is hydrolyzed to nucleoside diphosphates (NDP) and inorganic phosphate (P_i). When the concentration of P_i is high relative to the NTP concentration, the bioenergetic status of a cell or tissue is low. The latter may occur when the diffusion-limited supply of oxygen and nutrients to tumor cells at a distance from perfused microvessels is insufficient. In **chapter 6**, the P_i/NTP ratio of the same heterogeneously and homogeneously perfused tumor lines of chapter 4, was related to the distribution of distances between perfused capillaries using (immuno)histochemical analyses of the perfused vascular architecture. When the distance between functional microvessels increases, it is expected that the diffusion-limited supply of oxygen and nutrients decreases simultaneously and influences the bioenergetic status of the tumor.

Apart from characterizing the physiological profile of tumors, advanced MR-methods may also be used to evaluate proposed modifications of these profiles for improved treatments.
For instance, **in chapter 7**, MR-techniques were used to evaluate the effects of carbogen breathing on the physiological profile of gliomas. Carbogen is a gas mixture of 5 % CO_2 and 95 % O_2, which has been introduced to reduce hypoxia in tumors (13, 27). The ultimate effect of carbogen breathing on tumor physiology evolves from changes in multiple processes and varied in different experimental and human tumors (28, 29). Thus, the effect can only be understood when all relevant physiological parameters are taken into account. Near infrared spectroscopy (NIRS) was used to investigate relative changes in oxy- and deoxyhemoglobin concentrations in tumors (= Blood Oxygen Level Dependent (BOLD) effect) (30). Similar studies are possible with functional MRI methods (3), but the separation of perfusion and BOLD effects on signal intensity changes was impossible until recently (31). Oxygen tension changes in tumor tissue were evaluated by ^{19}F-MR relaxometry (as described in **chapter 5**), and possible modifications of tumor blood perfusion (TBP) were analyzed by fast dynamic [1]H-MR imaging of Gd-uptake (see **chapter 3**). Finally, changes of the bioenergetic status and pH of tumor cells were analyzed by ^{31}P-MRS (see also **chapter 6**). If carbogen-breathing results in an extension of the tissue volume supplied with oxygen, then the P_i/NTP ratio of tumor cells may decrease due to enhanced oxidative energy metabolism. Further, changes in the intracellular pH of tumor cells (pH_{mrs}) may correlate with changes in energy metabolism (32).

Chapter 8 provides a summary of this work.

References

1. Pass TJ, Bluemke DA, Siegelman SS. Tumor angiogenesis: Tutorial on implications for imaging. *Radiology* **203**: 593-600 (1997).

2. Hunjan S, Mason RP, Constantinescu A, Peschke P, Hahn EW, Antich PP. Regional tumor oximetry: ^{19}F NMR spectroscopy of hexafluorobenzene. *Int J Radiat Oncol Biol Phys* **41(1)**: 161-171 (1998).

3. Van Zijl PCM, Eleff SM, Ulatowski JA, Oja JME, Ulu AM, Traystman RJ, Kauppinen RA. Quantitative assessment of blood flow, blood volume and blood oxygenation effects in functional magnetic resonance imaging. *Nature Medicine* **4(2)**: 159-167 (1998).

4. Certaines de JD, Larsen VA, Podo F, Carpinelli G, Briot O, Henriksen O. Review paper: In vivo ^{31}P-MRS of experimental tumours. *NMR Biomed* **6**: 345-365 (1993).

5. Taghian A, Gioioso D, Budach W, Suit H. In vitro split-dose recovery of glioblastoma multiforme. *Radiation Res* **134**: 16-21 (1993).

6. Hall EJ. Radiobiology for the Radiologist (3th Ed), Philadelphia, Pa.: Lippincott 1988; 138-160.

7. Deacon J, Peckman MJ, Steel GG. The radioresponsiveness of human tumours and the initial slope of the cell survival curve. *Radiotherapy and Oncology* **2**: 317-323 (1984).

8. Gulledge CJ, Dewhirst MW. Tumor oxygenation: A matter of supply and demand. *Anticancer Res* **16**: 7741-750 (1996).

9. Stryer L. Biochemistry (2nd Ed.), Pa: Freeman WH, New York, San Fransisco, p. 69-70 (1983).

10. Helmlinger, G, Yuan, F, Dellian, M, Jain, RK. Interstitial pH and pO_2 gradients in solid tumors in vivo: High-resolution measurements reveal a lack of correlation. *Nature Med* **3(2):** 177-182 (1997).

11. Groebe K, Vaupel P. Evaluation of oxygen diffusion distances in human breast cancer xenografts using tumor-specific in vivo data: role of various mechanisms in the development of tumor hypoxia. *Int J Radiat Oncol Biol Phys* **15**: 691-697 (1988).

12. Horsman MR, Overgaard J. The oxygen effect in: " Basic Clinical Radiobiology, G. Gordon Steel (ed.) Edward Arnold Publishers, London Boston Sydney, Auckland, p. 81-88 (1993).

13. Chaplin DJ, Horsman MR, Aoki DS. Nicotinamide, Fluosol DA and Carbogen: A strategy to reoxygenate acutely and chronically hypoxic cells in-vivo. *Br J Cancer* **63**: 109-113 (1991).

14. Denekamp J. Review article: Angiogenesis, neovascular proliferation and vascular pathophysiology as targets for cancer therapy. Br J Radiology **66(783):** 181 – 195 (1993).

15. Bernsen HJJA, Rijken PFJW, Oostendorp T, van der Kogel. Vascularity and perfusion of human glioma xenografted in the athymic nude mouse. *Br J Cancer* **71(4):** 721-726 (1995).

16. Keuken JWM, Sprenger HE, Wesseling P, Bernsen HJJA, Suijkerbuijk RF, Roelofs F, Macville MVE, Gilhuis HJ, van Overbeeke JJ, Boerman RH. Xenografts genetically reflect glioblastoma biopsies: Characterization of 11 glioblastoma xenograft lines by comparative genomic hybridization. Submitted for publication in J. Neurosurgery, 1999.

17. Neil JF. The validation of freely diffusible tracer methods with NMR detection fpr measurements of blood flow. *Mag Res Med* **19**: 299 - 304 (1991).

18. Evelhoch JF. Tracer measurements of blood flow, in "NMR in physiology and biomedicine" (R.J. Gillies, Ed), Pa.: Academic press, San Diego: p.209-220 (1994).

19. Evelhoch JF. Measurement of tumor blood flow by deuterium NMR and the effects of modifiers. *NMR in Biom* **5**: 290 - 295 (1992).

20. Larsson HBW, Stubgaard M, Frederiksen JL, Jensen M, Henriksen O, Paulson OB. Quantitation of blood-brain barrier defect by magnetic resonance imaging and gadolinium-DTPA in patients with multiple sclerosis and brain tumors. *Mag Res Med* **16**: 177-131 (1990).

21. Tofts PS, Kermode AG. Measurement of the blood-brain barrier permeability and leakage space using dynamic MR imaging. 1. Fundamental concepts. *Mag Res Med* **17**: 357-367 (1991).

22. Larsson HBW, Tofts PS. Measurements of blood-brain barrier permeability using dynamic Gd_DTPA scanning – A comparison of methods. *Mag Res Med* 24: 174-176 (1992).

23. Degani H, Gusis V, Weinstein D, Fields S, Strano S. Mapping pathophysiological features of breast tumors by MRI at high spatial resolution. *Nature Med* **3(7)**: 780-782 (1997).

24. Dardzinski BJ, Sotak CH. Rapid tissue oxygen tension mapping using ^{19}F inversion-recovery echo-planar imaging of perfluoro-15-crown-5-ether. *Mag Res Med* **32**: 88-97 (1994).

25. Nozue M, Lee I, Hartford A, Tanda S, Suit HD, Jain RK. PO_2 measurent in murine tumors by Eppendorf histograph: Calibration, reproducibility and comparison with diamond-general device. *Int J Oncol* **9**: 955-962 (1996).

26. Kallinowski F, Zander R, Hoeckel M, Vaupel P. Tumor tissue oxygenation as evaluated by computerized-pO$_2$-histography. *Int J Radiat Oncol Biol Phys* **19**: 953-961 (1990).

27. Honess DJ, Bleehen NM. Perfusion changes in the RIF-1 tumor and normal tissues after carbogen and nicotinamide, individually and combined. *Br J Cancer* **71**: 1175-1180 (1995).

28. Robinson SP, Rodrigues LM, Ojugo ASE, McSheehy PMJ, Howe FA, Griffiths JR. The response to carbogen breathing in experimental tumor models monitored by gradient-recalled echo magnetic resonance imaging. Br J Cancer **75(7):** 1000 – 1006 (1997).

29. Griffiths JR, Taylor NJ, Howe FA, Saunders MI, Robinson SP, Hoskin PJ, Powell MEB, Thoumine M, Caine LA, Baddeley H. The response of human tumors to carbogen breathing, monitored by gradient-recalled echo magnetic resonance imaging. *Int J Radiat Oncol Biol Phys* **39(3):** 697-701 (1997).

30. Chance B, Borer E, Evans A, Holtom G, Kent J, Maris M, McCully K, Northrop J, Shinkin M. Optical and nuclear magnetic resonance studies of hypoxia in human tissue and tumors. *NY Acad Sci* **551**: 1-16 (1986).

31. Kim SG. Quantification of relative cerebral blood flow change by flow-sensitive alternating inversion recovery (FAIR) technique: Application to functional mapping. *Mag Res Med* **34**: 293-301 (1995).

32. Dobson GP, Yamamoto E, Hochachka PW. Phosphofructokinase control in muscle: nature and reversal of pH-dependent ATP inhibition. *Am J of Physiology* **250**: R71-R76 (1986).

Chapter 2

Pharmacokinetic models for the interpretation of diffusible tracer-uptake in tissue.

Boudewijn P.J. van der Sanden

2.1   Introduction

In the context of a tumor therapy, it is important to know how efficiently blood is providing oxygen, nutrients and drugs to tumor tissue and how effective it is in removing waste products from that tissue. The supply to tissue depends on physiological processes such as: blood transport or blood perfusion rates in the vascular compartment, the transport across the vascular endothelium and finally, the diffusion from regions adjacent to perfused vessels into nonperfused regions of the tissue (for review see 1-3). The uptake rate of diffusible tracers in the extravascular volume is related to these processes and therefore this parameter may indirectly provide information on the oxygen, nutrient and drug supply in tissue. The problem is, however, how to correlate tracer-uptake rates directly to one or more of these physiological processes. In chapter 3 and 4 detailed information on the perfused vascular architecture is given, which may help to solve this problem. If tracer-uptake rates can be related to physiological parameters, then they may be used more efficiently as a prognostic tool before or during the monitoring of a therapy (4-7).

Different pharmacokinetic models have been developed to relate global or regional tracer-uptake rates to physiological parameters (8-10). The choice of the pharmacokinetic model depends on physicochemical and pharmacological properties of the tracer (e.g. size, charge, structure, half-time in blood, ...) and the applied MR-method for the detection of tracer concentration changes in the volume of interest. In this thesis, only MR-studies of tracer-uptake were used, which permit direct or indirect analyses of the physiological processes in the tumor related to perfusion and/or diffusion-limited supply with oxygen, nutrients and drugs.

The aim of this chapter is to give a short review of different pharmacokinetic models and their assumptions, which have been frequently used for the interpretation of uptake rates of diffusible tracers. Knowledge of these models permits a better understanding of the content of chapters 3 and 4.

2.2   Comparison of the freely diffusible tracer HDO with the diffusible tracer gadolinium

In this thesis, two diffusible tracers: HDO and the paramagnetic contrast-agent Gd_DTPA have been used (see Table 2.1 for physicochemical and pharmacological properties). HDO is considered a freely diffusible tracer that has access to the total water volume of a tissue (11). The term freely diffusible refers to a redistribution of tracer in the extravascular space of a volume of interest, which is not impaired by morphometric, and/or physiological parameters of the perfused vascular architecture and the extravascular space. In previous studies, the redistribution of HDO in tissue was assumed to be instantaneous and therefore limited by perfusion (11, 13-16). These characteristics make HDO a good candidate for measurements of blood perfusion. However, with respect to toxicity and MR-sensitivity, it seems unlikely that this tracer can be used for clinical purposes. Therefore the clinical contrast-agent Gd was also explored in addition to HDO. In this thesis, the abbreviation Gd refers to the contrast agent Gd_DTPA and not to the element gadolinium. In contrast to HDO, the transport of the larger tracer Gd across the microvessel endothelium may be hindered by the morphometric structure of the latter. Furthermore, the uptake of Gd is limited to the extracellular volume in tissue. Therefore, this agent is considered a *diffusible* tracer in comparison to the *freely diffusible* tracer HDO (12).

Changes in the HDO concentrations can be observed directly by ^{2}H-MRS (14,15) or ^{2}H-MRI (13,16). The magnetic resonance sensitivity of ^{2}H-spins is, however, approximately 100 times smaller than the sensitivity of ^{1}H spins (17), which makes the detection of ^{2}H-spins in small volumes with a reasonable temporal resolution presently impossible. In most ^{2}H-MR experiments, the global uptake of HDO in the whole tumor volume is detected by ^{2}H-MRS (see chapter 4 and ref. 14).

In studies of the Gd-uptake in tissue, the effect of this paramagnetic contrast agent on the T_1-relaxation time of ^{1}H-spins of water is observed. An advantage of this contrast agent is that the high MR-sensitivity of ^{1}H-spins can be used, therefore ^{1}H-MRI experiments with a high temporal and spatial resolution are possible (see also chapter 3 and ref. 4, 18). A disadvantage of this contrast agent is that changes of the tracer concentration cannot be observed directly. However, at low concentrations ([Gd] < 0.01 M) the relationship between the T_1-relaxation rate of ^{1}H-spins and [Gd] is linear (19). Thus, with appropriate MR-sequences, changes in T_1-relaxation time of ^{1}H-spins can be related to changes of the [Gd] (chapter 3 and ref. 20).

Table 2.1 Comparison of physicochemical and pharmacological properties of the two (freely) diffusible tracers used in this thesis: HDO and Gd. In reference (21) the structural formula of Gd_DTPA is given.

	HDO	Gd
Molecular weight (M)	18	583
Distribution volume in extravascular space	intra/ extracellular volume	extracellular volume
Diffusion coefficient (D) in tissue of $37°$ C .[1), 2)]	$\sim 1.10^{-5}$ cm^2.s^{-1}	$\sim 2.10^{-6}$ cm^2.s^{-1}
Half-time in blood of mice and rats ($t_{1/2}$)[3), 4)]	3 - 4 days	10 - 20 min

1)   see chapter 4, p. 54.
2)   The diffusion coefficient of Gd in tissue of $37°$ C was estimated as follows (22):
        $D_{water} \cdot \sqrt{M_{water}} = D_{Gd} \cdot \sqrt{M_{Gd}}$, (D = Diffusion coefficient, M = Molecular weight).
3)   see ref. (14).
4)   see ref. (23) and (24).

2.3   Pharmacokinetic models used for the description of HDO and Gd-uptake in tumor tissue

Until recently, two different pharmacokinetic models were commonly used to fit to Gd-uptake curves as measured in tissue: 1. the single-capillary model proposed by Larsson et al (9) in 1990 and 2. the multi-compartment model developed by Tofts et al (10) in 1991. The single-capillary model is similar to the Kety model (8), which has been used for the interpretation of HDO-uptake curves. S.S. Kety already developed this model in 1951 for the theoretical description of inert gas exchange at lungs and tissue. In 1992, the single-capillary model and the multi-compartment model were compared and possible differences explained (25).

2.3.1 General model assumptions versus reality

Schematic representations of the single capillary and the multi-compartment model are given in figures 2.1 and 2.2. Both models make some basic assumptions related to concepts in tracer kinetics. The most important assumptions are the following (see 26 for a review):

   1. Tumor volume of interest in the different models is defined as a volume with two compartments: a vascular and an extravascular compartment. The pharmacokinetic models presented in this chapter assume uniform dimensions and permeabilities along the microvessels (= vascular compartment) (9). When considering the vascular compartment in a growing tumor, one must take into account the existence of two different populations of vessels: 1. preexisting host vessels which are incorporated into the tumor tissue and 2. capillaries arising from neovascularization or angiogenesis (27). These newly formed capillaries usually show structural and functional abnormalities with regard to their spatial distribution, morphology, dimensions and permeability (28). In none of these models attention is paid to the real nature of the perfused vascular architecture of tumor tissue. In chapter 3 and 4, it will be shown that the proper interpretation of tracer-uptake rates in tumors is impossible without knowledge of the latter.

   2. The different compartments contain the well-mixed tracer in a uniform concentration throughout the compartment. This assumption may be valid in normal tissue, however, the extravascular compartment or interstitial space of a tumor is not comparable to the interstitial volume of normal tissue (3). In solid tumors the interstitial fluid pressure is generally higher than in normal tissue which is due to leaky microvessels (see previous paragraph) and the absence of lymphatic vessels. The interstitial fluid pressure was found to increase rapidly in the periphery of a tumor towards a steady state, which is maintained throughout the center of a tumor (29). This interstitial fluid pressure may be a major cause for a heterogenous distribution of macromolecules, because it leads to radially outward convection that opposes the inward diffusion (3, 29). However, for small molecules it was shown that they could enter tumor tissue freely and were not selectively excluded from any region in small tumors (30). Therefore, any spatial restriction of the tracers used in this thesis is not expected, however, interstitual fluid pressure may increase the time to reach tracer equilibrium between perfused and nonperfused regions of the tumor.

   3. It is assumed that tracer in the tumor volume of interest has arrived directly from a nearby capillary. Diffusion of tracer through the extravascular tumor volume from more distant capillaries is neglected. Therefore, the tracer-uptake should only be analyzed in regions of

interest with a high-density of perfused capillaries. The region of interest should not include nonperfused tumor regions, since tracer-uptake in these regions is due to diffusion processes from more distant perfused microvessels and would render the models invalid. Thus, prior knowledge of the 2D or 3D distribution of perfused capillaries is needed (chapter 3 and 4). In tumor tissue, the 3D distribution of capillaries may be very heterogeneous with large intercapillary distances, which makes the interpretation of tracer-uptake complicated (see end of this chapter and chapter 4).

As implicitly outlined above, tumor tissue is not comparable to normal tissue. In particular, the (perfused) vascular architecture and the extracellular matrix are different. Existing pharmacokinetic models for the interpretation of tracer-uptake in tissue can be adapted to physiological and morphological characteristics of a tumor. The function generated by the more complicated model (the one with more variables) will always come closer to the measured datapoints, but the estimated values of many physiological and morphological parameters are difficult to verify and are not always independent. For instance, functional capillaries may collapse when the interstitual fluid pressure increases which results in a lower perfused capillary density with larger intercapillary distances (3). In this thesis, efforts have been made to adapt MR-methods for tracer-uptake studies in tumor tissue in such a way that the assumptions discussed above are valid for the interpretation of the data (e.g. in chapter 3, Gd-uptake rates were only analysed in voxels with predominantly perfused capillaries) or otherwise an alternative model or interpretation of tracer-uptake is proposed (see end of this chapter and chapter 4).

2.3.2 Mathematical description of pharmacokinetic models

Both in the model of Larsson and Tofts (9,10), (tumor) tissue of interest is defined as a volume with a vascular and extravascular compartment, see Figure 2.1 and 2.2. The tracer-uptake rate in the extravascular compartment is determined by a rate constant k. The changes of the [tracer] in the extravascular compartment in time ($C_{tu}(t)$) can be descibed as follows, see Equation [1] :

$$\frac{dC_{tu}(t)}{dt} = k.(C_p(t) - C_{tu}(t)) \qquad \text{[1]}$$

$C_{tu}(t)$: tracer concentration in extravascular tumor volume at time t   (mmol.ml^{-1})
$C_p(t)$: tracer blood (plasma) concentration at time t   (mmol.ml^{-1})
k   : tracer-uptake rate constant   (s^{-1})

As pointed out in Table 2.1, the distribution volume of HDO and Gd are different in the vascular and extravascular compartment. The distribution of Gd is limited to the extracellular volume in both compartments, whereas HDO has access to the extra - and intracellular volumes.

When the tracer concentration in tumor tissue at the time of the bolus injection (t = 0) is 0, the general solution of Equation [1] is (8,9):

$$C_{tu}\left(t\right) = k.\exp^{-k.t} . \int_{0}^{t} \exp^{k.\tau} . C_{p}(\tau)d\tau \qquad\qquad [2]$$

Equation 2 is also known as the Kety equation (8) for tracer-uptake or saturation experiments. In chapter 3, p. 30 (Eq. [2]), the solution for the integral in Eq. [2] of page 14 is given.
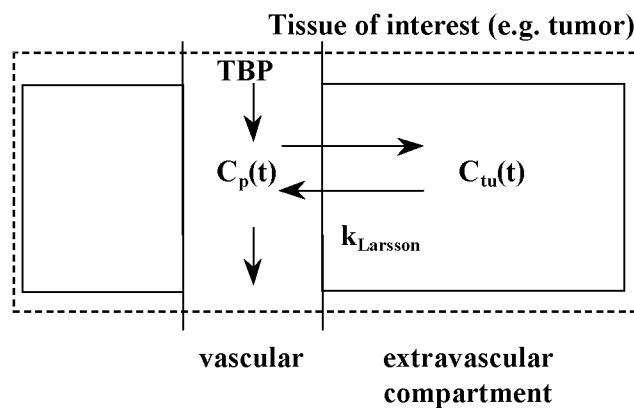
Tissue of interest (e.g. tumor)

TBP

$C_p(t)$ $C_{tu}(t)$

$k_{Larsson}$

vascular   extravascular
compartment

Figure 2.1 Single-capillary model of Larsson (9). The blood volume in tumor tissue (see dashed box) is represented by a single-capillary with uniform dimensions and permeability for the tracer. The uptake rate of the tracer is governed by the rate constant $k_{Larsson}$ and by tracer concentration difference between the vascular ($C_p(t)$) and extravascular compartment ($C_{tu}(t)$), which depends among others on tumor blood perfusion (TBP).

Bolus injection

Tissue of interest (e.g. tumor)

$C_p(t)$ $C_{tu}(t)$

vascular k_{Tofts} extravascular

k_2 k_1

Kidneys   **tissue rest body**
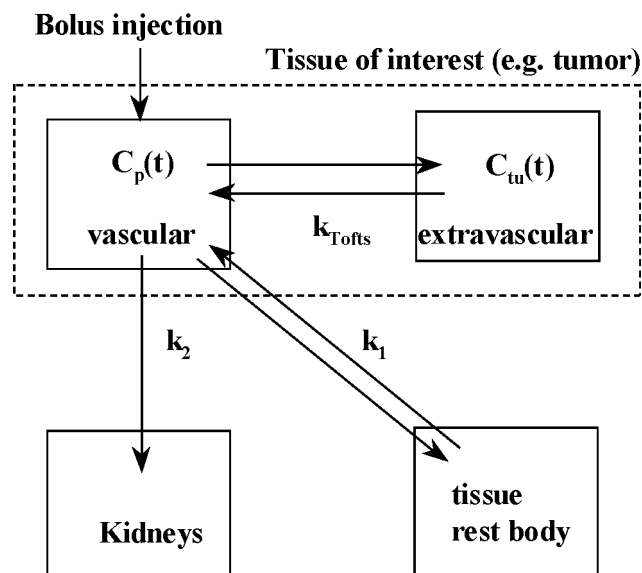
Figure 2.2 Multi-compartment model of Tofts (10). The vascular and extravascular compartment of the tissue of interest (see dashed box) are shown as well as other compartments, which influence the tracer concentration in the vascular compartment (Kidneys and rest body). Changes of tracer concentration in compartments depend on exchange rate constants: k_{Tofts}, k_1 and k_2.

The form of the function which describes the changes of the tracer concentration in blood $C_p(t)$, depends among others on the temporal resolution of the experiment. When changes of the [tracer] in tissue are measured directly after bolus injection with a high temporal resolution (sample time < 1 s per datapoint), $C_p(t)$ should include the first bolus passage of the tracer in the capillaries and a multi-exponential decay describing the clearance of the tracer from the blood compartment (see ref. 31 and next paragraph). The function $C_p(t)$ is also called the arterial input function and is measured in an artery feeding the tissue of interest: e.g. the arterial input function is detected in the carotid artery when the tracer-uptake in brain tumors is measured. Actually, the tracer concentration changes in blood should be measured in perfused capillaries and not in arteries (see Figure 2.1), however, this is impossible due to the leak of tracer into the extravascular compartment during the first bolus passage. Therefore, it is assumed that arterial tracer concentration changes are equal to changes in the perfused capillaries. In the multi-compartment model (see Figure 2.2), the first bolus passage is simply neglected by assuming an instantaneous tracer redistribution in the blood compartment after bolus injection.

When $C_{tu}(t)$ is sampled with a low temporal resolution or when it is assumed that the redistribution of the tracer in the blood compartment is instantaneous, $C_p(t)$ can be approximated by a multi-exponential decay describing the clearance of the tracer from the blood compartment only. In such a case, $C_p(t)$ is related to tracer exchanges with the extravascular compartments of tissues in the rest of the body with permeable capillaries (k_1, fast exchange) and to the clearance by the kidneys (k_2, slow exchange), see Figure 2.2 and Equation [3]. It should be noted that k_1 and k_2 depend on the physicochemical and pharmacological parameters of the tracer (see Table 2.1). For instance, the clearance of HDO by the kidneys is much slower than the clearance of Gd_DTPA: the half-times in blood are 3 – 4 days and 20 min, respectively. The loss of tracer in the blood compartment is described by a multi-exponential decay with different rate constants k_1 & k_2 and amplitudes A_1 and A_2, see Eq. [3] and Figure 2.3.

$$C_p(t) = A_1 \cdot e^{-k_1 \cdot t} + A_2 \cdot e^{-k_2 \cdot t} \qquad\qquad [3]$$

$C_p(t)$: tracer blood (plasma) concentration at time t   (mmol.ml^{-1})
A_1, A_2 : amplitudes of the fast and slow exponential   (mmol.ml^{-1})
       component, respectively
k_1, k_2 : rate constants of the fast and slow exponential   (s^{-1})
       component, respectively

It is beyond the scope of this chapter to analyse the effect of the $C_p(t)$ function on the quantification of tracer-uptake rates (k). In reference 31, this analysis was done in more detail for Gd-uptake studies in brain tumors (see also chapter 3). In perfused tumor regions, estimations of tracer-uptake rate constants were very inaccurate when a $C_p(t)$ function was used which included the bolus passage. These constants were not significantly different from experiments where the bolus passage was not included by omitting a few datapoints of the Gd-uptake curve obtained during the bolus passage. This can partly be explained by the fact that tracer-uptake in this tumor model was mainly limited by tracer transport across the capillary endothelium. But, when tracer-uptake is governed by transport in the perfused capillaries, the shape of arterial input function may influence the uptake rate in tissue.

In Figure 2.3, the changes of the [Gd] in time in the vascular (C_p(t)) and extravascular compartment (C_{tu}(t)) of a 9L-glioma rat model are shown (chapter 3 and ref. 31). The arterial input function was determined in the carotid artery and the function C_{tu}(t) was measured in a well-perfused tumor voxel, with a high-density of perfused capillaries, see legend of Figure 2.3 for details. After bolus injection of the tracer, the C_p(t) function decreased rapidly, and simultaneously the tracer concentration in the extracellular volume of the tumor (C_{tu}(t)) increased. The function C_{tu}(t) reached a maximum and was equal to C_p(t) after approximately 1 min, and declined afterwards until the tracer concentrations in the vascular and extravascular compartment of the voxel were a second time in equilibrium and decreased simultaneously.

In global HDO-uptake studies, changes of the tracer concentration in the total extravascular compartment of the tumor are not similar due among others to a different half-time in the blood compartment (Table 2.1). After the bolus passage, the concentration of HDO in blood stays constant over a long time period; thus, tracer equilibrium between the vascular and total extravascular volume by diffusion is possible during the total measurement time (see end of this chapter and chapter 4, Fig.4.4D). In Gd-uptake experiments, the latter is only possible in well-perfused voxels during a short time interval.
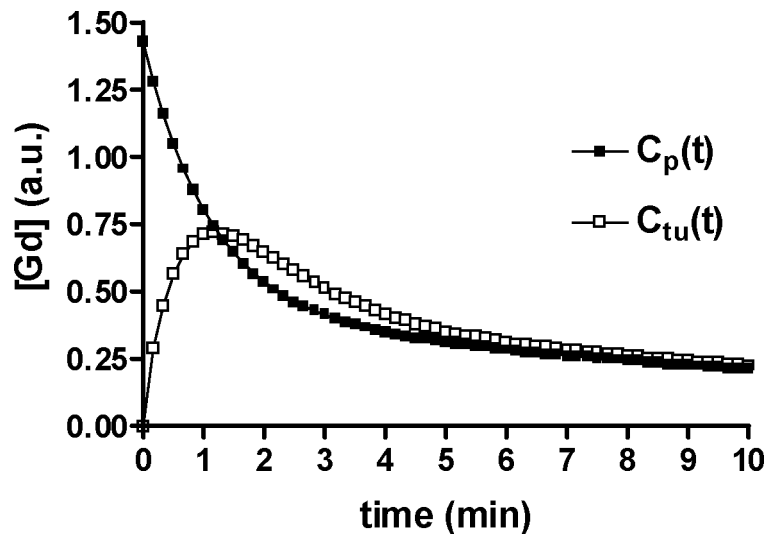
Figure 2.3 Changes of the [Gd] in time in the vascular (C_p(t)) and extravascular compartment (C_{tu}(t)) of a 9L-glioma rat model. The arterial input function C_p(t), was measured in the carotid artery and C_{tu}(t) was detected in a well-perfused voxel of the tumor. The estimated rate constant k was 0.02 s^{-1}. The following parameters of the arterial input function (C_p(t)) were found : $A_1/A_2 = 2.35$, $k_1 = 0.015$ s^{-1}, $k_2 = 0.00117$ s^{-1} (31).

2.3.3 Definitions of the tracer-uptake rate constants in both pharmacokinetic models.

The main difference between the single-capillary model of Larsson et al (9) or Kety equation (8) and the multi-compartment model of Tofts et al (10) is the definition of the rate constant k (s^{-1}). The rate constant k as defined by the model of Tofts (10) and Larsson (9) are given in Eq. [4] and Eq. [5] respectively. The different symbols of Eq. [4] - [6] are explained hereafter.

In the multi-compartment model (Figure 2.2), the tracer-uptake in the extravascular compartment of the tissue of interest is governed by the product of the capillary permeability (P) and the perfused vascular surface-area (S). Both parameters are combined in the so-called PS-product, because in most tracer-uptake studies it is difficult to separate the effect of P or S on the tracer-uptake rates. In the multi-compartment model it is supposed that this product is the rate-limiting step during tracer-uptake and not TBP.

In the single-capillary model (Figure 2.1) it is suggested that the tumor blood perfusion (TBP) cannot be excluded during the tracer-uptake and should be considered as well. The main question is: How important is the TBP in comparison with the PS-product during the extraction (E) of the tracer in tissue? Here, the extraction is defined as the fraction of the inflowing amount of tracer that leaves the vascular bed by diffusion through the capillary wall and is given by Eq. [6] (8, 32).

Finally, the distribution volume of the tracer (V_d) in the volume of interest has an inverse relationship with the uptake rate constant in both models: if V_d is large, then it will take more time to reach equilibrium between the tracer concentration in the vascular and extravascular compartment.

$$k_{Tofts} = \frac{PS}{V_d} \qquad\qquad [4]$$

$$k_{Larsson} = \frac{E.TBP}{V_d} \qquad\qquad [5]$$

$$E = \left(1 - \exp^{\frac{PS}{TBP}} \right) \qquad\qquad [6]$$

k_{Tofts} : Tracer-uptake rate constant in Tofts's model (s^{-1})

P : Permeability of perfused capillaries ($cm.s^{-1}$)
   P can be defined as the linear velocity of tracer during the passage across the capillary endothelium

S : Total surface-area of perfused capillaries (cm^2)

PS   : Permeability surface-area product $(ml.s^{-1})$
          Here, the PS-product can be seen as a volume flow
          velocity of tracer across the capillary endothelium.
V_d : Distribution volume of tracer in volume of interest (cm^3)
$k_{Larsson}$: Tracer-uptake rate constant in Larsson's model (s^{-1})
E   : Extraction of tracer during passage in capillaries   (-)
TBP   : Tumor blood perfusion $(ml.s^{-1})$

When PS » TBP, the extraction of the tracer is maximal during the passage in the perfused capillaries: E = 1 (see Eq. [6]) and no tracer would be detectable at the venous side of the tissue of interest. In such a case, the tracer-uptake in tissue is completely governed by the TBP (perfusion-limited): $k_{Larsson}$ = TBP/V_d. The model of Tofts (10) does not take into consideration such a situation.

When PS « TBP, E can be approximated by a first order Taylor expansion around PS = 0, which results in E = (1-(1-PS/TBP)). Substitution of E in Eq. [5] gives: $k_{Larsson}$ = PS/V_d, which is the same rate constant as defined by Tofts et al (10) in Eq. [4]. The tracer-uptake is now completely governed by diffusion of the tracer across the capillary endothelium (= diffusion-limited).

When both TBP and diffusion across the capillary endothelium influence the uptake rate, the situation is more difficult to describe. In Figure 3.6 of chapter 3, the relationship between $k_{Larsson}$, TBP and the PS-product was simulated using Eq. [5] and Eq.[6]. In the surface plot it is shown that for perfusion-limited tracer-uptake (TBP « PS-product), the PS-product has no influence on the value of $k_{Larsson}$. The k-value reaches a steady state when the PS-product becomes larger than TBP. When TBP increases the relationship between the PS-product and $k_{Larsson}$ becomes slowly linear, k is more and more dominated by the PS-product.

All physiological parameters of the pharmacokinetic models (TBP, PS-product) are only defined in perfused regions of the tumor. Therefore, in tumors with a heterogeneously perfused microvessel distribution, tracer-time curves should only be analyzed in voxels with perfused microvessels and not in nonperfused areas of the tumor. When TBP affects the tracer-uptake rate in perfused regions and the exchange of tracer between the capillaries and tissue is not limited by diffusion across the vascular endothelium, the model of Larsson should be used for the interpretation of tracer-uptake curves in all circumstances. The pharmacokinetic model of Tofts should only be applied for the interpretation of tracer-uptake studies, when clear evidence is provided that the tracer-uptake in the extravascular volume of tissue is controlled by tracer diffusion across the vascular endothelium (PS-product). In such a case, a linear relationship may exist between the perfused vascular surface-area (S) and the uptake rate constant, when all microvessels are highly permeable to the tracer (chapter 3). Diffusion-limited tracer uptake across the vascular endothelium may be favoured when tracers with a molecular weight larger than 20 kD are chosen.

If the tumor has a heterogeneously perfused vascular architecture with large nonperfused regions, and regional analyses of the tracer-uptake in perfused regions of the tumor are not possible, then the pharmacokinetic models cannot be fitted to the tracer-uptake curve. The latter may occur in global ^{2}H-MRS studies of the HDO-uptake in the whole volume of the tumor (see chapter 4). The latter is explained in more detail in Figure 2.4.

In this figure, tubes connected to a water tap, which regulates the perfusion rate in the whole system (TBP), symbolize the vascular system. The tube walls in the tissue of interest (■) are permeable to the tracer (•), which enters the extravascular volume via diffusion across the tube wall or vascular endothelium. In the case of normal tissue or in perfused regions of the tumor (case1), diffusion distances between the functional microvessels are small, thus the time to reach a tracer concentration equilibrium between the vascular and extravascular compartment is short. In Figure 2.4B, changes of the [tracer] as a function of the distance (--) between functional vessels in a transversal slice (- -) through the center of the tissue of interest are shown. The time to reach a steady state [tracer] in the vascular and extravascular compartment is approximately 2 s for an intercapillary distance of 50 μm. Diffusion times were estimated using a diffusion coefficient of $8.4.\ 10^{-6}\ cm^2.s^{-1}$ (see chapter 4, p. 54) and a modified partial differential equation describing HDO diffusion in one dimension (33)). In heterogeneously perfused tumors (case 2), the diffusion distances between perfused regions may be large, and consequently the time for equalization of the tracer concentration is considerable (see Figure 2.4B). This is further illustrated in Figure 1C, which shows the changes of the [tracer] in the whole tissue volume of interest as a function of time for both cases. Similar curves are obtained with ^{2}H-MRS studies of the HDO-uptake in the whole tissue volume (Figure 4.4B or 4.4D in Chapter 4).

In summary: When diffusion distances between functional microvessels are short, the tumor blood perfusion (TBP) and/or permeability surface-area product (PS-product) (see above) mainly dominate the time to reach tracer concentration equilibrium between the vascular and extravascular volume. The pharmacokinetic models described in literature and cited in this chapter can be used to relate tracer-uptake rates to TBP and/or PS-product.

However, in case 2, tracer diffusion processes in the extravascular volume determine the time to reach [tracer] equilibrium between the vascular and extravascular compartment. Until recently, no pharmacokinetic models are available, which take into consideration these diffusion processes in the extravascular space.
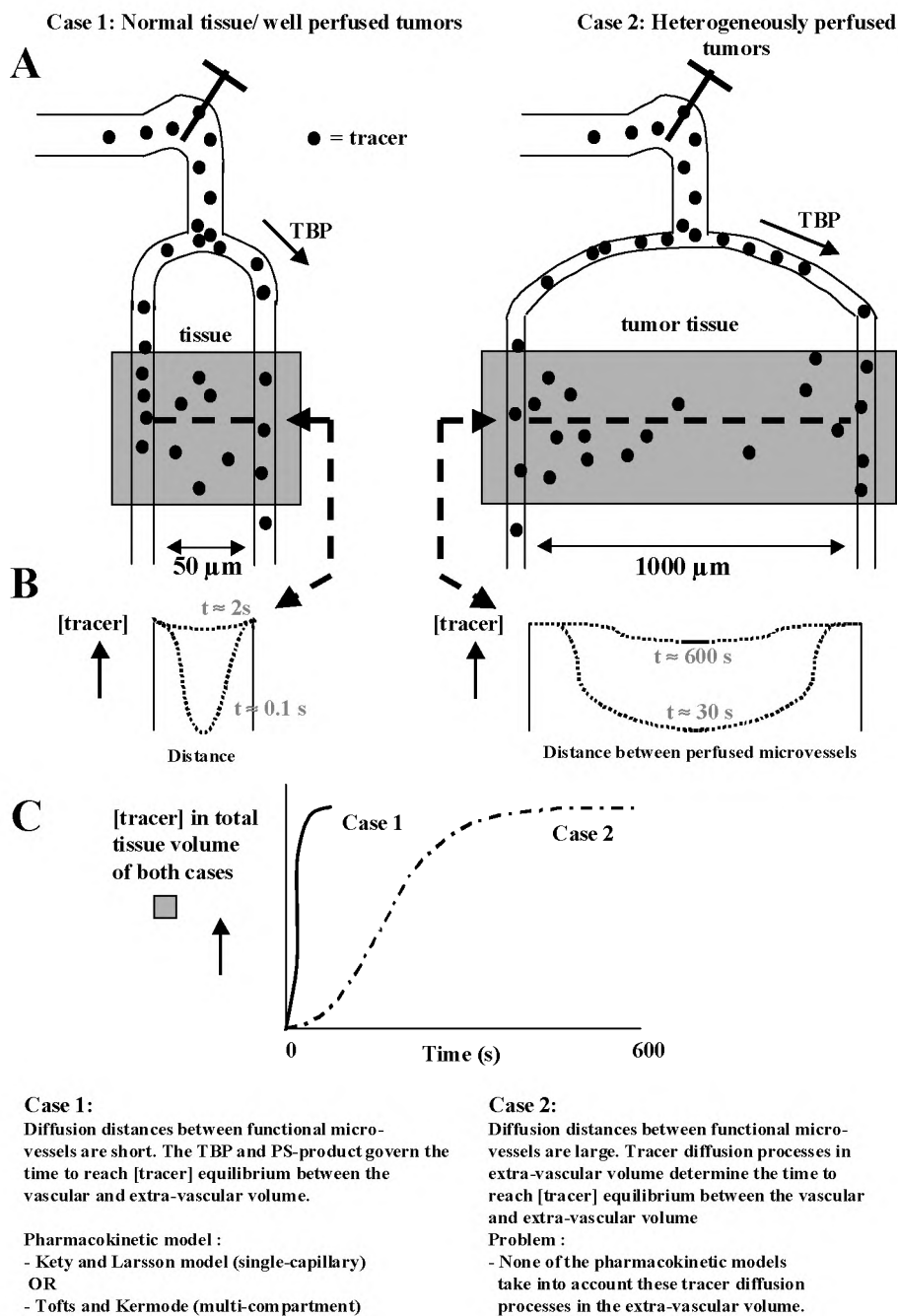
Figure 2.4 Comparison of physiological and morphometric parameters, which determine the tracer-uptake in perfused regions with short intercapillary distances (case 1) and large intercapillary distances (case 2). For further details see text.

References

1. Jain RK, Determinants of Tumor Blood Flow: A Review. *Cancer Res* **48**: 1641-2658 (1988).

2. Jain RK, Transport of molecules across tumor vasculature. *Cancer and Metastasis Reviews* **6**: 559-593 (1987).

3. Jain RK, Transport of Molecules in the Tumor Interstitium: A Review. *Cancer Res* **47**: 3039-3051 (1987).

4. Barentsz JO, Berger-Hartog O, Witjes JA, Hulsbergen van der Kaa C, Oosterhof GON, VanderLaak JAWM, Kondacki H, Ruijs SH. Evaluation of Chemotherapy in Advanced Urinary Bladder Cancer with Fast Dynamic Contrast-enhanced MR Imaging. *Radiology* **207**: 791-797 (1998).

5. Schwickert HC, Stiskal M, Roberts TPL, van Dijke CF, Mann J, Mühler A, Shames, Demsar F, Disston A, Brasch RC. Contrast-enhanced MR Imaging Assessment of Tumor Capillary Permeability: Effect of Irradiation on Delivery of Chemotherapy. *Radiology* **198**: 893-898 (1996).

6. Furman-Haran E, Margalit R, Maretzek AF, Degani H. Angiogenic Response of MCF7 Human Breast Cancer to Hormonal Treatment: Assessment by Dynamic GdDTPA-enhanced MRI at High Spatial Resolution. *JMRI* **1**: 195-202 (1996).

7. Evelhoch JL. Measurement of Tumor Blood Flow by Deuterium NMR and the Effects of Modifiers. *NMR Biomed* **5**: 290-295 (1992).

8. Kety SS. The theory and applications of the exchange of inert gas at the lungs and tissues. *Pharmacol Rev* **3**: 1-41 (1951).

9. Larsson HBW, Stubgaard M, Frederiksen JL, Jensen M, Henriksen O, Paulson OB. Quantitation of blood-brain defect by magnetic resonance imaging and gadolinium-DTPA in Patients with multiple sclerosis and brain tumors. *Mag Res Med* **16**: 117-131 (1990).

10. Tofts PS, Kermode AG. Measurements of the blood-brain barrier permeability and leakage space using dynamic MR imaging. 1. Fundamental concepts. *Mag Res Med* **17**: 357- 367 (1991).

11. Ackerman JJH, Ewy CS, Becker NN, Shaltwitz RA. Deuterium nuclear magnetic resonance measurements of blood flow and tissue perfusion employing ^2H_2O as a freely diffusible tracer. *Proc Natl Acad Sci* USA **84**: 4099-4102 (1987).

12. Strich GS, Hagan PL, Gerber KH, Slutsky RA. Tissue distribution and magnetic resonance spin lattice relaxation effects of gadolinium-DTPA. *Radiology* **154**: 723-726 (1985).

13. Larcombe McDouall, Evelhoch JL. Deuterium nuclear magnetic resonance imaging of tracer distribution in D_2O clearance measurements of tumor blood flow in mice. *Cancer Res* **50**: 363-369 (1990).

14. Mattiello JM, Evelhoch JF. Relative volume-average murine tumor blood flow measurements via deuterium nuclear magnetic resonance spectroscopy. *Mag Res Med* **18**: 320 - 334 (1991).

15. Evelhoch JL. Tracer measurements of blood flow. In "NMR in physiology and biomedicine " (Gillies RJ, Ed.), pp. 209-220. Academic Press, San Diego (1994).

16. Eskey CF, Koretsky AP, Domach MM, Jain RK. ^{2}H-Nuclear magnetic resonance imaging of tumor blood flow: spatial and temporal heterogeneity in a tissue-isolated mammary adenocarcinoma. *Cancer Res* **52**: 6010-6019 (1992).

17. Müller S and Seelig J, *In vivo* NMR imaging of deuterium. *J of Mag Res* **72**: 456-466 (1987).

18. Barentsz JO, Jager GJ, van Vierzen PBJ, Witjes JA, Strijk SP, Peters H, Karssemeijer N, Ruys SHJ. Staging urinary bladder cancer after transurethral biopsy: value of fast dynamic contrast-enhanced MR imaging. *Radiology* **201**: 185-193 (1996).

19. Wang SC, White DL, Pope JM, Brasch RC. Magnetic resonance imaging contrast enhancement versus tissue gadolinium concentration. *Invest Radiol* **25**: S44-S45 (1990).

20. Rozijn TH. MRI techniques for tissue perfusion and vascular permeability measurements. PhD Thesis, Dept. of Applied Physics, Delft University of Technology (1998).

21. Bousquet J-C, Saini S, Stark DD, Hahn PF, Nigam M, Wittenberg J, Ferrucci JT. Gd-DOTA: Characterization of a new paramagnetic complex. *Radiology* **166**: 693 - 698 (1988).

22. Kallinowski F, Runkel S, Fortmeyer HP, Förster H, Vaupel P. L-Glutamine: a major substrate for tumor cells in vivo? *J Cancer Res Clin Oncol* **113**: 209-215 (1987).

23. Wedeking P, Eaton S, Covell DG, Nair S, Tweedle MF, Eckelman WC. Pharmacokinetic analyses of blood distribution of intravenously administered ^{153}Gd-labeled, Gd(DTPA)^2- and ^{99m}Tc(DTPA) in rats. *Mag Res Imaging* **8**: 567-575 (1990).

24. Weissleder R, Cheng HC, Marecos E, Kwong K, Bogdanov A. Noninvasive In vivo Mapping of Tumour Vascular and Interstitual Volume Fractions. *European J of Cancer* **34(9)**: 1448 - 1454 (1998).

25. Larsson HBW, Tofts PS. Measurements of blood-brain barrier permeability using dynamic Gd_DTPA scanning - A comparison of methods. *Mag Res Med* **24**: 174-176 (1992).

26. Tofts PS. Modeling Tracer Kinetics in Dynamic Gd_DTPA MR Imaging. *JMRI* 7: 91 – 101 (1997).

27. Wesseling P. Angiogenesis in brain tumors: pathobiological and clinical aspects. PhD Thesis. Dept. of Pathology, Academic Hospital Nijmegen (1997).

28. Vaupel PW. Blood flow, oxygenation, tissue pH distribution and bioenergetic status of tumors. In "Ernst Schering Research Foundation Lecture 23", pp. 7-10, Information and standards medical scientific publications, Berlin (1994).

29. Jain RK, Baxter LT. Mechanisms of Heterogeneous Distribution of Monoclonal Antibodies and Other Macromolecules in Tumors: Significance of Elevated Interstitial Pressure. *Cancer Res* **48**: 7022-7032 (1988).

30. Dvorak HF, Nagy JA, Dvorak JT, Dvorak AM. Identification and Characterization of the Blood Vessels of Solid Tumors that are Leaky to Circulating Macromolecules. *Am J Pathology* **133(1)**: 95-109 (1988).

31. Rozijn TH, van der Sanden BPJ, Heerschap A, Creyghton JHN, Bovée WMMJ. Influence of the pharmacokinetic model on the quantification of the Gd-DTPA uptake rate in brain tumours using direct T_1 measurements. *MAGMA* **6**: 37-43 (1998).

32. Renkin EM. Transport of potassium-42 from blood to tissue in isolated mammalian skeletal muscles. *Am J Physiol* **197**: 1205 - 1210 (1959).

33. Goldstick TK, Fatt I. Diffusion of oxygen in solutions of blood proteins. *Chemical Engineering progress symposium series.* **66**: 101 – 113 (1970).

Chapter 3

Gd_DTPA-uptake rates are linearly related to the perfused microvessel density and surface-area in 9L-glioma in rat brain

Boudewijn P.J. van der Sanden
Tom H. Rozijn
Paul F.J.W. Rijken
Hans P.W. Peters
Arend Heerschap
Albert J. van der Kogel
Wim M.M.J. Bovée

Abstract

Purpose: to spatially correlate apparent Gd-concentrations ($r_1[Gd]$) to the 2D distribution of *perfused* microvessels, and Gd-uptake rates to morphometric parameters of the perfused vascular architecture in 9L-gliomas growing in rat brain.

Material and methods: Changes of $r_1[Gd]$ in time were analyzed in a slice through the center of ten 9L-gliomas using fast T_1-measurements. At comparable locations, $r_1[Gd]$ maps were matched to whole tumor tissue sections with (immuno)histochemically-stained perfused and nonperfused microvessels, and hypoxic areas. Finally, the pharmacokinetic model of Larsson was fitted to $r_1[Gd]$-time curves in voxels containing perfused microvessels, and $k_{Larsson}$-values were spatially related to the perfused microvessel density (N_p) or vascular surface-area (S_p).

Results: A spatial correlation was observed between $r_1[Gd]$ maps and the 2D distribution of perfused microvessels. In tumor voxels with perfused microvessels, a linear correlation was found between $k_{Larsson}$-values and N_p ($k_{Larsson} = [0.00029 \pm 2.3.10^{-5}$ (SD)] x N_p) or S_p ($k_{Larsson} = [0.23 \pm 0.02$ (SD)] x S_p). No correlation was observed between $k_{Larsson}$-values and the total microvessel density.

Conclusion: A positive correlation exists between Gd-uptake rates and the perfused microvessel density or surface-area in 9L-gliomas. The latter correlation indicates that tumor blood perfusion far exceeds the tracer transport across the microvascular endothelium. Therefore, noninvasive Gd-uptake measurements may be of additional value to pathology in the evaluation of therapies that affect the perfused microvessel density or surface-area, such as anti-angiogenic therapy.

Introduction

Information on tumor angiogenesis is important to evaluate the potential of a tumor to grow and metastasize (1, 2). Therefore, direct and indirect methods have been developed to analyze the angiogenic capacity of a tumor (1, 3-5). One of the more direct methods of assessing tumor vascularity is the microvessel density (MVD) technique (1, 3, 5). With this technique endothelial cells of all microvessels are immunohistochemically stained in biopsy specimen and quantification is established from regions with the highest vascular density (hot spots) by the pathologist. Several clinical studies have shown that increased microvessel density is correlated to poorer overall survival and/or increased risk for metastasis: for instance in patients with breast and prostate carcinoma (1, 3-6). However, these correlations were less obvious in other malignant lesions (7).

The MVD technique has many drawbacks such as the low reproducibility among pathologists (4, 8) and the inability to distinguish between perfused and nonperfused microvessels. The morphological appearance of the total vascular bed does not necessarily allow judgements on functional aspects of the tumor microcirculation (9). Microvessels, which are not perfused during a long time, are not expected to contribute to tumor growth or metastasis. Therefore, a relevant analysis of the vascular bed should include an evaluation of the distribution of perfused microvessels. The perfused microvessel distribution may be assessed noninvasively by dynamic Gd_DTPA (Gd) -enhanced magnetic resonance imaging (MRI). This paramagnetic contrast agent appears to accumulate in the extracellular tumor volume adjacent to perfused microvessels, which are permeable to this tracer (10). This suggests a possible role for dynamic Gd-enhanced MRI in obtaining in vivo information on the perfused microvessel distribution with prognostic potential.

In addition, pharmacokinetic models have been developed to examine wheter Gd-uptake rates are related to physiological parameters such as tumor blood perfusion (11) and the perfused capillary permeability surface-area product (PS-product, (12)). Information on Gd-uptake rates and the spatial distribution of Gd were useful in longitudinal studies of tumor therapy effects (13-15). The latter may be of particular importance in the follow-up of anti-angiogenic therapy where the effect of an agent on the angiogenesis in solid tumors may be analyzed noninvasively by dynamic Gd- enhanced MRI (4, 8, 16). In previous studies, Gd-uptake rates have been related to the microvessel density (MVD), but in most reports poor correlations were found (17-20). A number of factors may contribute to this. First, it was not possible to spatially correlate the MVD with Gd-uptake rates, because Gd-enhanced MRI was not used to guide biopsy of surgical specimens. Secondly, the applied MVD technique (1) evaluates all microvessels whereas dynamic Gd-Enhanced MRI only senses functional or perfused microvessels.

Therefore, the aim of this study is to see whether a spatial correlation exists between 1) apparent Gd-concentrations and the 2D distribution of perfused microvessels, and between 2) Gd-uptake rates (k-values) and morphometric parameters of the perfused vascular architecture, such as the perfused microvessel density (N_p) and vascular surface-area (S_p). As a tumor model, 9L-gliomas growing in rat brain were used. The perfused vascular surface-area has been suggested to determine the Gd-uptake rates in perfused tumor regions together with other physiological parameters, such as tumor blood perfusion (TBP) and microvessel permeability (P) (11, 12).

For this purpose, the apparent Gd-concentration ($r_1[Gd]$) as a function of time was determined using a fast dynamic MRI T_1-sequence (21). Next, pharmacokinetic models were fitted to $r_1[Gd]$-time curves (11, 12, 21) to estimate k-values per voxel (k-map).

The distribution of apparent Gd- concentrations (r_1[Gd]) and k-maps were spatially correlated to immunohistochemical images showing the 2D distribution of perfused microvessels, the total vascular bed (MVD technique), chronically hypoxic cells (22), and necrotic regions in whole tumor sections at comparable locations as the MR-slices. Staining of these cells or cell structures permits comparison of the total vascular bed with the perfused microvessel distribution, and detailed analyses of nonperfused tumor areas. Whole tumor sections were analyzed using a computer-controlled image-processing system connected to a (fluoresence) microscope (23). In this way, the reproducibility of the (immuno)histochemical analyses was increased and the quantification of morphological parameters was independent of the pathologist's choice of certain tumor regions. In MR-voxels containing functional microvessels, morphometric parameters of the perfused vascular architecture were related to Gd-uptake rates.

Material and Methods

Animal model. Ten days before the NMR experiments, 9L-glioma cells (kindly provided by Dr Jeffrey A. Coderre, Brookhaven National Laboratory, Upton, N.Y., USA) were injected in the brain of 10 Fischer rats (CDF® (F-344)/CrlBr Charles River Laboratories, Germany). Cannulae (Insyte®, Ø 0.7/19 mm, 24 G., Becton Dickinson Belgium) were inserted in a tail vein for online administration of Gd_DTPA (Magnevist®, Schering AG, Germany) solution in saline (dose: 0.2 mmol.kg^{-1}, duration of bolus injection is 2 s). Rats were anaesthetized by subcutaneous injection of 0.1 ml of an atropine solution (Atropini Sulfas, Pharmachemie B.V., Haarlem, Netherlands) followed by exposure to 1.5 % enflurane in an oxygen-nitrous oxide (30 % O_2) mixture applied through a nose cone. Body temperature was monitored with a rectal probe (Ø 3.5 mm, Hewlett Packard) and maintained at 36.5° - 37° C by a warm water blanket with a feed back system. The local ethical committee for animal use approved the experimental procedures.

MR-measurements. MR-experiments were performed on a home-built spectrometer (6.3 T) using a single tuned ^{1}H-resonator with a diameter of 3 cm well adapted to the rat head. Before the start of Gd-uptake measurements, the tumor location and size were determined in coronal, sagittal and transversal slices using a fast T_1-sequence (see below). In this study, the T_1-relaxation times of water ^{1}H-spins in tumor regions were longer than in normal brain tissue: thus, tumor regions were clearly delineated in T_1-maps through the whole brain. Next, in a transversal slice through the center of the tumor, the homogeneity of the local B_o- field was optimized. The uptake of Gd was measured in this slice using a SNAPSHOT T_1-method (24) with an interleaved EPI imaging sequence (21). An effective T_1 value (T_1*) is obtained using this sequence (24). The Gd-uptake experiment contained 15 T_1* maps prior to the bolus injection (T_{10}*) and 40 T_1* maps after bolus injection (21). One SNAPSHOT T_1-experiment consisted of 12 images of 300 ms duration each with a flip angle of 5°, a time resolution of 3.6 s, FOV = 30 x 30 mm, resolution 90 x 90 pixels, and slice thickness = 2 mm.

MR-data analyses. Gd-uptake rate constants (k, s^{-1}) per voxel (k-map) were obtained by the following 3 steps (21). First, 15 effective T_1-experiments prior to the bolus injection were averaged to obtain a high SNR T_{10}* measurement. For each voxel, a mono-exponential three-parameter model function (see Eq. [1]) was fitted to 12 phase corrected ^{1}H-MR signals of a relaxation curve (M(t)) using the Marguardt least-squares non-linear fitting algorithm (25) (IDL-software 5.1, Creaso GmbH, Gilching, Germany). In this way, a T_{10}*map was generated (24). In Eq. [1], - M_b is the magnetization directly after inversion and M_0* is the effective end and/or rest magnetization, Eq. [1]:

$$M(t) = M_0^* - (M_0^* - M_b).\exp^{-\frac{t}{T_{10}^*}} \quad \text{[1]}$$

Secondly, T_1*-relaxation maps after bolus injection were obtained in a similar. The linear relationship between changes in the effective T_1 relaxation rates and the average Gd-concentration in the extravascular volume of tumor tissue was used to calculate apparent Gd-concentration maps: $r_1[Gd] = 1/T_1^* - 1/T_{10}^*$. The constant r_1 or relaxivity ((mM.s)$^{-1}$) depends on tissue parameters such as temperature and pH (26). These tissue parameters were unknown; thus, only apparent Gd-concentration maps could be calculated, which was sufficient in this study.

Finally, a k-map was obtained after fitting the pharmacokinetic model of Larsson (11, 21) to $r_1[Gd]$ - time curves per voxel $(r_1[Gd](t))$, see Equation [2]. The Powell minimization method was used for the least-squares non-linear fitting (27). In Eq. [2], the uptake rate constant k (s^{-1}) as proposed by Larsson et al (11) is defined as $k_{Larsson}=$ TBP.E/ V_d. TBP is the tumor blood perfusion $(ml.s^{-1})$, E (-) is the extraction fraction of the amount of tracer during bolus passage $(E = 1 - exp(-PS_p/TBP))$ and V_d is the distribution volume (ml) of the tracer, which equals the extracellular volume in the case of Gd (see end of material & methods). In the extraction term (E), P is the permeability of the microvessel endothelium for the tracer $(cm.s^{-1})$ and S_p is the total *perfused* microvessel surface-area (cm^2) in the volume of interest (see next section immunohistochemical analyses). If TBP is much larger than the PS_p-product, then k approaches the uptake rate constant as proposed by Tofts, see (12, 28): $k_{Tofts} = PS_p/V_d$.

Changes of the apparent Gd-concentration in time are generally given by Eq. [2] with a scaling factor S (21):

$$r_1.[Gd](t) = S\left[\frac{A_1.k}{k-k_1}.\exp^{-k_1.t} + \frac{A_2.k}{k-k_2}.\exp^{-k_2.t} - \left(\frac{A_1.k}{k-k_1} + \frac{A_2.k}{k-k_2}\right)\exp^{-k.t}\right] + r_1.[Gd]_0.\exp^{-k.t}$$

[2]

In Eq. [2] $r_1[Gd]_0$ is the apparent Gd-concentration at t = 0, A_1, A_2 and k_1, k_2 are amplitudes (mM) and rate constants (s^{-1}), respectively, of the arterial input function $C_p(t)$, which describes the bi-exponential decay of the Gd-concentration in bloodplasma (p) in a carotid artery during the time of the Gd-uptake experiment, see Eq. 3 and (12, 21). The fast phase of this bi-exponential decay (k_1) is governed by Gd-exchange with the extravascular volumes in rest of body, and the slow phase (k_2) is determined by the Gd- clearance via the kidneys (12).

$$C_p(t) = A_1.\exp^{-k_1.t} + A_2.\exp^{-k_2.t} \qquad [3]$$

The arterial input function $(C_p(t))$ was determined independently in 3 rats (21). Briefly, the carotid arteries of 3 rats were cannulated and 20 blood samples of 60 μl per rat were taken at 7 s intervals directly after bolus injection of Gd through the tail vein. Directly after sampling, blood samples were diluted in 10 μl heparine and 10 ml saline. Next, absolute Gd concentrations were determined using inductively coupled plasma-emission spectrometry (IL Plasma-200, Instrumentation Laboratory Benelux, IJsselstein, the Netherlands). The following parameters for the $C_p(t)$ function of Eq. 3 were found: $k_1 = 0.015$ s^{-1} ± 0.004 (SD) and $k_2 = 0.00117$ s^{-1} ± 3.10^{-4} (SD) and $A_1/A_2 = 2.35$ ± 0.2 (SD).

In reference 21, the effect of the bolus passage on estimations of uptake-rate constants was analyzed. A mean bolus passage was measured in a transversal slice through normal rat brain at a comparable location as 9L-gliomas in this study. When the bolus passage was included in the $C_p(t)$ function, estimations of tracer-uptake rate constants became very inaccurate. These constants were not significantly different from estimations of k-values when the bolus passage was not included. Therefore, the first data points of the $r_1[Gd]$-time curves which coincided with the bolus passage were omitted before fitting the curves to Eq. [2] (Figure 3.3B).

Fluorescence microscopy. In complete transverse tumor sections morphometric analyses of the total vascular bed, perfused microvessels, hypoxic-/ necrotic areas and the extracellular volume in viable regions were performed using a computer-controlled digital-image analyses system connected to a (fluorescence) microscope.

Immunohistochemical staining. One day after the MR-measurements, markers for the detection of hypoxic cells (Pimonidazol, 20 mg in 0.1 ml saline, kindly provided by Prof. J. Raleigh, Dept. of Radiation Oncology and Toxicology, UNC school of medicine, Chapel Hill, NC, USA) and perfused microvessels (Hoechst 33342, 3 mg in 0.1 ml saline, Sigma, St.Louis, MO, USA) were injected via a lateral tail vein 60 min and 1 min, respectively, before sacrificing the rats. One minute after Hoechst injection, a complete transversal section of the brain containing the entire tumor as determined from T_1* maps after Gd injection, was quickly removed and frozen in liquid nitrogen. In every tumor, 10 frozen tissue sections (5 μm) at a location corresponding to the slice of the Gd -uptake experiment, were made using a cryo-microtome. Five sections, homogeneously distributed throughout the 2 mm slice of the MR-measurements, were used for quantitative immunohistochemical analyses of the 2D distribution of the total vascular bed, perfused microvessels (Hoechst) and hypoxic areas (pimonidazole).

The endothelium of all microvessels (= total vascular bed) was visualized with goat anti-collagen IV (Southern Biotechnology Associates, Birmingham, AL, USA) followed by a second antibody, TRITC-labeled donkey anti-goat (Jackson ImmunoResearch Laboratories Inc., West Grove, USA). For the staining of hypoxic areas, sections were incubated with rabbit anti-pimo (kindly provided by Prof. J. Raleigh, Dept. of Radiation Oncology and Toxicology, UNC school of medicine, Chapel Hill, NC, USA) followed by incubation with FITC-labeled donkey anti-rabbit immunoglobulin (Jackson ImmunoResearch Laboratories, West Grove, USA). Three tumor sections in between the previous 5 sections were used for conventional staining with eosin (cytoplasm) and haematoxylin (nuclei). Finally, NADH-diaphorase in the whole cytoplasm of cells was labeled in the remaining 2 sections using NADH and Nitro-blue-tetrazolium (NBT) (Sigma, St.Louis, MO, USA). Previous stainings were used to distinguish viable tumor regions from necrotic areas and to estimate the extracellular volume in viable regions (see end of material & methods).

Scanning and processing. Tumor tissue sections were processed in three steps: First, the perfused microvessels (Hoechst) were analyzed, followed by immunohistochemical staining of hypoxic areas and the endothelium of all microvessels. The distribution of necrotic areas and extracellular volume were evaluated separately. After each staining step sections were scanned using an extended version of the digital-image analyses system as described by Rijken et al (23). After processing all fields of each scan a composite image was reconstructed from the individual processed fields revealing the different structures. If the composite images of the tumor sections obtained after each step were combined, then the new matched image showed the 2D distribution of perfused microvessels, hypoxic areas and the total vascular bed simultaneously.

Finally, the fluorescent rim of the Hoechst dye around perfused microvessels due to Hoechst diffusion into adjacent tissue was deleted by image processing. In this way, the perfused surface-area of microvessels (see below) was not overestimated.

Data analyses.

Matching of r₁[Gd] maps with immunohistochemical images. For each tumor, a representative immunohistochemical image showing the 2D distribution of perfused microvessel and hypoxic cells approximately half-way the 2 mm MR-slice, was used for matching with a r_1[Gd] map obtained one minute after bolus injection. This particular r_1[Gd] map was used, because rats were sacrificed one minute after injection of the fluorescent perfusion marker Hoechst. During the interactive matching (= shifting and rotating of the r_1[Gd] maps relative to the immunohistochemical images) using IDL-software (IDL 5.1, Creaso GmbH, Gilching, Germany), prior knowledge on orientations of 1) the r_1[Gd] maps obtained in Gd-uptake studies, and 2) the tumor sections during histochemical processing was used.

To enable further analyses, an MR-lattice was generated consisting of voxels with a 4 times lower spatial resolution than in original r_1[Gd] maps using IDL-software (the new voxel volume was approximately 1 mm³). In a further study, the 2D distribution of r_1[Gd] in tumor slices will be spatially correlated to the distribution of metabolites as measured by spectroscopic imaging, therefore the spatial resolution of both experiments was tuned. In addition, the analyzes of correlations between k-values and morphometric parameters in large voxels are less sensitive to a mismatch of the Gd-enchanced MRI with histology than in small voxels.

Subsequently, each voxel of the MR-lattice was labeled. With help of the representative immunohistochemical image different categories of voxels were assigned as follows:
- Pr   = voxels with perfused microvessels at the rim of the tumor.
- P   = voxels with perfused microvessels inside the tumor.
- PH   = voxels with perfused microvessels and hypoxic areas inside the tumor.
- HN   = voxels with hypoxic- and necrotic areas only.

It should be noted that the distribution of perfused microvessels and hypoxic cells may slightly differ between the representative tumor section of the MR-slice and the 4 other sections homogeneously distributed throughout the MR-slice. For instance, a MR-voxel of category P, as assigned with use of the representative section may contain hypoxic cells in the other sections. All 5 tumor sections were used for estimations of morphometric parameters of the perfused vascular. For each voxel of category P and PH, correlations between these morphometric parameters and Gd-uptake rate constants (k-map) were analyzed (see next paragraph). The latter is important because r_1[Gd]-time curves were fitted to pharmacokinetic models with parameters such as TBP and PS_p-product, which are only defined in voxels with perfused microvessels. Voxels of category Pr were not included, because a large volume fraction in these voxels coincide with 'normal' brain tissue. A detail of an immunohistochemical image overlaid with a rotated and shifted MR-lattice is shown in Figure 3.3A, with assignments for the different voxel categories and voxel numbers.

Estimations of the (perfused) microvessel density, the perfused microvessel length density and the total perfused surface-area. For each voxel of category P and PH the following 4 morphometric parameters were estimated: **1**. perfused microvessel density (N_p, no.mm⁻²); **2**. the total microvessel density (= density of perfused and nonperfused microvessels (N, no.mm⁻²)); **3**. the perfused microvessel length density (L_p, mm.mm⁻³), and **4**. the total perfused

surface-area density (S_p, $cm^2.mm^{-3}$). The microvessel density parameters N_p and N were defined as the mean of the perfused and total microvessels density per 5 tumor sections homogeneously distributed throughout a voxel. The perfused microvessel length density and surface-area density were estimated using a stereological algorithm (29). Briefly, for an estimation of L_p per voxel, the sum of the major axis (a) divided by the minor axis (b) (= eccentricity of ellipse) of all cross-sectional areas of perfused microvessels in all 5 tumor sections was divided by the total sum of areas per section in which microvessels were analyzed (A_t), see equation: $L_p = \Sigma a/b / \Sigma A_t$. Five whole tumor sections were used for the calculations of L_p, because pilot studies revealed that the values of the latter were not significantly different when 10 or 20 tumor sections were taken. Furthermore, a model was developed to test the stereological algorithm for the estimation of L_p on our digital-image analyses system. The error in the estimation of L_p was approximately ± 15 %. In addition, analyses of L_p in different regions of the normal rat brain were comparable to estimations of L_p in previous studies (30) (results to be published elsewhere).

Next, the value of S_p was estimated after determination of the median radius (r) of all perfused microvessels per 5 tumor sections (= median of minor axis b divided by 2), using the following equation: $S_p = (2.\pi. r. Lp)/ 100$. The perfused microvessels were approached as cylinders with uniform dimensions. For each voxel of category P and PH, the relationship between N_p or S_p and $k_{Larsson}$ values was analyzed using Graphpad software (Graphpad PRISM version 2, San Diego, USA).

Estimations of the extracellular volume in perfused tumor regions. The following 3 steps resulted in an estimated distribution volume of Gd (V_d) in perfused voxels. First, the extracellular regions were segmented from the cells stained by NADH-diaphorase applying a threshold operation in digitized images. Secondly, the extracellular volume (V_e) was estimated in perfused voxels using the following equation: $V_e \approx 1 - $ (surface-area cells/ sample area). Finally, per perfused voxel the extracellular volume was corrected for the vascular volume (V_v) using the parameters defined in the previous paragraph (vascular volume per voxel volume is approximately: $V_v \approx \pi.r^2.L_p$). The value of V_d equals $V_e - V_v$, and is assumed to be a maximum estimate of the Gd distribution volume in in vivo studies, because some cell shrinkage may occur during the quick-freeze of tumors.

Results

Matching of r_1[Gd] maps with immunohistochemical images.

Examples of this matching for two tumors are shown in Figure 3.1 and 3.2. The r_1[Gd] maps as obtained 1 min after bolus injection of Gd (Figure 3.1A and 3.2A) were matched with immunohistochemical images showing the 2D distribution of perfused microvessels, the total microvessel bed and hypoxic regions (Figure 3.1C and 3.2C). In all tumors a positive correlation was observed between the distribution of the apparent Gd-concentration and the perfused microvessel distribution. Tumor regions with no Gd uptake appeared to be chronically hypoxic or necrotic. Necrotic areas were found in regions enclosed by hypoxic cells (results not shown here).
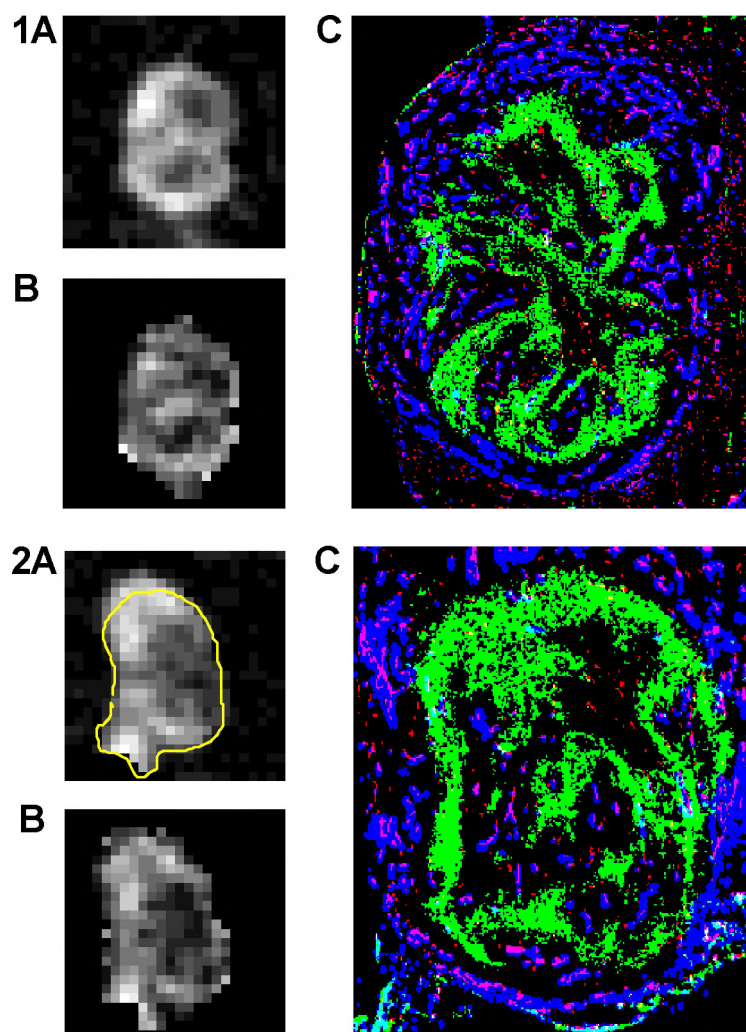

Figure 3.1 and 3.2 A) The distribution of the apparent Gd-concentration (r_1[Gd]) for two representative tumors in a transversal slice (2 mm) through the center of the tumor 1 min after bolus injection of Gd. **B)** k-maps, calculated using the Larsson model. **C)** Representative tumor sections at comparable locations as MR-slices showing the 2D distribution of the total vascular bed (red structures), perfused microvessels (blue structures) and hypoxic areas (green structures). The immunohistochemical image of Figure 3.2C matches the delineated area in Figure 3.2A.

In Figure 3.3A, a detail of an immunohistochemical image is shown which was overlaid with an MR-lattice as determined after matching with a r_1[Gd] map. A pharmacokinetic model proposed by Larsson was fitted to changes of r_1[Gd] in time per voxel (11, 21), resulting in a k-map (Figure 3.1B & 3.2B). In Figure 3.3B, an example is shown of a fitted r_1[Gd]-time curve as measured in a well-perfused voxel of category P.

Analyses of correlations between Gd-uptake rates and parameters of the perfused vascular architecture.

With the help of immunohistochemical images, only voxels containing perfused microvessels (categories P and PH) were selected for a comparative study between $k_{Larsson}$-values and parameters of the perfused vascular architecture (Figure 3.4 and 3.5). In previous studies, Gd-uptake rates were related to the microvessel density (MVD, (17, 18)). In our study, it appeared that Gd-uptake rates or $k_{Larsson}$-values (s^{-1}) have a linear relationship (Figure 3.4A) with the perfused microvessel density (N_p) in voxels of category P and PH in transversal slices through the center of 10 9L-gliomas. However, no clear relationship was found between $k_{Larsson}$-values and the density of all microvessels (perfused and nonperfused vessels, N) (Figure 3.4B).

In a next step, analyses of the perfused vascular density were extended to estimations of the perfused vascular surface-area per voxel (S_p). The latter parameter is expected to have a stronger correlation with Gd-uptake rates, when TBP is much larger than the PS-product (see definition of $k_{Larsson}$ and k_{Tofts}). Before S_p can be calculated, the length density (L_p, (mm.mm^{-3})) per voxel was estimated using a stereological algorithm (29). The lenght density is comparable to the perfused microvessel density N_p when microvessels are arranged parallel to each other and perpendicular to cross-sectional areas of the voxels (29). If the microvessels are bent and twisted throughout the voxel volume, then L_p is always larger than N_p. In tumor voxels of category P and PH of all 9L-gliomas the following linear correlation was found after least-squares regression analyses (n = 86, R^2 = 0.95): L_p = [4.6 ± 0.3 (SD)] x N_p. The large slope value (> 1) indicates that perfused microvessels were tortuous in the different voxels.

Finally, the perfused length density (L_p) and a median radius of all perfused microvessels (r) in the 5 tumor sections per MR-voxel were used to estimate the perfused vascular surface-area density (S_p) in P and PH voxels. The $k_{Larsson}$-values were found to be linearly related to the estimated perfused surface-area density (S_p) (Figure 3.5). This correlation was slightly better than the correlation between Gd-uptake rates and the perfused microvessel density (N_p) as shown in Figure 3.4A, see goodness of fit (R^2- values) in legends of Figures 3.4A and 3.5. The median radii which were used for the estimations of S_p varied between 3.6 and 6.5 μm. The distribution of the perfused microvessel radii was not homogeneous, however the percentage of radii larger than 2 times the median radius did not exceed 5 %. Thus, significant groups of large microvessel radii were not observed and are not expected to influence considerably the estimations of S_p.
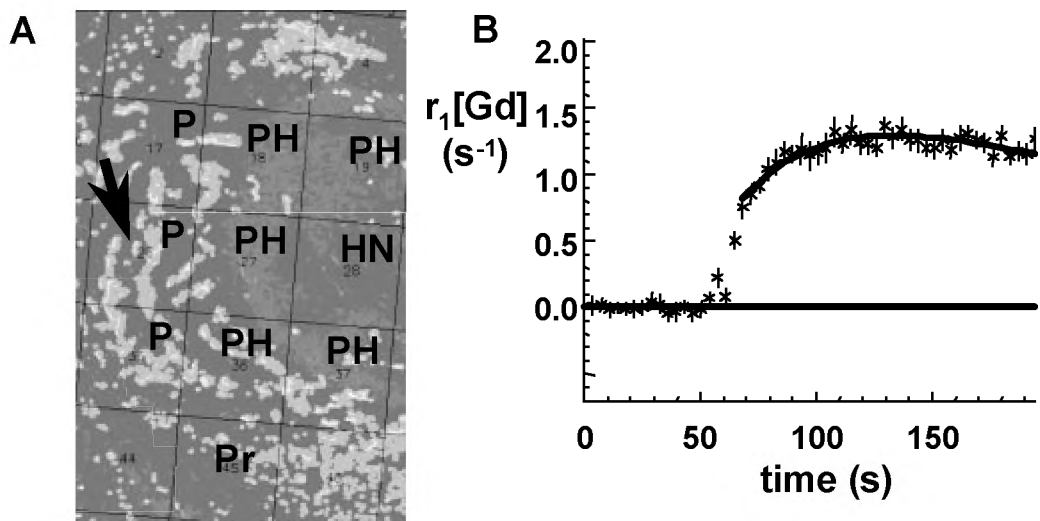
Figure 3.3 A) A detail of an immunohistochemical image (see Figure 3.2B) overlaid with a MR-lattice. The different voxel categories: Pr, P, PH and HN are denoted. The light grey structures correspond to perfused microvessel (see also Fig. 3.1C and 3.2C) and dark grey structures in PH and H voxels are hypoxic cells. **B)** A r_1[Gd]-time curve (* dashed line) of voxel no. 26 (category P, see black arrow) is fitted to the Larsson model (solid line). The nonlinear regression analyses resulted in a $k_{Larsson}$ value of 0.012 ± 0.0026 (SD) s^{-1}. The error bars indicate the 95 % confidence interval.
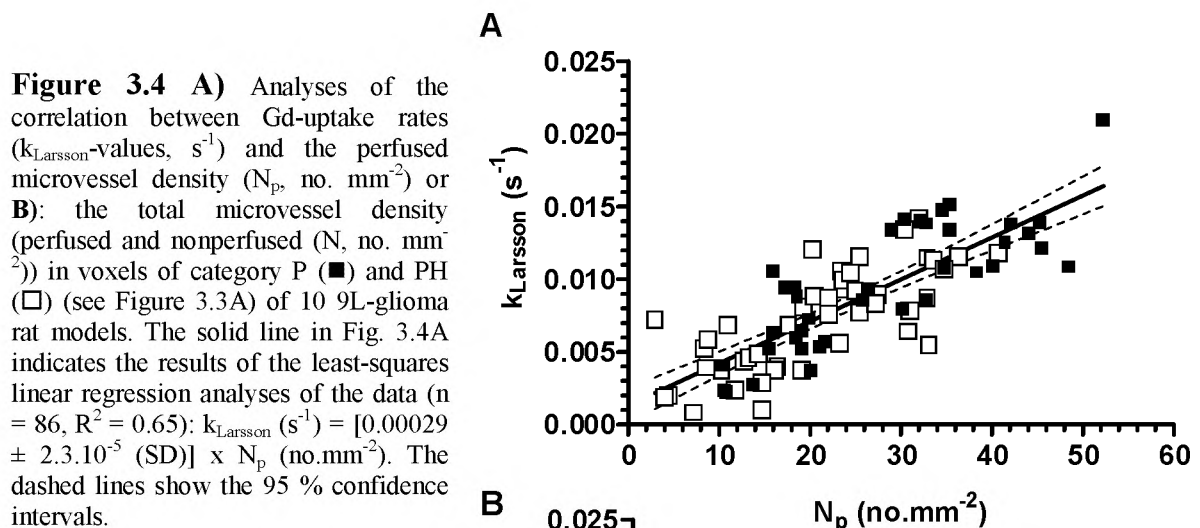
Figure 3.4 A) Analyses of the correlation between Gd-uptake rates ($k_{Larsson}$-values, s^{-1}) and the perfused microvessel density (N_p, no. mm^{-2}) or **B)**: the total microvessel density (perfused and nonperfused (N, no. mm^{-2})) in voxels of category P (■) and PH (□) (see Figure 3.3A) of 10 9L-glioma rat models. The solid line in Fig. 3.4A indicates the results of the least-squares linear regression analyses of the data (n = 86, $R^2 = 0.65$): $k_{Larsson}$ (s^{-1}) = [0.00029 $\pm$ 2.3.10^{-5} (SD)] x N_p (no.mm^{-2}). The dashed lines show the 95 % confidence intervals.
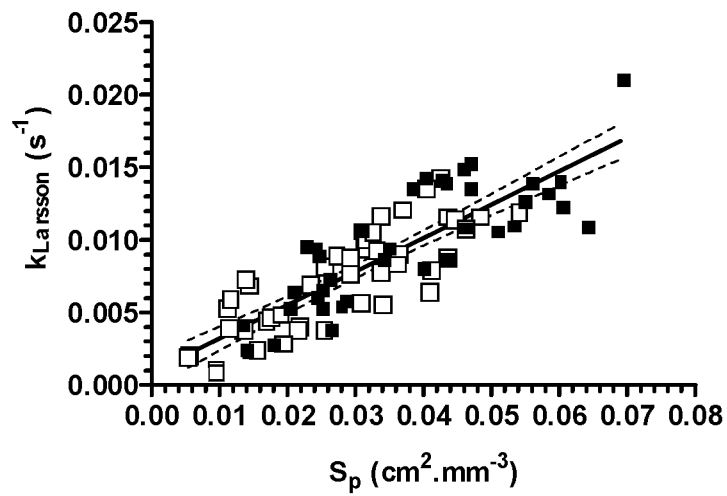
Figure 3.5 The correlation between $k_{Larsson}$-values (s^{-1}) (y-axis) and the perfused vascular surface-area (S_p, $cm^2.mm^{-3}$) per voxel of categories P (■) and PH (□) (see Figure 3.3A) in 10 9L-gliomas. The solid line indicates the results of the least-squares linear regression analyses of the data (n = 86, R^2 = 0.72): $k_{Larsson}$ (s^{-1}) = [0.23 ± 0.02 (SD)] x S_p. The dashed lines show the 95 % confidence intervals.

Discussion

Tumor growth and metastasis is associated with angiogenesis (1, 2, 4). The angiogenic capacity of a tumor has been related to the total microvessel density (MVD), but information on this morphometric parameter does not necessarily allow judgements on functional aspects of the tumor microcirculation. Microvessels, which coincide with chronically hypoxic areas or necrotic regions, may not contribute to tumor growth or metastasis. Fast dynamic ^{1}H-MRI studies of the Gd-uptake in tumor tissue have potential to gain insight into the distribution of perfused microvessels in tumor tissue slices or to provide knowledge on the perfused vessel density or vascular surface-area. Before dynamic Gd-enhanced MR-imaging can be recognized as a valid technique for analyses of functional microvessels, it will need extensive comparison with other techniques.

In this study, Gd-uptake rate constants were compared to immunohistochemical analyses of morphometric parameters of the perfused vascular architecture. This is possible when changes of the T_1-relaxation time of water protons as a function of time due to the uptake of Gd in the extracellular volume are directly related to Gd-concentration changes. Fast dynamic SNAPSHOT T_1-measurements permit direct analyses of the apparent Gd-concentrations as a function of time, which can be related to morphometric and physiological parameters of the perfused vascular architecture by fitting pharmacokinetic models to Gd-uptake curves (11, 12). Measurements of Gd-uptake rates are also possible with T_1-weighted fast MRI sequences (31-33), but these results are less accurate than those obtained with the fast T_1-method. For instance, changes of signal intensities in T_1-weighted fast MR images depend on the pulse angle α (and so RF-inhomogeneity), the MR-sequence (TR, RF-spoiling), and the T_1, T_2 and T_2^* relaxation times. In reference experiments, the T_2 and T_2^* relaxation times differ from those in the experiments after Gd-injection, and depend on the time after injection. However, the calculation of $r_1[Gd]$ changes using T_1 maps before and after tracer administration are independent of the previous acquisition parameters and T_2, T_2^* relaxation times (34).

The immunohistochemical analyses, which has been applied one day after the MR-experiments, seems to detect nearly all functional microvessels, since in regions with nonperfused microvessels chronically hypoxic cells (diffusion-limited oxygen-supply) and necrotic areas were detected. Microvessels, which transiently open and close in such ways that a hypoxic region appears acutely were not observed. In such a case, the Hoechst signal would show overlap with hypoxic cells and/or isolated areas of non-hypoxic cells would occur in hypoxic regions around nonperfused microvessels. Thus, it seems safe to presume that the immunohistochemical method allows a proper evaluation of functional aspects of the tumor microcirculation.

The distribution of apparent Gd-concentrations in whole transversal tumor slices was found to be spatially correlated to the 2D perfused microvessel distribution in a representative tumor section of that slice. In a next step, Gd-uptake rates were found to be linearly related to the perfused microvessel density, and perfused microvessel surface-area in voxels containing perfused microvessels. The linear relationship between $k_{Larsson}$ and the perfused vascular surface-area indicates that the Gd-uptake rate is not affected by variations in vascular permeability (P) and/or tumor blood perfusion (TBP). In the present study, the molecular weight of Gd is probably not large enough to discriminate between more or less leaky tumor microvessels; all microvessels were highly permeable to Gd. The heterogeneity of the vascular permeability may be assessed by contrast agents with a molecular weight larger than 20 kD (35-37).

In previous fast dynamic MRI-studies of the Gd-uptake, two different pharmacokinetic models were used to fit to changes of the apparent Gd-concentration in time, namely: the multi-compartment model of Tofts (12, 38) and the single-capillary model of Larsson (11). If Gd-uptake rates are not affected by variations in tumor blood perfusion, then the $k_{Larsson}$ may be approached by the Gd-uptake rate constant as defined by Tofts (12, 28) (k_{Tofts}). The uptake rate constant k_{Tofts} has a linear relationship with tracer transport across the vascular endothelium (PS_p-product) and an inverse relationship with the distribution volume of the tracer in the volume of interest. In such a case, the slope of Figure 3.5 equals the apparent vascular permeability (P) divided by the distribution volume of the tracer per voxel (V_d). The use of the term apparent vascular permeability is preferable, since Gd-uptake rates were obtained from homogeneously and heterogeneously perfused voxels. In heterogeneously perfused voxels, the tracer may have arrived from nearby capillaries, and may have arrived by diffusion through the extracellular volume from more distant perfused microvessels, which overestimates the calculations of the vascular permeability. The distribution volume (V_d) of Gd in perfused voxels was approximately 25 ± 1.5 (SD) % and equals the extracellular volume corrected for the vascular volume, which varied between 1.5 ± 0.5 (SD) % and 2.4 ± 0.7 (SD) %. Thus, consequently the cellular volume fraction is close to 73 %, which is comparable to mean values found by K. Donahue et al in a mammary adenocarcinoma model (39). The apparent microvessel permeability (P) in voxel categories P and PH can now be calculated using the estimated V_d value and the slope of Figure 3.5: P = 6.10^{-5} cm.s^{-1}.

The vascular permeability for Gd and/or the PS_p-product was measured previously in gliomas growing in the rat brain (40, 41). However, the values found in these studies cannot be compared directly to estimations of the vascular permeability or PS_p-product in the present study, because the PS_p-product was estimated using a simple graphical method of Patlak et al (42). The latter method assumes that the reflux of Gd from the tumor interstitium back into the microvessels can be neglected (unidirectional two-compartment model). However, in our study, changes of the Gd-concentration in the extravascular volume of the tumor were not linear during the time of the Gd-uptake experiments. This means that the reflux of Gd from the tumor interstitium back into the microvessels should be taken into account, see the models of Tofts or Larsson (11, 12). In studies on the quantitation of blood-brain barrier permeability in patients with multiple sclerosis lesions using a comparable MR-method and pharmacokinetic model as applied in this study, permeability constants in a range of 0.4 - $1.7.10^{-5}$ cm.s^{-1} were found (12). These values are smaller than our estimations of the permeability of the blood-brain barrier in 9L-gliomas, which may be explained among others by differences in the disruption of the blood-brain barrier.

The linear relationship between Gd-uptake rates and the perfused vascular surface-area indicates that Gd-uptake rates are not affected by variations in tumor blood perfusion (TBP). The relationships between Gd-uptake rates, PS_p-product and TBP are now analyzed using the single-capillary model of Larsson (11). In this way, information can be obtained on the range of TBP values, which may affect the linear relationship between $k_{Larsson}$ and PS_p-product. Estimates of the vascular permeabilty in this paper and the tracer distribution volume in voxels of vital tumor regions permit simulations of these relationships (Figure 3.6). In these simulations, the TBP was varied between 0 and 4 times the maximum PS_p-product found in the present study (= product of the apparent vascular permeability and the maximum S_p value). In addition, information on the range of $k_{Larsson}$ values was used, since $k_{Larsson}$ values larger than 0.021 s^{-1} were not detected in perfused voxels. In Figure 3.6, it is shown that the relationship between $k_{Larsson}$ and the PS_p-product becomes slowly linear when

the TBP is larger than the PS_p-product. Thus, the linear relationship between $k_{Larsson}$ and S_p can only be explained when the TBP is larger than the PS_p-product in the different voxels.
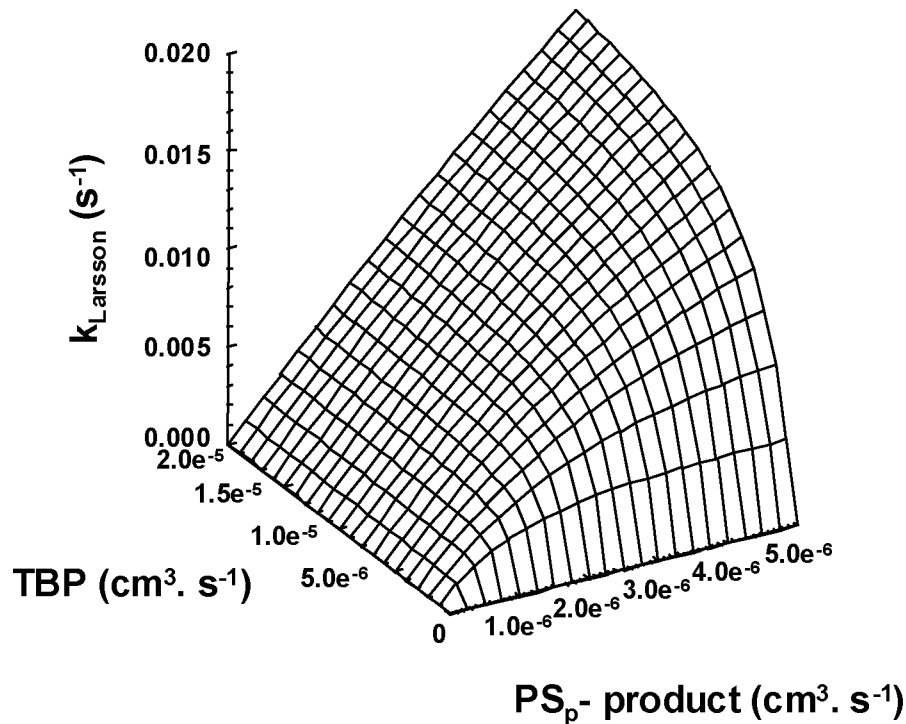

Figure 3.6 Surface-plot of correlations between the permeabilty surface-area product (PS_p-product, x-axis), tumor blood perfusion (TBP, y-axis) and Gd-uptake rate constants ($k_{Larsson}$, z-axis) using the definition of the rate constant k as proposed by Larsson et al (11): $k_{Larsson} = E \times TBP/V_d$. The distribution volume (V_d) of the tracer in the extracellular volume of perfused voxels (1 mm^3) was 25 % in these simulations.

Pratical applications: If Gd-uptake rates in voxels with perfused microvessels are governed by the perfused vascular surface-area or indirectly by the perfused vascular density, then quantification of these Gd-uptake rate constants may help to monitor noninvasively the effect of an anti-angiogenic therapy (8, 16). The latter therapy should not decrease the TBP in such a way that it becomes equal to or smaller than the PS_p-product, but should only have an effect on the number of perfused microvessels or vascular surface-area. Furthermore, the early enhancement of Gd in apparent Gd-concentration maps was found to spatially correlate to the perfused microvessel distribution. This information may be used in the prediction phase before radiotherapy or chemotherapy, since both treatments depend among others on the delivery of oxygen and drugs, respectively, via functional microvessels. Nonperfused hypoxic tumor regions were not enhanced in $r_1[Gd]$ maps, and therefore these maps provide additional information on tumor areas which depend on oxygen and drug supply by diffusion (see the immunohistochemical analyses of chronically hypoxic cells). Therefore, areas in $r_1[Gd]$-maps which are not enhanced may be less sensitive to radiotherapy (42) or chemotherapy.

Conclusions. In whole tumor sections through the center of 9L-gliomas in the rat brain, a spatial correlation was found between the apparent Gd-concentration and the 2D distribution of perfused microvessels. In perfused voxels, the Gd-uptake rates were linearly related to the perfused microvessel density and vascular surface-area. The latter relationship indicates that Gd-uptake rates do not depend on variations of the tumor blood perfusion and vascular permeability. Therefore, quantification of Gd-uptake rates has potential to monitor noninvasively the effect of a therapy on the perfused microvessels density or vascular surface-area.

References

1. Weidner N, Semple JP, Welch WR, Folkman J. Tumor Angiogenesis and Metastasis Correlation in invasive Breast Carcinoma. *The New England J of Medicine* **324**: 1-8 (1991).

2. Folkman J. What is the evidence that tumors are angiogenesis dependent? *J Natl Cancer Inst* **8**: 4-6 (1990).

3. Weidner N, Folkman J, Pozza F, et al. Tumor Angiogenesis: A New Significant and Independent Prognostic Indicator in Early-Stage Breast Carcinoma. *J Natl Cancer Inst* **84**: 1875-1887 (1992).

4. Gasparini G, Harris AL. Clinical importance of the determination of tumor angiogenesis in breast carcinoma: much more than a new prognostic tool: review. *J Clin Oncol* **13**: 765-782 (1995).

5. Bosari S, Lee AK, DeLellis RA, et al. Microvessel Quantitation and Prognosis in Invasive Breast Carcinoma. *Human Pathol* **23**: 755-761 (1992).

6. Brawer MK, Deering RE, Brown M, Preston SD, Bigler SA. Predictors of pathologic stage in prostatic carcinoma. The role of neovascularity. *Cancer* **73**: 678-687 (1994).

7. Weidner N, Folkman J. Tumoral Vascularity as a Prognostic Factor in Cancer. In: Important Advances in Oncology, Devita VT, Hellman S, Rosenberg SA, eds., Philadelphia, Pa.: Lippincott-Raven Publisher: 167-190 (1996).

8. Pass TJ, Bluemke DA, Siegelman SS. Tumor Angiogenesis: Tutorial on Implications for Imaging. *Radiology* **203**: 593-600 (1997).

9. Vaupel PW. Blood Flow, Oxygenation, Tissue pH Distribution, and Bioenergetic Status of Tumors. Information and Standards Medical Scientific Publications, ed., Berlin, Germany, Pa: Ernst Schering Res. Foundation: 8 (1992).

10. Elster AD, Jackels SC, Allen NS, Marrache RC. Europium-DTPA: a gadolinium analogue traceable by fluorescence microscopy. *Am J of Neuroradiology* **10(6)**: 1137–1144 (1989).

11. Larsson HBW, Stubgaard M, Frederiksen JL, Jensen M, Henriksen O, Paulson OB. Quantitation of Blood-Brain Barrier Defect by Magnetic Resonance Imaging and Gadolinium-DTPA in Patients with Multiple Sclerosis and Brain Tumors. *Mag Res Med* **16**: 117-131 (1990).

12. Tofts PS, Kermode AG. Measurement of the Blood-Brain Barrier Permeability and Leakage Space Using Dynamic MR Imaging. 1. Fundamental Concepts. *Mag Res Med* **17**: 357-367 (1991).

13. Barentsz JO, Berger-Hartog O, Witjes JA, et al. Evaluation of Chemotherapy in Advanced Urinary Bladder Cancer with Fast Dynamic Contrast-enhanced MR Imaging. *Radiology* **207**: 791-797 (1998).

14. Furman-Haran EF, Margalit R, Maretzek AF, Degani H. Angiogenic Response of MCF7 Human Breast Cancer to Hormonal Treatment: Assessment by Dynamic Gd_DTPA-enhanced MRI at High Spatial Resolution. *JMRI* **1**: 195-202 (1996).

15. Kennedy SD, Szczepaniak LS, Gibson SL, Hilf R, Foster TH, Bryant RG. Quantitative MRI of Gd_DTPA Uptake in Tumors: Response to Photodynamic Therapy. *Mag Res Med* **31**: 292-301 (1994).

16. Brasch R, Pham C, Shames D, et al. Assessing Tumor Angiogenesis Using Macromolecular MR Imaging Contrast Media. *JMRI* **7**: 68-74 (1997).

17. Hulka CA, Edmister WB, Smith BL, et al. Dynamic Echo-Planar Imaging of the Breast: Experience in Diagnosing Breast Carcinoma and Correlation with Tumor Angiogenesis. Radiology **205**: 837-842 (1997).

18. Hulka CA, Smith BL, Sgroi DC, et al. Benign and Malignant Breast Lesions: Differentiation with Echo-planar MR Imaging. *Radiology* **197**: 33-38 (1995).

19. Buadu LD, Murakami J, Murayama S, et al. Breast Lesions: Correlation of Contrast Medium Enhancement Patterns on MR Images with Histopathologic Findings and Tumor Angiogenesis. *Radiology* **200**: 639-649 (1996).

20. Buckley DL, Drew PJ, Mussurakis S, Monson JRT, Horsman A. Microvessel density in invasive breast cancer assessed by dynamic Gd-DTPA enhanced MRI. *JMRI* **7**: 461-464 (1997).

21. Rozijn TH, van der Sanden BPJ, Heerschap A, Creyghton JHN, Bovée WMMJ. Influence of the pharmacopharmacokinetic model on the quantification of the Gd_DTPA uptake rate in brain tumours using direct T_1 measurements. *MAGMA* **6**: 37–43 (1998).

22. Kennedy AS, Raleigh JA, Perez GM, Calkins DP, Thrall DE, Novotny DB, Varia MA. Proliferation and hypoxia in Human squamous cell carcinoma of the cervix: First report of combined immunohistochemical assays. Int J of Radiation Onc Biol Phys **37**: 897–905 (1997).

23. Rijken PFJW, Bernsen HJJA, van der Kogel AJ, Application of an image analyses system to the quantitation of tumor perfusion and vascularity in human glioma xenografts. *Microvascular Res* **50**: 141–153 (1995).

24. Deichmann R, Haase A. Quantification of T_1 Values by SNAPSHOT-FLASH NMR Imaging. *J of Mag Res* **96**: 608-612 (1992).

25. Bevington PR, Data reduction and error analyses for the physical science. N-Y, San Francisco, St. Louis, Toronto, London, Sydney, Pa: McGraw-Hill Book Company: 237–239 (1969).

26. Strich G, Hagan PL, Gerber KH, Slutsky RA. Tissue Distribution and Magnetic Spin Lattice Relaxation Effects of Gadolinium-DTPA. *Radiology* **154**: 723–726 (1985).

27. Press WH, Flannery BP, Teukolsky SA, Vetterling WT. Numerical Recipes in C: The Art of Scientific Computing 2nd ed, Press WH, Flannery BP, Teukolsky SA, Vetterling WT, eds, Cambridge, N-Y, Chester, Melbourne, Sydney, Pa: Cambridge University Press: p. 309–317 (1988).

28. Larsson HBW, Tofts PS. Measurements of blood-brain barrier permeability using dynamic Gd_DTPA scanning - A comparison of methods. *Mag Res Med* **24**: 174-176 (1992).

29. Adair TH, Wellis ML, Hang J, Montani J-P. Stereological method for the estimating length density of the arterial vascular system. *Am J of Physiology* **266**: H1424-H1438 (1994).

30. Honig CR. Dimensions and Maximum Diffusion Distance of Capillaries: Vertebrate tissue. In : Respiration and Circulation, Biological Handbooks, Altman PL, Dittmer DS, eds, Bethesda, USA, Pa : Federation of American S. for Experimental Biology: p. 454 (1971).

31. Barentsz JO, Jager GJ, van Vierzen PBJ et al. Staging Urinary Bladder Cancer after Transurethral Biopsy: Value of Fast Dynamic Contrast-enhanced MR Imaging. *Radiology* **201**: 185-193 (1996).

32. Furman-Haran E, Grobgeld D, Degani H. Dynamic Contrast-Enhanced Imaging and Analyses at High Spatial Resolution of MCF7 Human Breast Tumors. *J of Mag Res* **128**: 161–171 (1997).

33. Hittmair K, Gomiscek G, Langenberger K, et al. Method for the Quantitative Assessment of Contrast Agent Uptake in Dynamic Contrast-Enhanced MRI. *Mag Res Med* **31(5)**: 567 – 571 (1994).

34. Rozijn TH. MRI techniques for tissue perfusion and vascular permeability measurements. PhD-thesis, University of Technology Delft: p. 151 (1998).

35. Artemov D, Bhujwalla ZM. 3-Dimensional MRI Quantitation of Tumour Vascular Volume and Permeability. Proceedings of the Int. Society for Magnetic Resonance in Medicine, 5th Meeting, Vancouver, Canada: p. 491 (1997).

36. Demsar F, Roberts TPL, Schwickert HC et al. A MRI Spatial Mapping Technique for Microvascular Permeability and Tissue Blood Volume Based on Macromolecular Contrast Agent Distribution. *Mag Res Med* **37**: 236–242 (1997).

37. Su M-Y, Najafi A, Nalcioglu O. Regional Comparison of Tumor Vascularity and Permeability Parameters Measured by Albumin-Gd-DTPA and Gd-DTPA. *Mag Res Med* **34**: 402–411 (1995).

38. Degani H, Gusis V, Weinstein D, Fields S, Strano S. Mapping pathophysiological features of breast tumors by MRI at high spatial resolution. *Nature Medicine* **13(7)**: 780–782 (1997).

39. Donahue KM, Weisskoff RM, Parmelee DJ, Callahan RA, Wilkinson RA, Mandeville JB, Rosen BR. Dynamic Gd-DTPA Enhanced MRI measurements of Tissue Cell Volume Fraction. *Mag Res Med* **34**: 423–432 (1995).

40. Kenney J, Schmiedl UP, Maravilla K, Starr F, Graham M, Spence A, Nelson J. Measurement of Blood-Brain Barrier Permeability in a Tumor Model Using Magnetic Resonance Imaging with Gadolinium-DTPA. *Mag Res Med* **27**: 68–75 (1992).

41. Schmiedl UP, Kenney J, Maravilla KR. Kinetics of Pathologic Blood-Brain-Barrier Permeability in an Astrocytic Glioma Using Contrast-Enhanced MR. *Am J of Neuroradiology* **13**: 5–14 (1992).

42. Patlak CS, Blasberg RG, Fenstermacher JD. Graphical evaluation of blood-to-brain transfer constants from multiple-time uptake data. *J Cereb, Blood Flow Metab* **3**: 1-7 (1983).

43. Denekamp J. Does physiological hypoxia matter in cancer therapy? In: The Biological Basis of Radiotherapy. Steel GG, Adams MJ, eds, Amsterdam, New York, Oxford, Pa: Elsevier: p. 139–155 (1983).

Chapter 4

Global HDO-uptake as measured by ^{2}H-MRS is related to the perfused capillary distribution in human glioma xenografts

Boudewijn P.J. van der Sanden
Henricus J.A. in 't Zandt
Louis Hoofd
Robin A. de graaf
Klaas Nicolay
Paul F.J.W. Rijken
Albert J. van der Kogel
Arend Heerschap

Abstract

The aim of this study is to evaluate the existence of a possible relationship between global HDO-uptake rates and the diffusion geometry of human glioma xenografts in nude mice.

HDO diffusion times in the whole extravascular tumor volume were estimated by combining quantitative ^{1}H-MR diffusion imaging and morphometrical analyses of intercapillary distances in 2 tumor lines with a different perfused vascular architecture. HDO-uptake was measured independently using ^{2}H-MRS. Uptake time constants (τ) were compared to estimations of maximum HDO diffusion times (t_{difmax}).

Tumors with a homogeneously perfused capillary distribution showed a mono-exponential HDO uptake. The t_{difmax} was comparable to τ's of HDO-uptake curves: t_{difmax} varied between 74 and 368 s and the range of τ's was 115 - 370 s. Heterogeneously perfused tumors had a bi-exponential HDO uptake with t_{difmax} in between the τ's of the fast and slow uptake phase.

These findings indicate that the global HDO uptake is related to the perfused capillary distribution in human glioma xenografts. That HDO-uptake rates indeed can depend on the perfused capillary distribution was substantiated in experiments with 2D models. In these models with a diffusion-limited HDO-uptake, HDO-uptake curves could be approximated by curves derived from 2D HDO-diffusion simulations.

Introduction

Tumor blood perfusion can determine among other physiological parameters the sensitivity of a tumor to radiotherapy and/or chemotherapy. Manipulations of tumor blood perfusion (TBP) may enhance the sensitivity of a tumor for a particular treatment. Therefore, information on TBP can help to select the most suitable treatment modality.

^{2}H-magnetic resonance spectroscopy (^{2}H-MRS) and imaging studies (^{2}H-MRI) of HDO uptake and HDO clearance in tumor tissue have frequently been used for the determination of TBP (1-8). ^{2}H-MRI has been used to study regional HDO-uptake and TBP (3, 5 ,8), whereas ^{2}H-MRS has been used to analyse the global HDO-uptake in the whole tumor volume (1, 2, 4, 7). Generally the time to reach tracer concentration equilibrium between the vascular - and extravascular compartment is supposed to be instantaneous and TBP can be derived from HDO-uptake rates using the Kety model (9). However, the assumption that HDO uptake is perfusion-limited has to be verified for every application (10).

The HDO uptake may become diffusion-limited at high perfusion rates (10) and/or in tissue with a significant fraction of large intercapillary distances. The Kety model as well as other kinetic models (11-13) which were used for the interpretation of tracer-uptake studies include tracer diffusion through the vascular endothelium per unit tissue volume (permeability surface-area product (9, 12, 13), but ignore tracer diffusion in the extravascular space. In normal and tumor tissue, the permeability surface-area product for HDO is sufficiently high relative to TBP (14). In addition, diffusion distances between capillaries in normal tissue are small (approximately 50 μm (15, 16)), so that the characteristic time of HDO diffusion is short in comparison to the capillary transit time of the tracer (perfusion-limited uptake, (8)). However, in tumors with extended hypoxic and necrotic areas a significant fraction of large intercapillary distances exist, which may decrease the time to reach tracer equilibrium by diffusion between the perfused and nonperfused regions. Tracer diffusion distances between perfused capillaries in the whole tumor volume have never been analyzed so far.

Detailed information on the pattern of tracer delivery is important in the context of radiotherapy and chemotherapy. The lack of O_2 or chemotherapeutic agents in tumor tissue can be due to the presence of regions with low TBP or of nonperfused regions, characterized by large diffusion distances between perfused capillaries. In the first case, an increase of the tumor oxygenation or drug delivery may be achieved by an improvement of the TBP. However, such a treatment modulation will not be effective in the second case (17).

The aim of this study is to investigate the existence of a possible relationship between HDO-uptake rates and HDO diffusion times in the extravascular space of two different human glioma xenograft lines with a homogeneously and heterogeneously perfused vascular architecture. HDO diffusion times were estimated combining quantitative ^{1}H-MR diffusion imaging (18) and two-dimensional morphometrical analyses of intercapillary distances between perfused capillaries in complete transverse tumor sections (19). Maximum HDO-diffusion times were related to time constants of HDO-uptake curves as measured independently with ^{2}H-MRS. A linear correlation was found between the maximum HDO-diffusion times and the time constants of the HDO-uptake. To obtain a better understanding of the relation between HDO-uptake rates and HDO diffusion times in the extravascular volume, HDO-uptake curves of 2D models with anisotropic capillary distribution were compared to curves derived from two-dimensional HDO diffusion simulations. As models we used blood filters, which contained bundles of parallel, perfused capillaries and which showed diffusion-limited HDO uptake. Intercapillary distances were varied and the effect on HDO-uptake rates was studied by ^{2}H-MRS. A good approximation of HDO-uptake curves in all blood filters was obtained by the simulation of 2D HDO diffusion.

Material and Methods

In vivo studies.

Animal model. Two tumor lines (E49 and E98), with a different perfused vascular architecture and derived from two different primary human gliomas, were grown subcutaneously in the hind limb of athymic mice (Balb/c nu/nu, BonholdGard Denmark). The E49 line was more heterogeneously perfused than the E98 line (20). Cannulae (Neoflon $\emptyset$ 0.6/19mm, 24 G) were inserted in a tail vein for online administration of D_2O. Mice were anaesthetized by exposure to 1.5 % enflurane in an O_2/N_2O (3:7) mixture applied through a nose cone. Their body temperature was monitored with a rectal probe (36 G, Hewlett Packard) and maintained at 36.5° - 37° C by a warm water blanket with a feedback system. In ^{2}H-MRS experiments and in immunohistochemical analyses 10 E49 tumors and 9 E98 tumors were analyzed. In ^{1}H-MR diffusion experiments the same tumor lines but different tumors were used: 8 E49 tumors and 6 E98 tumors. The local ethical committee for animal use approved the experimental procedures.

Quantitative ^{1}H-MR diffusion imaging experiments. ^{1}H-MR diffusion experiments were performed on a horizontal-bore SISCO 200/400 spectrometer (4.7 T) with a 220 mT.m^{-1} gradient insert (rise time = 300 μs). A single 2.0 cm diameter, inductively coupled surface coil tuned to the proton frequency (200.1 MHz) was used for both RF transmission and reception. Before the diffusion experiments sagittal ^{1}H-SE images were made for the positioning of a coronal slice in the center of the tumor parallel to the surface coil. The following acquisition parameters were used: TR = 1.5 s, TE = 23 ms, matrix size 256 x 64, FOV 5 x 5 cm and slice thickness = 1.5 mm.

An adiabatic double spin-echo sequence (21) was used for the measurement of apparent diffusion coefficients of water in tumors, using the following acquisition parameters: TR = 2.5 s, TE = 65 ms, matrix size = 256 x 128, FOV = 2.5 x 2.5 cm and slice thickness = 1.5 mm. Signal excitation was performed with a non-selective adiabatic half passage pulse (pulse length = 1.0 ms) (22) while frequency selective refocusing was achieved with a pair of adiabatic full passage (AFP) pulses (23) (pulse length = 2.0 ms). Diffusion weighting was introduced by a pair of halfsine shaped gradients around each AFP pulse (gradient pulse length δ = 5 ms, separation of the gradients Δ = 19 ms). Apparent diffusion coefficients of water (ADC$_w$) were obtained by fitting 5 separate diffusion measurements (b = $2.(2/\pi)^2.\gamma^2.G^2.\delta^2.(\Delta - \delta/4)$) : 33, 179, 441, 821, 1317 s/cm^2, where γ is the gyromagnetic ratio and G the maximum gradient amplitude) with a mono-exponential curve (18).

Data analyses. Per tumor, a mean ADC$_w$ (mADC$_w$) for all voxels of the ADC$_w$ map was calculated. For calculations of the maximum diffusion time (see Eq. [3]) an average ADC$_w$ value of all tumors was used. The average ADC$_w$ is defined as the average of all mean ADC$_w$ values of both tumor series.

^{2}H-Magnetic Resonance Spectroscopy. ^{2}H-MRS measurements were performed on a vertical-bore Bruker spectrometer (4.7 T) employing a home-built ^{1}H/^{2}H double tunable 3-turn solenoid coil with an inner diameter of 13 mm. The solenoid coil was fitted with a Faraday shield to eliminate spurious signals from normal tissue adjacent to the tumor. Mice, with human glioma xenografts, were excluded if host tissue was partially present in the volume sampled by the solenoid (tumor weight < 0.3 g) and when tumors did not fit completely in the solenoid (tumor weight > 0.9 g). ^{2}H-MRS spectra were obtained with a one-pulse sequence using a flip angle of

10°, TR = 766 ms and number of scans = 64. An i.v. bolus injection of 0.1 ml PBS D_2O solution was given after the acquisition of the third of 100 serial 49-s ^{2}H-MR spectra.

The HDO concentration in blood plasma after an i.v. bolus injection of 0.1 ml PBS HDO solution was analyzed by cannulating the carotid arteries of 3 mice. Starting one min after injection, 8 blood samples (20 µl) were taken at 10 min intervals. The samples were diluted in 600 µl saline. The HDO concentration in the diluted blood samples was determined with in-vitro ^{2}H-MRS using a standard HDO solution for calibration.

Data analyses. ^{2}H-MR spectra were obtained after applying zero filling and exponential line broadening (10 Hz) to the free induction decay. The HDO peaks were fitted to Lorentzian lineshapes with NMR1 software (New Methods Research, Inc., Syracuse, NY, USA). Relative HDO amount changes in time were estimated from HDO peak integrals. Next, HDO-uptake curves were fitted to a minimum number of exponential terms. The F-test was used to distinguish between mono-exponential or bi-exponential HDO uptake, see Eq. [1] and [2], using Graphpad software (Graphpad PRISM version 2.0, San Diego, USA). In Eq. [2] A and B are defined as weight factors belonging to the exponential components with the largest (k_1) - and smallest rate constant (k_2), respectively. After fitting the HDO curves to Eq [1] or [2] the HDO peak integrals were normalized to the value of A or to the sum of the A and B value.

$$f(A,k;t) = A.(1 - e^{-k.t})$$ [1]

$$f(A,B,k_1,k_2;t)) = A.(1 - e^{-k_1.t}) + B.(1 - e^{-k_2.t})$$ [2]

The parameter τ = 1/k is called the time constant of mono-exponential uptake curves and equals the time (s) at which the amount of tracer corresponds to 63 % of its final value (= 0.63*A). Per tumor with mono-exponential or bi-exponential HDO uptake, values of τ (or weighted mean values of τ_1 and τ_2) were compared to estimations of maximum HDO diffusion times (t_{difmax}, see Eq. [3] and Figure 4.5). This approach was validated in model studies (Table 4.2).

Fluorescence Microscopy and two dimensional morphometrical analyses of perfused vascular architecture. In complete transverse tumor sections morphometrical analyses were employed, using a computer-controlled digital image analyses system connected to a fluorescence microscope. A detailed description of this method is given by Rijken et al (19). Briefly, after the ^{2}H-MRS experiments, a 0.05 ml solution of PBS (phosphate buffered saline, pH=7.4) containing a fluorescent perfusion marker Hoechst 33342 (15 mg/kg, Sigma chemical company, St.Louis, USA), was injected i.v. via a lateral tail vein. One minute after injection the mice were killed and tumors were quickly removed and frozen in liquid nitrogen preventing the redistribution of the dye. The tumor was cut in halves: one half was used for the analyses of perfused capillaries and the other half was used for classical histological staining with eosin (cytoplasm) and haematoxylin (nuclei). Fifteen frozen tissue sections (5 µm) at random locations were made using a freeze microtome. Sections were incubated at room temperature for 15 min with collagen Type IV polyclonal antibody (rabbit serum, Euro-Diagnostics BV, Oss, The Netherlands), a marker for the basal lamina of capillaries. Next, the sections were incubated with a second antibody, goat anti rabbit immunoglobulin labelled with Tritc (Tago-Inc., Birlingame, USA).

The complete transverse tumor sections were analyzed in the fluorescence microscope using a digital image processing system. Each section was scanned twice on a computer-controlled motorized stage of a fluorescence microscope using two different excitation/emission filters. After processing all fields of each scan, a composite image was reconstructed from the individual processed fields revealing the perfused capillaries (Hoechst image) and the total capillary bed (Collagen image) in separate scans. When both images were combined, the new matched image showed the perfused - and nonperfused capillaries (see Figure 4.4A and 4.4C). In the next step the fluorescent rim of the Hoechst dye around perfused capillaries due to Hoechst diffusion into adjacent tissue was deleted by image processing.

Data analyses. For each perfused vessel a domain (defined in ref. (24)), i.e. the area of tumor tissue which is supposed to be supplied by the nearest perfused vessel, was determined in matched images containing only the perfused capillaries. As a consequence, one domain contains one perfused capillary and may contain nonperfused capillaries and avascular regions. Line networks as shown in Figure 4.1 represent the contours of these domains. Contours of domains (= lines in between perfused capillaries) were used to estimate intercapillary distances (icds), which were defined as the shortest distance between neighbouring perfused capillaries, crossing the contour lines perpendicularly (e.g. see arrow in Figure 4.1). Note that neighbouring perfused capillaries have adjacent domains. Thus, intercapillary distances were not determined between perfused capillaries which did not have adjacent domains.

A mean intercapillary distance (micd) was calculated for the largest icds found between perfused capillaries ($micd_{max}$) in all 15 sections per tumor, as verified in matched fluorescence images showing the perfused - and nonperfused capillaries. Half of the $micd_{max}$ was used as an estimate of maximum diffusion distances between perfused capillaries adjacent to nonperfused regions (see Eq. [3]). Nonperfused tumor regions are defined by a small number of large icds in comparison with perfused regions, which contain a large number of small icds (see Figure 6.2 on page 96). If mean icds would have been used, then diffusion distances in the whole tumor volume were underestimated since approximately 70 % of the icds are shorter than 100 μm (perfused regions) but the small number of large icds determine HDO diffusion times from perfused into nonperfused regions. Note that global HDO-uptake measurements are sensitive to HDO diffusion processes in the whole tumor volume. For capillaries at the edge of a tumor section the shortest distance between perfused capillaries and the edge was taken as diffusion distance rather than half the intercapillary distance.

Estimation of maximum HDO-diffusion times between perfused capillaries.
Mean maximum intercapillary distances per tumor ($micd_{max}$, see previous paragraph) obtained from 2D data sets of 15 tissue sections and the average water ADC ($avADC_w$) were used to estimate maximum HDO-diffusion times (t_{difmax}). The Einstein equation for 2D diffusion, as given by Vaupel et al (26), was used for rough estimations of maximum diffusion times in tumor tissue slices, Eq. [3]:

$$t_{difmax} \sim \frac{(micd_{max}/2)^2}{4.avADC_w} \qquad \text{[3]}$$
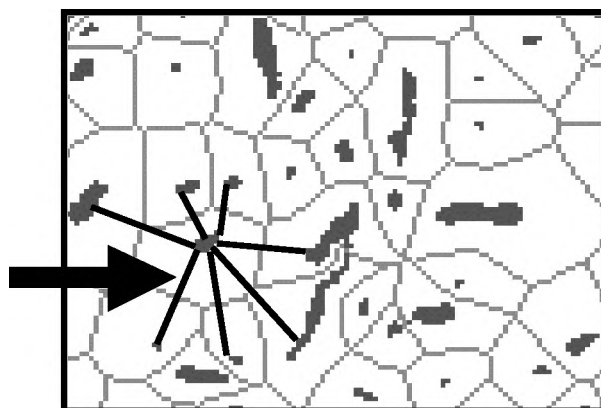
Figure 4.1 Detail of a matched digitized fluorescence image of a scanned tumor section. The black structures are cross-sectional areas of perfused capillaries. The grey lines, determined by the computer, are exact mid-lines between the vessel walls and represent the contours of vascular domains. These lines were used for the determination of the shortest distances (= intercapillary distances) between vessel walls (see black lines). The arrow indicates a shortest distance between two perfused capillaries.

Model studies

Model. Six blood filters were used as two-dimensional diffusion models (Pan H-10, Asahi Medical CO., LTD. Japan). Filters consisted of ~ 150 parallel perfused capillaries with a mean radius of 0.15 ± 0.01 mm and length of 10 ± 0.1 cm in a cylindrical volume of 10.4 ± 1 ml. The side ports for the counter flow were blocked; the tracer could only enter and leave the cylinder by the capillaries. The membranes of the capillaries (thickness ~5 μm) consisted of polyacrylonitril with pores which were highly permeable to small molecules such as HDO, but which excluded molecules with molecular weights larger than 24 - 25 kDa. The perfused capillary distribution in the blood filters was changed by blocking the capillaries at the inlet of the filter with plastic cylinders precisely fitting in the capillaries. Only filters with a comparable capillary distribution at the inlet (= capillary distribution used in the diffusion simulations) and in the cylindrical volume of the filter (= volume of interest during the ^{2}H-MRS experiments) were selected for ^{2}H-MRS experiments.

Blood filters were incorporated in an open system, see Figure 4.2A. The reservoir at the inlet of the pump contained a 10 % HDO solution in demi water (v/v). The water flow velocity in the system was determined by the pump (Fluid Metering Inc., Oyster Bay, NY, USA) which was able to generate constant flow velocities varying between 0.23 ml.s^{-1} and 4.5 ml.s^{-1}. The flow velocities were calibrated with an in-line device (Fluid Metering Inc., Oyster Bay, NY, USA). In most experiments the flow velocity was 2.46 ml.s^{-1}. At this flow velocity the mean capillary transit time of HDO molecules is 0.4 s (approximately the volume of capillaries (1 ml) divided by 2.46 ml.s^{-1}). The experiments were performed at room temperature: $20 \pm 0.3°$ C. The temperature was measured with a rectal probe in the reservoir at the inlet of the pump. At this temperature the self-diffusion coefficient for water is ~ 2.10^{-5} cm^2.s^{-1} (27, 28).

Deuterium Magnetic Resonance Spectroscopy (^{2}H-MRS). The ^{2}H-MRS experiments were performed on a 4.3 T, 7.5 cm diameter vertical-bore magnet equipped with an SMIS spectrometer (SMIS ltd. Guildford U.K.) employing a homebuilt double tunable ^{1}H/^{2}H Helmholtz coil with a diameter of 2 cm and a length of 3 cm.

The Helmholtz coil was situated around the middle of the blood filter to measure the HDO-uptake in the extracapillary volume of the blood filter (see Figure 4.2B).

^{2}H-MRS spectra were obtained with a one-pulse sequence with the following acquisition parameters: flip angle = 10°, TR = 1250 ms, number of scans = 2. Data were analyzed as described in the first 4 sentences of the paragraph data analyses of in vivo ^{2}H-MRS studies.

Simulation of diffusion. Photographs of the 2D capillary distribution at the inlet of normal and modified blood filters were digitized using a digital-image processing system (19). The Cartesian coordinates of the capillaries were determined and set into a 2D matrix with a grid size of 53 x 53 pixels. At this size the cross-sectional area of one capillary corresponds to one pixel. An octagon approximated the circular boundary of the filter inlet. For a constant supply of tracer, the 2D diffusion of HDO was simulated by solving Fick's law numerically using Matlab® (see appendix and ref. 29). The sum of all pixels was taken per time step and represented the total amount of HDO in the volume of interest per time unit, similar to ^{2}H-MRS experiments. The HDO concentration gradients at the edge of the filter were set to zero since there was no diffusion to the outside of the filter. For the simulation of diffusion the following assumptions were made:

1. The diffusion coefficient was independent of time and location.
2. Capillaries were considered perfectly parallel in the cylindrical volume of the filter. In this way, HDO-uptake experiments can be compared with 2D diffusion simulations.
3. The HDO concentration in the capillary was considered independent of the distance from the inlet of the filter.
4. The diffusion of HDO molecules across the capillary membrane was supposed to be isotropic and not to be hindered by the porous structure of the wall.
5. Axial diffusion in the extracapillary space of the filter was not taken into consideration. For HDO-uptake experiments the Helmholtz coil was situated in the middle of the blood filter minimizing the effect of axial diffusion since a loss of tracer at the outlet of the volume of interest is compensated at the inlet.
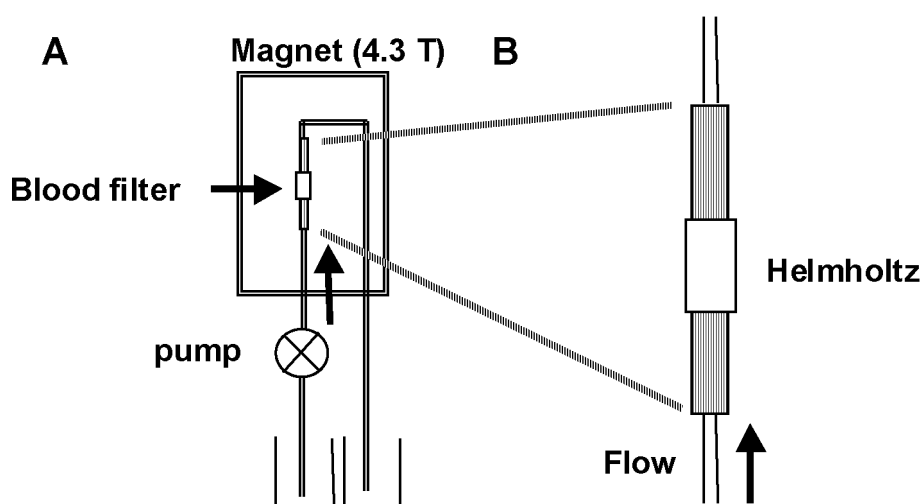

Figure 4.2 Schematic representation of the setup for model studies (Figure 4.2A). The reservoir at the inlet of the pump contained a 10 % HDO solution in demi water (v/v). The Helmholtz coil was situated around the middle of the blood filter (see Figure 4.2B).

Results

In vivo studies

Analyses of the water apparent diffusion coefficients (ADC$_w$) in tumor tissue.

An example of a ADC$_w$ map of a coronal slice through the center of a tumor (E49) is shown in Figure 4.3. The signal intensity per voxel is directly related to the ADC$_w$. Tumors from both lines showed an ADC$_w$ range from 4.10^{-6} cm^2.s^{-1} to 14.10^{-6} cm^2.s^{-1}. No significant difference was observed between the mean ADC$_w$ of both tumor lines (paired t-test, p = 0.07). For further calculations, an average ADC$_w$ value ($8.4.10^{-6}$ ± $2.4.10^{-6}$ (SD) cm^2.s^{-1}) derived from mean ADC$_w$ values of all tumors of both lines was used.

Figure 4.3 A representative water apparent diffusion coefficient (ADC$_w$) map of a slice through the center of an E49 tumor. The intensities are directly related to ADC$_w$ values, which varied from 6.10^{-6} cm^2.s^{-1} to $9.3.10^{-6}$ cm^2.s^{-1} in this example.

12x10^{-6}

6x10^{-6}

0
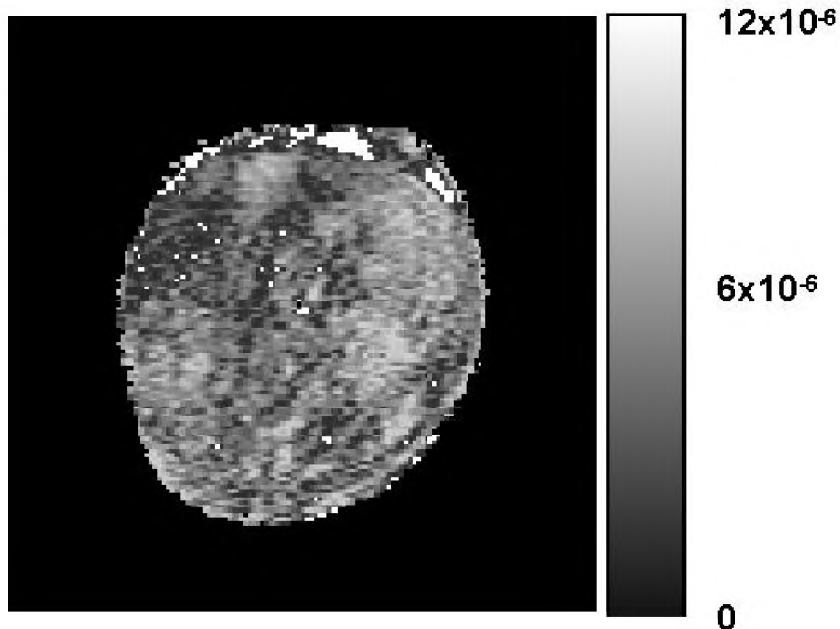
Morphometrical analyses of the 2D perfused vascular architecture and intercapillary distances.

In comparison to skeletal muscle, human glioma xenografts have asymmetrical intercapillary distance (icd) distributions with a long tail of large icds (see 25 and Figure 6.2, chapter 6). Composite digital fluorescence images of scanned tumor sections and corresponding HDO-uptake curves of 2 representative tumors of each line are displayed in Figures 4.4. The perfused capillaries are shown in white. Tumor E49, no.5 represents one of the least perfused tumors in this study: a large area in the center of the tumor was not perfused (Figure 4.4A). This tumor had a bi-exponential HDO uptake, see Figure 4.4B. E98 tumor in Figure 4.4C had a more homogeneously perfused vascular architecture with a mono-exponential HDO uptake (Figure 4.4D). Note that the time scale in Figure 4.4D is different from Figure 4.4C. In general, E49 tumors had a more heterogeneously perfused vessel distribution than E98 tumors. Most E49 tumors were found to have larger maximum intercapillary distances than E98 tumors (Table 4.1, column 3).
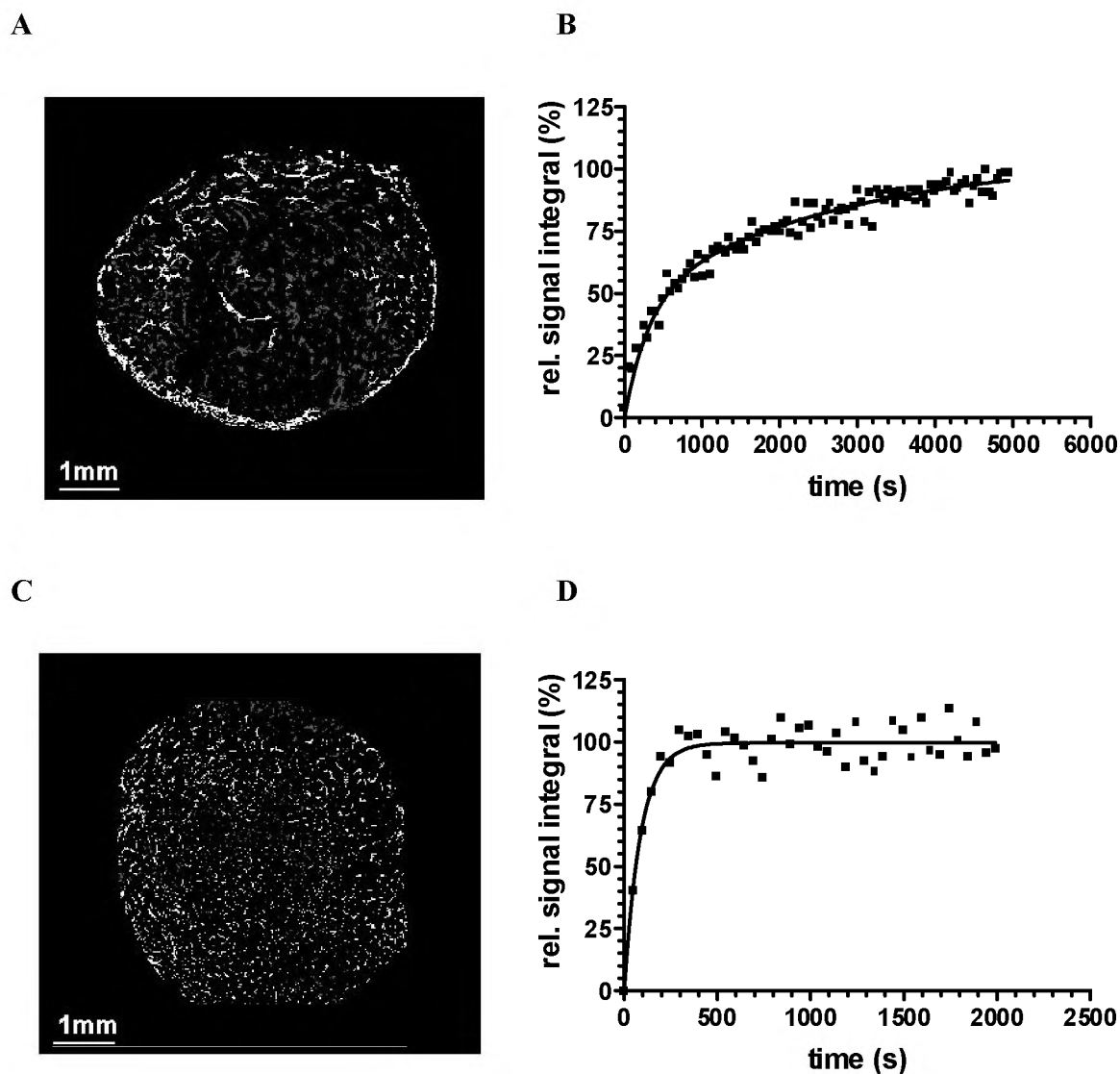
A

B

C

D

Figure 4.4 Digitized and processed fluorescence images of a coronal section through the center of two representative E49 (**4.4B**) and E98 tumors (**4.4C**) showing perfused capillaries (white structures) with the corresponding HDO-uptake curves of the whole tumor (**Figure 4.4B and 4.4D**). In the HDO-uptake curve, data points represent normalized integrals of HDO peaks, and the solid line is the result of a least-square bi-exponential regression analyses of the data. All values reported hereafter are means $\pm$ SE. The results of the regression analyses are (Fig. 4.4B, bi-exp.: F-ratio = 9.8 and p = 1.3. 10^{-4}): R^2 = 0.96, A = 80 $\pm$ 10 %, B = 20 $\pm$ 2 %, k_1 = 1.4. $10^{-3} \pm 4.10^{-4}$ s^{-1}, k_2 = 1.7. $10^{-4} \pm 5$. $10^{-5}s^{-1}$. The results of the regression analyses in Fig. 4.4D are: mono-exp. , R^2 = 0.88, k = 1.1. $10^{-2} \pm 1.2$ 10^{-3} s^{-1}.

Comparison between maximum diffusion times and the time constants of the HDO-uptake curves.

HDO diffusion times for maximum icds as estimated using Eq. [3] are given in column 4 of Table 4.1. The time constants τ, τ_1 and τ_2 (s) for mono-exponential or bi-exponential HDO uptake as obtained after fitting to Eq. [1] or [2] are included in columns 5 and 6, respectively. For mono-exponential HDO-uptake curves, τ had the same order of magnitude as t_{difmax}, especially for the E98 tumors: no.12 - no.16. Most E98 tumors showed a mono-exponential uptake and most E49 tumors a multi-exponential HDO uptake. For bi-exponential HDO-uptake curves, t_{difmax} was in between τ_1 and τ_2. The correlation between t_{difmax} and τ or the weighted mean of τ_1 and τ_2 (τ_w) is further illustrated in Figure 4.5.

For multi-exponential HDO-uptake curves, the HDO concentration in tumor tissue was not in equilibrium with the HDO concentration in blood after 80 minutes. However, 8 blood samples taken at 10 min intervals from the carotid arteries of 3 mice, starting one minute after bolus injection of D_2O, showed a steady state HDO concentration for all samples (results not shown).

Table 4.1 Comparison between estimated maximum diffusion times (t_{difmax}) and time constants of HDO-uptake curves in E49 and E98 tumors of different weight (w). In column 4, maximum diffusion times (t_{difmax}) are calculated using $micd_{max}$ (column 3) and the average ADC_w of $8.4.10^{-6}$ $cm^2.s^{-1}$, see Eq.[3]. In column 5 and 6, time constants for mono-exponential (τ) or multi-exponential HDO-uptake curves (τ_1 and τ_2) are given, see further details in text. All values are depicted with their SE.

Table 4.1

|	no.	w (g)	$micd_{max}$ (μm)	t_{difmax} (s)	τ or τ_1 (s)	τ_2 (s)
E49	1	0.35	1783 ± 78	237	370 ± 10	
	2	0.42	1800 ± 66	241	249 ± 15	1115 ± 200
	3	0.36	1820 ± 80	246	117 ± 17	685 ± 111
	4	0.42	3000 ± 57	670	99 ± 91	567 ± 170
	5[a]	0.63	3775 ± 53	1060	714 ± 20	5882 ± 386
	6	0.90	2911 ± 68	631	161 ± 22	1904 ± 244
	7	0.41	1893 ± 86	267	123 ± 19	1381 ± 176
	8	0.34	2784 ± 110	577	116 ± 23	974 ± 118
E98	11	0.64	997 ± 40	74	172 ± 20	
	12[b]	0.27	1267 ± 63	119	89 ± 12	
	13	0.37	1549 ± 80	179	226 ± 25	
	14	0.90	2223 ± 89	368	363 ± 29	
	15	0.87	1633 ± 65	198	175 ± 16	
	16	0.68	1100 ± 55	90	115 ± 10	
	17	0.82	1405 ± 70	147	81 ± 7	649 ± 71
	18	0.90	2042 ± 102	310	150 ± 17	1462 ± 117

[a] see Figure 4.4A, [b] see Figure 4.4C
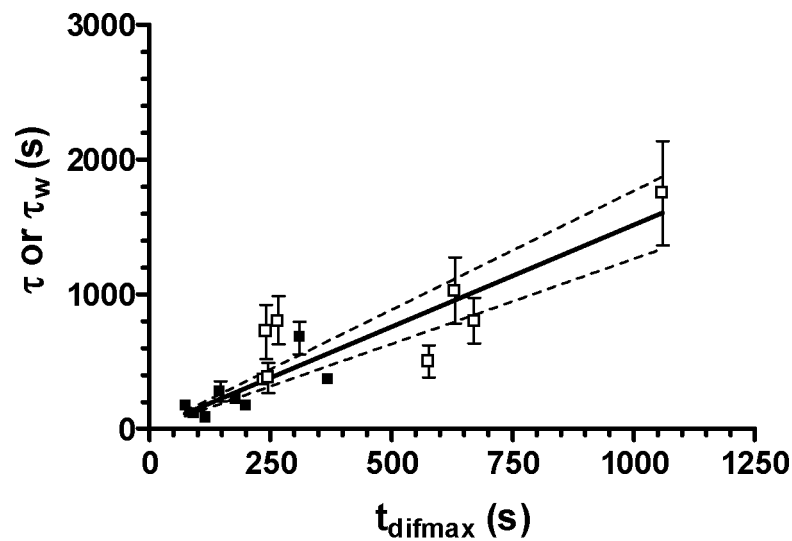
Figure 4.5 Plot of the correlation between time constants of mono-exponential HDO-uptake curves (τ, s) or weighted mean time constants (τ_w, s) of bi-exponential HDO-uptake curves and the estimated t_{difmax} (s) for the tumor lines E49 ($\square$) and E98 ($\blacksquare$) (One square represents one tumor). In the case of bi-exponential uptake, the weight factors A and B (see Eq. (2)) were used for calculations of the τ_w ($= (A^*\tau_1 + B^*\tau_2)/(A+B)$). The line indicates the results of the least-squares linear regression analyses ($R^2 = 0.92$): time constant $= 1.5 \pm 0.12$ (SD) * t_{difmax}. The regression line was forced to go through zero. The dashed line shows the 95 % confidence intervals. Error bars reflect SE.

Model studies

Measurements of the HDO uptake in the middle of unmodified blood filters.

In order to validate the blood filters as models for diffusion-limited HDO uptake, the HDO uptake in the middle of filters was measured at different flow velocities: 0.91, 1.55 and 2.46 ml.s^{-1}. The rate constants of HDO-uptake curves (k) at these flow velocities in e.g. filter 3 were 0.021 ± 0.001 (SE), 0.027 ± 0.0003 and 0.028 ± 0.002, respectively. In all filters, the HDO-uptake rate constants for the largest flow velocities were not significant different, because the HDO-uptake rates were limited by diffusion. The largest flow velocity was used in the following studies.

Comparison of the time constants of HDO-uptake curves with maximum diffusion times of HDO in unmodified blood filters.

Comparable to the procedure used for the in vivo studies, the rate constants of HDO-uptake curves were compared to maximum diffusion times of HDO in the extracapillary volume of unmodified blood filters. The maximum diffusion time (t_{difmax}) was estimated using the mean maximum intercapillary distance ($micd_{max}$) in unmodified blood filters with mono-exponential HDO-uptake curves. Mean maximum intercapillary distances of the unmodified blood filters (see Table 4.2, column 2) were in between mean maximum intercapillary distances found in human glioma xenografts, which varied between 997 μm and 3775 μm.

The maximum diffusion times (t_{difmax}) in Table 4.2 have the same order of magnitude as the time constants (τ). Note that the time constant of mono-exponential HDO-uptake curves equals the time at which the amount of tracer corresponds to 63 % of the final amount in the steady state. For example, blood filter 2 had an time constant of 26 s, which indeed corresponds to the time at which the amount of tracer is 63 % of the amount in the steady state, see Figure 4.6B. The amount of tracer reached a steady state approximately 100 s after injection, which corresponds roughly to the estimated t_{difmax} in Table 4.2.

Table 4.2 Comparison of estimated maximum HDO diffusion times (t_{difmax}) with time constants of mono-exponential HDO-uptake curves (τ) of different unmodified blood filters, see in vivo experiments. The temperature was 20° C during the experiments, thus the HDO diffusion coefficient is approximately 2.10^{-5} $cm^2.s^{-1}$ (27,28). The system flow velocity is 2.46 ml.s^{-1}.

blood filter	micd$_{max}$ ± SE (μm)	t_{difmax} (s)	τ ± SE (s)
1	1500 ± 465	70	21 ± 1.1
2[a]	1620 ± 818	82	26 ± 2.6
3	1735 ± 595	94	36 ± 2.5
4	1900 ± 760	113	53 ± 4.2

a) see Figure 4.6A and 4.6B.

Effect of modifications of the capillary distribution in blood filters on HDO-uptake curves and comparison with simulations of the 2D diffusion.

In Figure 4.6A and 4.6C an example is shown of the anisotropic capillary distribution in an unmodified (Figure 4.6A) and a modified blood filter (Figure 4.6C) with the corresponding HDO-uptake curves displayed in Figures 4.6B & 4.6D, respectively. The linear flow velocity in the modified filter was increased by approximately a factor two due to the blocking of one half of the capillaries. This had no effect on the HDO-uptake curve, as expected from a diffusion-limited model. The HDO-uptake rate in the modified blood filter (Figure 4.6D) was even slower than the HDO-uptake rate in the unmodified filter (Figure 4.6D). In the modified filter the number of small diffusion distances decreases and the number of large diffusion distances increases. Upon the introduction of large diffusion distances in modified filters, the HDO-uptake curves became multi-exponential, see Figure 4.6D. The curves derived from 2D diffusion simulations (solid lines in Figure 4.6B and 4.6D) correspond well to the HDO-uptake curves in all blood filters. However, diffusion simulations gave a faster HDO uptake at the beginning of the curve for all filters.
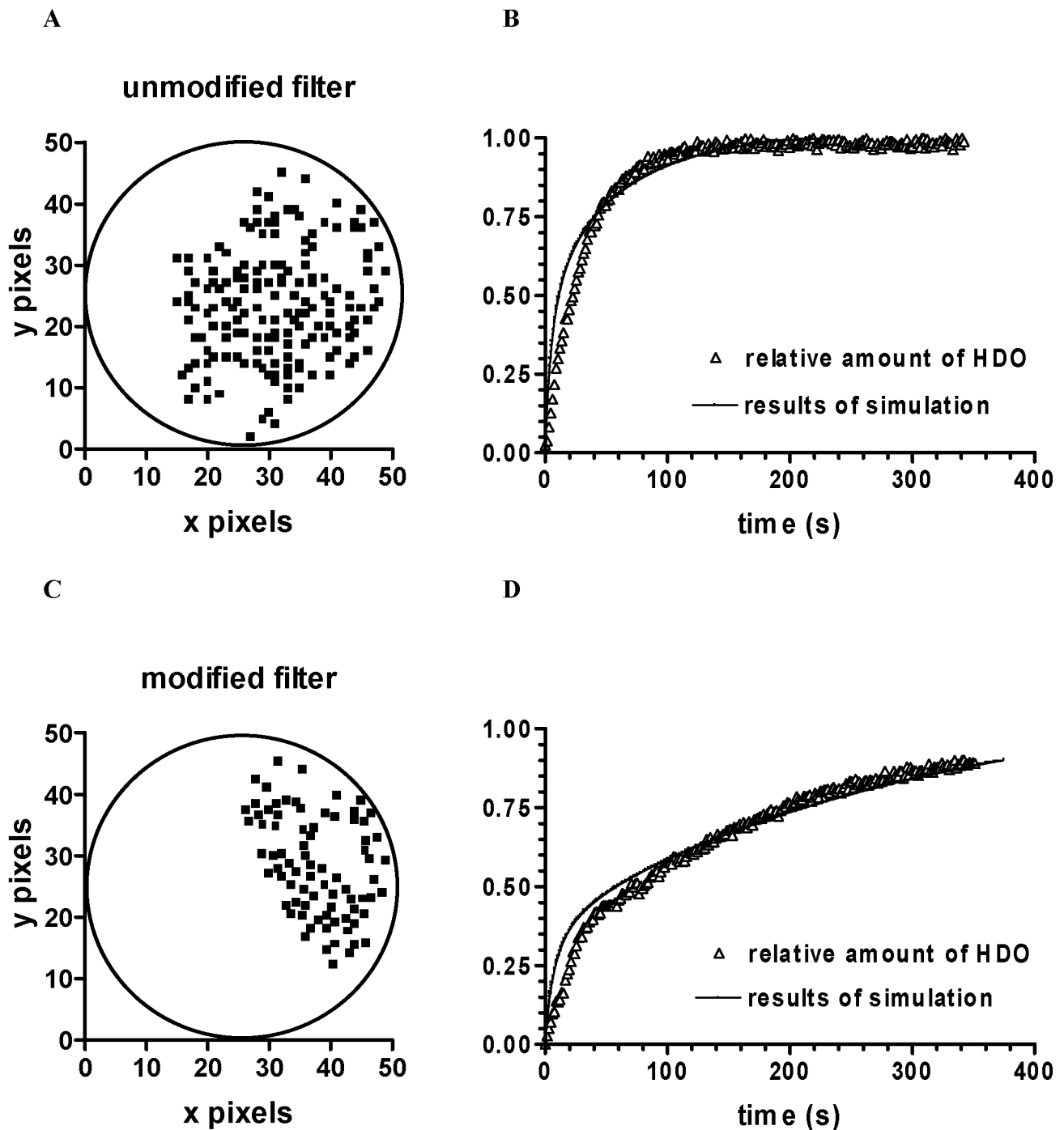
A

unmodified filter

B

C

modified filter

D

Figure 4.6 Examples of HDO-uptake experiments with an unmodified (Figure 4.6A) and a modified blood filter (Figure 4.6C). The effect of capillary distribution on the HDO uptake is shown in Figure 4.6B and 4.6D. 2D simulations of diffusion (—) correspond well to the HDO-uptake curves (Δ), see text. The temperature was $20°$ C during the experiments, and the system flow velocity was 2.46 ml.s^{-1} in both cases.

Discussion

To our knowledge this is the first study that relates HDO-uptake in tumors to morphometric analyses of the perfused vascular architecture. An (immuno)histochemical method was used to analyse the 2D distribution of perfused capillaries in whole tumor sections. A main question in this matter is whether this method, immediately applied after the MR-experiments, detects all functional capillaries during the HDO-uptake experiments or underestimates the number of perfused capillaries due to subpopulations of capillaries with very slow and irregularly perfusion rates? In the latter case, intercapillary distances between perfused capillaries would have been overestimated as well as HDO diffusion times. However, in complementary studies in which the 2D distribution of perfused capillaries and hypoxic cells were analyzed simultaneously (30, 31), evidence is provided that the histochemical method virtually detects all functional capillaries. These analyses showed that a continuous rim of hypoxic cells occurred at a certain distance from perfused regions, which indicated that these cells are chronically hypoxic (diffusion-limited O_2 supply). Capillaries which transiently open and close in such a way that hypoxic region appear acutely were not observed. In such a case, the Hoechst signal would show overlap with hypoxic cells and/or isolated areas of nonhypoxic cells would occur in hypoxic regions around capillaries, which were not perfused with Hoechst. In addition, the 2D distribution of perfused capillaries in complete tumor sections was found to match to the 2D distribution of the contrast agent Gd_DTPA in comparable slices (30, 31). Gd_DTPA accumulates in tumor regions adjacent to perfused capillaries. Thus, it seems safe to assume that the histochemical method virtually detects all functional capillaries.

In the present study, heterogeneously and homogeneously perfused human glioma xenografts were used to analyse in more detail the relationship between maximum HDO diffusion times and time constants of HDO-uptake curves. As long as there is no histological or physiological evidence for the existence of multiple tumor tissue compartments in the volume of interest, which are more or less accessible to HDO, one has to consider maximum diffusion distances for an estimation of maximum diffusion times.

In vivo studies

The tumors of both lines showed a rather homogeneous water apparent diffusion coefficient (ADC_w) map. The range of ADC_w values and the average ADC_w of both lines is in good agreement with ADC_w values found by others in different tumor models (32-34). Histological features might limit the HDO diffusion in the extravascular space of the tumor. However, histological analyses of eosin and haematoxylin stained tumor sections did not reveal any histological barrier in human glioma xenografts, which may limit the diffusion of HDO.

In addition, the interstitial fluid pressure might also affect the free diffusion of HDO (35). However, Dvorak et al (36) showed that small fluorescent molecules can enter tumor tissue freely and are not selectively excluded from any region in small tumors ($\varnothing < 1$ cm, weight $< \sim 1$ g). In a preliminary study we found that small bioreductive chemical probes such as N-imidazole-theophylline and pimonidazole distribute homogeneously in our tumor model within 80 min after injection (= approximately the total time of HDO-uptake measurements) (30, 31). Thus, a possible restriction of HDO diffusion in the extravascular space due to interstitial fluid pressure is not expected.

The average ADC_w and mean maximum icds were used for estimations of the maximum HDO-diffusion time per tumor. A linear correlation was found between t_{difmax} and (weighted mean) time constants of mono-exponential or bi-exponential HDO-uptake curves. Mono-exponential HDO-uptake curves were mainly found in tumors with a homogeneously perfused capillary distribution.

Tumors with a heterogeneously perfused capillary distribution showed a multi-exponential HDO uptake. The latter could not be explained by changes of the HDO concentration in the blood compartment, because 1 min after bolus injection the HDO concentration remained constant during the total experiment time. Maximum HDO-diffusion times and time constants were obtained from two independent series of experiments. The linear correlation between t_{difmax} and time constants as well as the observed differences of HDO-uptake in homogeneously and heterogeneously perfused human glioma xenografts indicate that the time constants are related to the perfused capillary distribution and to diffusion processes in the tumor. However, we cannot completely exclude that spatial and temporal variability in perfusion rates contribute to the uptake curves, because perfusion rates were not measured directly in capillaries. The following arguments provide some further support for the notion that diffusion processes play a significant role in the uptake kinetics of HDO in our glioma xenografts.

Until now, no methods are available to measure perfusion rates in individual capillaries noninvasively, with the exception of microscopic analyses of red blood cells velocities (37). The latter study can be used to gain a rough appreciation of mean capillary transit time of HDO molecules in perfused capillaries, if one assume that the linear velocity of HDO molecules in perfused capillaries is supposed to be determined by the linear velocity of red blood cells. These velocities of red blood cells were found to vary between 0.08 to 0.4 $mm.s^{-1}$ in capillaries of human glioma xenografts (37). Capillary path lengths in tissue-isolated mammary carcinoma measured from the entrance of the capillary mesh to the exit ranged from 0.5 to 1.5 mm (15). Thus, red blood cells with a linear velocity varying between 0.08 and 0.3 $mm.s^{-1}$ have a mean capillary transit time of approximately 5 s for a capillary path length of approximately 1 mm, which is similar to the mean capillary transit time of HDO molecules as estimated by Eskey et al (8). In the case of perfusion-limited tracer-uptake this mean capillary transit time must be longer than HDO-diffusion times. This will occur in perfused tumor regions with short icds, a situation that can be encountered both in regional and global HDO-uptake measurements.

For regional HDO-uptake experiments Eskey et al (8) approximated HDO-diffusion times in perfused regions of tissue-isolated mammary adenocarcinoma using a modified Einstein diffusion equation (comparable to Eq. [3]). The mean distance between perfused capillaries in their tumor model was approximately 50 µm (15). For the determination of their mean intercapillary distance, Less et al (15) used a polymer infusion technique and icds were measured in well-perfused regions only. The icds in perfused regions of our tumor model were similar to icds found by Less et al (15). Eskey et al (8) assumed an HDO diffusion coefficient (D_{HDO}) of 1.10^{-5} $cm^2.s^{-1}$ in tumor tissue (comparable to the average ADC_w in this study). Thus, the HDO-diffusion time was approximately 0.5 s, which, indeed, is much shorter than the estimated mean capillary transit time of 5 s.

In global HDO-uptake measurements the HDO-uptake may become perfusion-limited in homogeneously perfused tumors with short icds. Studies of the two-dimensional perfused capillary distribution in complete sections of RIF-1 tumors and GH3 prolactinomas (a generous gift from Dr. Paul McSheehy, CRC Biomedical Magn. Reson. Research Group, St.George's Hospital Medical School, London) show that these tumors have a homogeneous perfused vascular architecture with short icds. The mean intercapillary distance of both tumors is 51 ± 7 µm, and the mean maximum intercapillary distance is 338 ± 43 µm which is much shorter than those determined for human glioma xenografts in this study. These tumors may have a perfusion-limited HDO-uptake, because the estimated maximum diffusion time of HDO molecules in the total tumor volume is approximately 8.5 s, which is comparable to the estimated mean capillary transit time of HDO molecules.

Human glioma xenografts in this study showed an asymmetrical frequency histogram of icds with a significant tail for long distances (see 25 and Fig. 6.2). The estimated mean capillary transit time of HDO molecules is much shorter than the maximum HDO-diffusion times and time constants of HDO uptake in the whole tumor volume, which indicate that global HDO-uptake rates are merely related to the distribution of perfused capillaries. Thus, diffusion-limited HDO-uptake may be related to diffusion-limited delivery of oxygen and nutrients. Indeed this was corroborated by ^{31}P-MR spectroscopy studies on exactly the same tumors (ref. 25 and chapter 6). In this study a decrease of the bioenergetic status of the whole tumor was found to be linearly related to an increase of the percentage of intercapillary distances larger than 200 μm.

Model studies

The aim of the model studies was to show that in the case of diffusion-limited HDO-uptake, the latter is related to the distribution of perfused capillaries as deduced from the comparison of HDO-uptake curves with 2D diffusion simulations.

Diffusion simulations showed a somewhat faster HDO-uptake rate at the beginning of the curve in all filters. Discrepancies between HDO-uptake experiments and simulations may have the following causes: a) In simulations, the HDO diffusion from perfused capillaries was supposed to be isotropic, but the thickness and porous structure of capillary membranes may influence freely tracer diffusion. b) In 2D diffusion simulation the 2D capillary distribution at the filter inlet was used, whereas ^{2}H-MRS measurements were performed halfway through the filter. Small variations in icds and capillary distributions between both sites may explain the discrepancy. Discrepancies cannot be explained by perfusion-limited uptake in the first part of HDO-uptake curves. In that case the HDO-uptake rate would have been faster in modified filters in comparison with unmodified filters, because the linear flow velocity of HDO molecules in perfused capillaries of modified filters was two times larger than the linear flow velocity in the capillaries of unmodified filters.

Although blood filters are not exactly comparable to human glioma xenografts, the multi-exponential HDO-uptake curves were related to heterogeneous capillary distributions in both experiments. Simulations of the 3D diffusion of HDO in tumors was not possible, because information of the 3D perfused vascular architecture was not available. In in vivo studies, estimations of HDO diffusion times were obtained using a 2D dataset of intercapillary distances. The linear correlation between maximum HDO diffusion times and time constants of HDO-uptake curves suggest that diffusion processes cannot be neglected during global HDO-uptake studies in human glioma xenografts. Values of maximum diffusion times and time constants would not have been comparable when the HDO-uptake rates were purely limited by perfusion.

Conclusions. In human glioma xenografts a significant fraction of relatively large intercapillary distances was found. For the interpretation of global HDO-uptake curves as monitored with ^{2}H-MRS, diffusion of HDO in the extravascular volume of these tumors have to be taken into account. Therefore, tracer-uptake studies at high spatial and temporal resolution (see ref. 31 and 38 or chapter 3) may give a better estimate of tumor blood perfusion than time-resolved HDO-uptake experiments of the whole tumor; especially if tracer-uptake rates are only measured in perfused tumor regions with a high perfused capillary density and short intercapillary distances.

Appendix

When the diffusion coefficient (D) is independent of time (t) and location (x), Fick's law for one dimension can be written as:

$$\frac{\partial u(x,t)}{\partial t} = D \cdot \frac{\partial^2 u(x,t)}{\partial x^2} \qquad [A1]$$

In Eq. [A1], u(x,t) represents the HDO concentration at location (x) and at time (t). The numerical solution of Eq. [A1] in one dimension (Crank-Nicholson scheme) using a forward time-centred space scheme (FTCS) (29) is:

$$\frac{u_j^{n+1} - u_j^n}{\Delta t} = \frac{D}{2} \left[\frac{(u_{j+1}^{n+1} - 2 \cdot u_j^{n+1} + u_{j-1}^{n+1}) + (u_{j+1}^n - 2 \cdot u_j^n + u_{j-1}^n)}{\Delta x^2} \right] \qquad [A2]$$

In Eq. [A2], time is indicated by the superscript n and location by the subscript j. Rewriting Eq. [A2] with the same time terms on both sides and defining the constant γ as: $\gamma = \{D.\Delta t\} / \{2.\Delta x^2\}$ with Δt as the time step and Δx as the distance step, we get:

$$u_j^{n+1} - \gamma \cdot [u_{j+1}^{n+1} - 2 \cdot u_j^{n+1} + u_{j-1}^{n+1}] = u_j^n + \gamma \cdot [u_{j+1}^n - 2 \cdot u_j^n + u_{j-1}^n] \qquad [A3]$$

For a stable iteration scheme the constant γ has to be smaller than ¼. Eq. [A3] can be rewritten in matrix form, see e.g. term in brackets at time n + 1:

$$u_{j+1}^{n+1} - 2 \cdot u_j^{n+1} + u_{j-1}^{n+1} = \begin{bmatrix} -2 & 1 & 0 & 0 & .. \\ 1 & -2 & 1 & 0 & .. \\ 0 & 1 & -2 & 1 & .. \\ .. & .. & .. & .. & .. \end{bmatrix} \cdot \begin{bmatrix} u_0^{n+1} \\ u_1^{n+1} \\ .. \\ u_k^{n+1} \end{bmatrix} = A \cdot U^{n+1} \qquad [A4]$$

The vector U^{n+1} in Eq. [A4] correponds to the distribution of the HDO concentration in one dimension at time n+1. In 2 dimensions, this vector U becomes a matrix U (see Eq. [A8] and [A9]). In 2D HDO-diffusion simulations the matrix U at time = 0 contains the perfused capillary distribution, as shown, e.g., in Figure 4.6A and 4.6C. At time = 0 the distribution of the HDO concentration correponds to the perfused capillary distribution and is maximum in these capillaries. At every time step (n+1) a new matrix (U^{n+1}) is calculated showing the changes of the HDO concentration distribution around perfused capillaries due to radial diffusion. The HDO concentration in the capillaries is reset to the maximum values at every time step, corresponding to a constant supply of HDO. In general, Eq. [A3] in matrix form becomes Eq. [A5]:

$$(1 - \gamma A) \cdot U^{n+1} = (1 + \gamma A) \cdot U^n \qquad [A5]$$

For j = 0 the diffusion outside the blood filter (j = -1) cannot take place, so boundary conditions have to be introduced. The concentration gradient between location j = -1 and j = 1 is set to zero; this means that: $u_{-1} = u_1$. Using Eq. [A4] for j = 0 gives $u_{-1} - 2.u_0 + u_1$; with $u_{-1} = u_1$ we obtain $2.u_1 - 2.u_0$. The matrix A becomes, Eq. [A6]:

$$A = \begin{bmatrix} -2 & (2) & 0 & 0 & .. \\ 1 & -2 & 1 & 0 & .. \\ .. & .. & .. & .. & .. \\ .. & 0 & 1 & -2 & 1 \\ .. & 0 & 1 & (2) & -2 \end{bmatrix}$$

[A6]

In 2 dimensions Eq. [A1] is transformed as follows:

$$\frac{\partial u(x,y,t)}{\partial t} = D\left[\frac{\partial^2 u(x,y,t)}{\partial x^2} + \frac{\partial^2 u(x,y,t)}{\partial y^2}\right]$$

[A7]

The Crank-Nicholson algorithm is changed using the alternating-direction implicit method (ADI). This method divides each time step into two steps of duration $\Delta t/2$. In the first $\Delta t/2$ step the diffusion in the x-direction is calculated under the influence of concentration gradients in the y-direction and vice versa. Following Eq. [A5] in matrix form we obtain:

$$(1 - 2\gamma A).U^{n+\frac{1}{2}} = (1 + 2\gamma A).(U^n)^T$$

[A8]

$$(1 - 2\gamma A).(U^{n+1})^T = (1 + 2\gamma A).U^{n+\frac{1}{2}}$$

[A9]

In Eq. [A8] and [A9] transposed matrices are used for changing the multiplication with matrix A from x- to y-direction. In Eq. [A8] the result of diffusion in the x-direction ($U^{n+\frac{1}{2}}$) after time step $\Delta t/2$ under influence of the y-direction $(U^n)^T$ is calculated. The matrix U^n is known. Next, in Eq. [A9] the result of diffusion in the y-direction $(U^{n+1})^T$ after time step $\Delta t/2$ under influence of the x-direction ($U^{n+\frac{1}{2}}$) is calculated.

References

1. Kim SG, Ackerman JJH. Quantitative Determination of Tumor Blood Flow and Perfusion via Deuterium Nuclear Magnetic Resonance Spectroscopy in Mice. *Cancer Res* **48**: 3449-3453 (1988).

2. Kim SG, Ackerman JJH. Quantification of Regional Blood Flow by Monitoring of Exogenous Tracer via Nuclear Magnetic Resonance Spectroscopy. *Mag Reson Med* **14**: 266-282 (1990).

3. Larcombe McDouall JB, Evelhoch JL. Deuterium Nuclear Magnetic Resonance Imaging of Tracer Distribution in D_2O Clearance Measurements of Tumor Blood Flow in Mice. *Cancer Res* **50**: 363-369 (1990).

4. Mattiello J, Evelhoch JL. Relative Volume-Average Murine Tumor Blood Flow Measurement via Deuterium Nuclear Magnetic Resonance Spectroscopy. *Mag Reson Med* **18**: 320-334 (1991).

5. Evelhoch JL, Larcombe McDouall JB, Mattiello J, Simpson NE. Measurement of Relative Regional Tumor Blood Flow in Mice by Deuterium NMR Imaging. *Mag Reson Med* **24**: 42-52 (1992).

6. Evelhoch JL. Measurements of Tumor Blood Flow by Deuterium NMR and the Effects of Modifiers. *NMR in Biom* **5**: 290-295 (1992).

7. Smits GAHJ, Cornel EB, van de Boogert E, Oosterhof GON, Debruyne FMJ, Schalken JA, Heerschap A. Effects of High Energy Shock Waves on Tumor Blood Flow and Metabolism: $^{31}P/^{1}H/^{2}H$ Nuclear Magnetic Resonance Study. *NMR in Biom* **7**: 319-326 (1994).

8. Eskey CJ, Koretsky AP, Domach MM, Jain RK. ^2H-Nuclear Magnetic Resonance Imaging of Tumor Blood Flow: Spatial and Temporal Heterogeneity in a Tissue-isolated Mammary Adenocarcinoma. *Cancer Res* **52**: 6010-6019 (1992).

9. Kety SS. The Theory and Applications of The Exchange of Inert Gas at the Lungs and Tissues. *Pharmacol Rev* **3**: 1-41 (1951).

10. Neil JJ. The validation of Freely Diffusible Tracer Methods with NMR Detection for Measurement of Blood Flow. *Mag Reson Med* **19**: 299-304 (1991).

11. Evelhoch JL. Tracer Measurements of Blood Flow, in " NMR in Physiology and Biomedicine" (R.J. Gillies, Ed.), pp. 209-220, Academic Press, San Diego, 1994.

12. Tofts PS, Kermode AG. Measurements of the Blood-Brain Barrier Permeability and Leakage Space using Dynamic MR Imaging. 1. Fundamental Concepts. *Mag Reson Med* **17**: 357-367 (1991).

13. Larsson HBW, Stubgaard M, Frederiksen JL, Jensen M, Henriksen O, Paulson OB. Quantitation of Blood-Brain Barrier Defect by Magnetic Resonance Imaging and Gadolinium-DTPA in Patients with Multiple Sclerosis and Brain Tumors. *Mag Reson Med* **16**: 117-131 (1990).

14. Kovar DA, Lewis MZ, River JN, Lipton MJ, Karczmar GS. In Vivo Imaging of Extraction Fraction of Low Molecular Weight MR Contrast Agents and Perfusion Rate in Rodent Tumors. *Mag Reson Med* **38**: 259-268 (1997).

15. Less JR, Skalak TC, Sevick EM, Jain RK. Micovascular Architecture in a Mammary Carcinoma: Branching Patterns and Vessel Dimensions. *Cancer Res* **51**: 265-273 (1991).

16. Altman PL, Dittmer DS. in "Respiration and Circulation, Biological Handbooks, Federation of American Societies for Experimental Biology" (Altman PL, Dittmer DS, Eds.), p. 453-455, Bethesda, Maryland, 1974.

17. Jain RK. Transport of Molecules in the Tumor Interstitium: A Review. *Cancer Res* **47**: 3039-3051 (1987).

18. LeBihan D, Turner R. Diffusion and Perfusion, in "Magnetic Resonance Imaging (2nd ed.)", (D.D. Stark, W.G. Bradley, A.S. Patterson, Eds.), 1, p. 355 - 353, Mosbey-Year Book, St. Louis, Missouri, 1992.

19. Rijken PFJW, Bernsen HJJA, van der Kogel AJ. Application of an Image Analyses System to the Quantitation of Tumor Perfusion and Vascularity in Human Glioma Xenografts. *Microvascular Res* **50**: 141-153 (1995).

20. Bernsen HJJA, Rijken PFJW, Oostendorp T, van der Kogel AJ. Vascularity and perfusion of human gliomas xenografted in the athymic nude mouse. *Br J Cancer* **71(4)**: 721-726 (1995).

21. Conolly S, Glover G, Nishimura D, Macovski A. A Reduced Power Selective Adiabatic Spin-Echo Pulse Sequence. *Mag Reson Med* **18**: 28-38 (1991).

22. Garwood M, Ke Y. Symmetric Pulses to Induce Arbitrary Flip Angles with Compensation for RF Inhomogeneity and Resonance Offsets. *Journal of Mag Reson* **94**: 511-525 (1991).

23. Silver MS, Joseph RI, Hoult DI. Highly Selective $\pi/2$ and π Pulse Generation. *Journal of Mag Reson* **59**: 347-351 (1984).

24. Yoshii Y, Sugiyama K. Intercapillary Distance in the Proliferating Area of Human Glioma. *Cancer Res* **48**: 2938-2941 (1988)

25. van der Sanden BPJ, Rijken PFJW, Heerschap A, Bernsen HJJA, van der Kogel AJ. In vivo ^{31}P-Magnetic Resonance Spectroscopy and Morphometrical Analyses of the Perfused Vascular Architecture of Human Glioma Xenografts in Nude Mice, *Br J Cancer*, **75(10)**: 88-97 (1997).

26. Vaupel PW. Blood Flow, Oxygenation, Tissue pH Distribution, and Bioenergetic Status of Tumors, in "Ernst Schering Research Foundation 23", p. 19, Information and Standards Medical Scientific Publications Design, Berlin, 1994.

27. Sehgal CM, Greenleaf JF. Correlative Study of Properties of Water in Biological Systems Using Ultrasound and Magnetic Resonance, *Mag Reson Med* **3**: 976-985 (1986).

28. LeBihan D, Turner R. Diffusion and Perfusion, in "Magnetic Resonance Imaging (2nd ed.)", (Stark DD, Bradley WG, Patterson AS, Eds.), 1, p. 344, Mosbey-Year Book, St. Louis, Missouri, 1992.

29. Press WH, Flannery BP, Teukolsky SA, Vetterling WT. Numerical Recipes in C, The Art of Scientific Computing, p. 656-665, Cambridge University Press, 1988.

30. van der Sanden BPJ, de Graaf RA, Rijken PFJW, Peters JPW, Heerschap A, Nicolay K, van der Kogel AJ. A Comparative Study of Dynamic ^{1}H-MRI studies of Gd_DTPA Uptake, Perfused Vessel Distribution and Hypoxic Areas in Human Glioma Xenografts in "Proc., ISMRM, 5th Annual Meeting, Vancouver, 1997", p. 1087.

31. van der Sanden BPJ, Rozijn T, Rijken P, Peters H, Heerschap A, van der Kogel A, Bovée W. Gd_DTPA-uptake rates are linearly related to the perfused capillary surface-area in 9L Gliomas rat models. "15th Annual ESMRMB Meeting,Geneva, 1998", MAGMA 6 suppl. (1), p. 58.

32. Maier CF, Paran Y, Grobgeld D, Bendel P, Rutt BK, Degani H. Quantitative Diffusion Imaging in Implanted Human Breast Tumors. *Mag Reson Med* **37**: 576-581 (1997).

33. Zhao M, Pipe JG, Bonnett J, Evelhoch JL. Early Detection of Response to Cyclophosphamide Chemotherapy by Diffusion-Weighted ^{1}H NMR Spectroscopy in Murine RIF-1 Tumors in vivo, "in Proc., ISMRM, 3th Annual meeting, Nice, 1995", p.63.

34. Wang Z, Su M-Y, Lao X, Nalcioglu O. A Quantitative Analyses for Blood Volume Mapping Using Diffusion Weighted MRI : Application in Tumors, "in Proc., ISMRM, 4th Annual meeting, New York, 1996", p.265.

35. Boucher Y, Baxter LT, Jain RK. Interstitial Pressure Gradients in Tissue-isolatedand Subcutaneous Tumors: Implications for Therapy. *Cancer Res* **50**: 4478-4484 (1990).

36. Dvorak HF, Nagy JA, Dvorak JT, Dvorak AM. Identification and Characterization of the Blood Vessels of Solid Tumors That Are Leaky to Circulating Macromolecules. *AM J Pathology* **133 (1)**: 95-109 (1988).

37. Yuan F, Salehi HA, Boucher Y, Vasthare US, R.F. Tuma RF, Jain RK. Vascular Permeability and Microcirculation of Gliomas and Mammary Carcinomas Transplanted in Rat and Mouse Cranial Windows. *Cancer Res* **54**: 4564-4568 (1994).

38. Su M-Y, Wang Z, Roth GM, Lao X, Samoszuk MK, Nalcioglu O. Pharmacokinetic Changes Induced by Vasomodulators in Kidneys, Livers, Muscles, and Implanted Tumors in Rats as Measured by Gd_DTPA-Enhanced MRI. *Mag Reson Med* **36**: 868-877 (1996).

Chapter 5

Characterization and validation of noninvasive oxygen tension measurements in human glioma xenografts by ^{19}F-MR relaxometry

Boudewijn P.J. van der Sanden
Arend Heerschap
Arjan W. Simonetti
Paul F.J.W. Rijken
Hans P.W. Peters
Georg Stüben
Albert J. van der Kogel

Abstract

Purpose: The aim of this study was to characterize and to validate noninvasive ^{19}F-magnetic resonance relaxometry for the measurement of oxygen tensions in human glioma xenografts in nude mice. The following three questions were addressed: 1. When perfluorocarbon compounds (PFCs) are administrated intravenously, which tumor regions are assessed by ^{19}F-MR relaxometry? 2. Are oxygen tensions as detected by ^{19}F-MR relaxometry ($pO_{2/relaxo}$) comparable to Eppendorf O_2-electrode measurements ($pO_{2/electrode}$)? 3. Can ^{19}F-MR relaxometry be used to detect oxygen tension changes in tumor tissue during carbogen breathing?

Methods and Materials: Slice-selective ^{19}F-MR relaxometry was carried out with perfluoro-15-crown-5-ether as oxygen sensor. The PFC was injected i.v. 3 days before the ^{19}F-MR experiments. Two data sets were acquired before and two after the start of carbogen breathing. The distribution of PFCs and necrotic areas were analyzed in ^{19}F-Spin Echo (SE) density MR-images and T_2-weighted ^{1}H-SE MR-images, respectively. One day after the MR-investigations oxygen tensions were measured by oxygen electrodes in the same slice along two perpendicular tracks. These measurements were followed by (immuno)histochemical analyses of the 2D distribution of perfused microvessels, hypoxic cells, necrotic areas and macrophages.

Results: The PFCs mainly became sequestered in perfused regions at the tumor periphery; thus, ^{19}F-MR relaxometry probed mean oxygen tensions in these regions throughout the selected MR-slice. In perfused regions of the tumor, mean $pO_{2/relaxo}$ values were comparable to mean $pO_{2/electrode}$ values and varied from 0.03 to 9 mmHg. Median $pO_{2/electrode}$ values of both tracks were lower than mean $pO_{2/relaxo}$ values, because low $pO_{2/electrode}$ values that originate from hypoxic and necrotic areas were also included in calculations of median $pO_{2/electrode}$ values. After 8-min carbogen breathing the average $pO_{2/relaxo}$ increase was 3.3 ± 0.8 (SEM) mmHg and 2.1 ± 0.6 (SEM) after 14 min breathing.

Conclusions: We have demonstrated that PFCs mainly became sequestered in perfused regions of the tumor. Here, mean $pO_{2/relaxo}$ values were comparable to mean $pO_{2/electrode}$ values. In these areas, carbogen breathing was found to increase the $pO_{2/relaxo}$ values significantly.

Introduction

It has been shown that the oxygen tension of tumor tissue is an important physiological parameter during radiotherapy treatment (1-3). Hypoxic tumor cells are approximately three times more radioresistant than well-oxygenated cells (1). Therefore, modulations of the oxygen tension in tumor tissue may enhance the sensitivity of tumor cells for radiotherapy. For example, breathing of carbogen (95 % O_2, 5 % CO_2) has been introduced to decrease the fraction of chronically hypoxic cells (4-6). The combination of carbogen breathing with the administration of nicotinamide has produced a significant increase in local control of advanced laryngeal tumors (7).

A method to assess local or global oxygen tensions in tumor tissue would be valuable and may be used to predict the outcome of a treatment modality. Polarography (Eppendorf O_2-electrodes) is the most frequently used technique for direct measurements of local or global oxygen tensions in tumor tissue ($pO_{2/electrode}$) (8, 9). Although oxygen electrodes are small, polarographic measurements are invasive and studies of deep tumors are difficult or even impossible without surgery.

^{19}F-magnetic resonance relaxometry (^{19}F-MR relaxometry) using perfluorocarbon (PFC) compounds is a noninvasive technique, which permits the determination of local or global oxygen tensions in tumors ($pO_{2/relaxo}$) independent of the location of the tumor (10-17). This technique is based on the linear relationship between the spin-lattice relaxation rates ($1/T_1$) of ^{19}F-spins in PFCs and the local oxygen tension in tumor tissue. In most ^{19}F-MR relaxometry studies PFCs are administered intravenously a few days before the MR-measurements (11-15). After approximately 3 days PFCs had accumulated in tumor tissue and in the reticulo-endothelial system of liver and spleen, and PFCs were not detectable in blood plasma (11, 15, 18).

Before ^{19}F-MR relaxometry can be used as an indicator of absolute oxygen tensions or oxygen tension changes in tumor tissue, it will need extensive comparison with more established techniques such as polarography. A proper comparison between both techniques is possible when the distribution of PFC compounds is spatially correlated to the approximate location of the O_2-electrodes. In addition, it is necessary to know how the distribution of the PFCs and the location of the O_2-electrode tracks are spatially correlated to the distribution of perfused, hypoxic and necrotic tumor areas. The extent of the latter areas determine local or global oxygen tensions in tumors, and can be used to explain possible differences of pO_2 values as probed by both methods. Furthermore, validation of $pO_{2/relaxo}$ values with $pO_{2/electrode}$ values is of interest, because $pO_{2/relaxo}$ values are derived from T_1-relaxation rates of ^{19}F-spins in perfluorocarbon compounds and in principle these relaxation rates may also depend on other physiological and histological parameters.

The aim of this paper is to characterize and to validate in vivo ^{19}F-MR relaxometry as a tool to measure oxygen tensions and changes in oxygen tensions noninvasively in human glioma xenografts. The following questions were addressed: When perfluorocarbon compounds (PFCs) are administrated intravenously, which tumor regions are assessed by ^{19}F-MR relaxometry? How are the $pO_{2/relaxo}$ values related to $pO_{2/electrode}$ values? Finally, can ^{19}F-MR relaxometry be used to detect oxygen tension changes in tumor tissue during carbogen breathing?

To answer these questions the 2D distribution of perfluorocarbon compounds in ^{19}F-MR-images was compared to the 2D distribution of perfused microvessels, hypoxic regions,

macrophages (18) and necrotic areas using histochemical analyses (19) and T_2-weighted ^{1}H-MR images, respectively. In a previous study (18), it had been suggested that PFCs are taken up by macrophages, and therefore the distribution of the latter was also compared to the PFC distribution. For each tumor, both $pO_{2/relaxo}$ and $pO_{2/electrode}$ values were sampled in comparable slices through the center of tumors and oxygen tensions changes were measured during carbogen breathing.

Materials and Methods

Animal model. Human glioma xenografts (line E49) were grown subcutaneously in the hindlimbs of 13 athymic mice (Balb/c nu/nu, BonholdGard, Ry, Denmark) (20). In pilot studies on the feasibility of slice-selective ^{19}F-MR relaxometry measurements of oxygen tensions in 2 homogeneously perfused human glioma xenograft lines (E98, E106) (20)) and a heterogeneously perfused line (E49), the PFC uptake was only sufficient for slice-selective ^{19}F-MR relaxometry measurements in tumor line E49. Tumor volumes (cm^3) of the latter line were estimated from the formula: $(\pi / 6)$ x abc, where a, b and c are orthogonal diameters as measured with calipers. Mice were anaesthetized with 2 % enflurane in an oxygen-nitrous (25 % O$_2$) gas mixture applied through a nose cone. For experiments with carbogen breathing the oxygen-nitrous gas mixture was switched to carbogen (95% O$_2$/5% CO$_2$) and the percentage of enflurane was kept constant. The flow velocity was 1 l.min^{-1} in all experiments and the composition of gas mixtures was analyzed on-line at the inlet of the nose cone with a gas monitor (Datascope Multinex, Datascope Corp. Paramus, NJ, USA). All experiments were started 5 minutes after the beginning of carbogen breathing. The 5-min pre-breathing time was based on results of near-infrared spectroscopy experiments, which showed that after 5 min the oxyhemoglobin concentration was close to a steady state (21). Body temperature was monitored with a rectal probe (36-gauge wire, Hewlett Packard) and maintained at 36.5° - 37° C by a warm water blanket with a feedback system. The anesthesia and temperature controls were similar for the in vivo ^{19}F-MR relaxometry studies and the polarography measurements (see next sections); thus, possible effects of e.g. anesthesia on the results of both experiments were comparable. The local ethical committee for animal use approved the experimental procedures.

^{19}F-MR relaxometry. ^{19}F-MR relaxometry measurements were performed on an SMIS spectrometer interfaced to a vertical bore magnet (4.3 T) employing a home-built ^{1}H/^{19}F double tunable solenoid ($\varnothing$ 13 mm).

In vitro experiments. An in vitro calibration curve ($1/T_1$ (s^{-1}) versus pO$_2$ (mmHg)) was generated using an inversion-recovery T_1-sequence with a 180° adiabatic full passage inversion pulse (22) and a 90° hard excitation pulse. The PFC emulsion (40% (v/v) perfluoro-15-crown-5-ether, HemaGen/PFC, St. Louis, MO, USA) was bubbled for 60 minutes with 5 different gas mixtures (O$_2$/N$_2$) containing 0 %, 10 %, 21 %, 48 % and 100 % O$_2$. During the T_1 measurements gas mixtures were led smoothly over the emulsion to maintain pO$_2$ levels. The temperature of the emulsion was monitored online and was kept at 37° C using the same feedback system and rectal probe as mentioned in the previous paragraph. For low pO$_2$ values the T_1-relaxation time of ^{19}F-spins is relatively long; thus, a different array of delay times between inversion and excitation pulse was used for correct measurements of the different T_1-relaxation times. For the gas mixtures containing 0 % and 10 % O$_2$, the 8 delay times of inversion (TIs) varied between 0.2 and 6 s, and for the other gas mixtures the TIs ranged from 0.2 to 3 s. The in vitro calibration curve was determined from 3 independent measurements.

In vivo experiments. Three days before the NMR experiments 0.15 ml of the 40% (v/v) PFC emulsion was injected via a tail vein (dose: 4.2 g/kg). For the appropriate positioning of a coronal slice for ^{19}F MR relaxometry studies through the center of the tumor parallel to the solenoid coil, multi-slice coronal T$_2$-weighted ^{1}H-spin echo images (SE images) were acquired (TR=1 s, TE=0.06 s, number of scans = 2, matrix size = 128 x 128, FOV 15 x 15 mm, slice thickness 1.5 mm). Simultaneously, these T$_2$-weighted ^{1}H-SE images were used for analyses of the necrotic area distribution in comparable slices as observed in

in vivo ^{19}F-MR experiments. The water diffusion coefficient was found to be larger in necrotic areas than in vital tumor areas (23) which may result in higher signal intensities in T_2-weighted ^{1}H-SE images. Next, ^{19}F-SE density images were obtained at the same position as the ^{1}H-SE images using the following parameters: TR = 8 s, TE = 0.03 s, NS = 2, matrix size = 64 x 64, FOV = 15 x 15 mm and slice thickness 4 mm. The ^{19}F-SE density images were used for analyses of the 2D distribution of PFCs in similar slices as used in in vivo ^{19}F-MR relaxometry studies.

In vivo ^{19}F-MR relaxometry studies were performed with a slice-selective inversion-recovery T_1-sequence with similar acquisition parameters as used in the T_1 sequence for the determination of the in vitro calibration curve. The pulse width of the $90°$ sinc excitation pulse was optimized for a slice thickness of 4 mm. Eight TIs were used between 0.8 and 8 s, TR = 12 s, NS = 4, total measurement time 384 s. Two T_1 measurements were performed before carbogen breathing and subsequently two during carbogen breathing.

To obtain an in vivo $1/T_1$ value for the calibration curve at pO_2 = 0 mmHg, four independent in vivo experiments in mice were performed. T_1-values of ^{19}F-spins before and every 6-min after the killing of mice were determined with the slice-selective inversion-recovery T_1-sequence as described earlier. Mice were killed by switching off the oxygen supply and 1 min afterwards the total supply of anesthesia was stopped. Experiments on dead mice were finished when T_1-values of ^{19}F-spins reached a steady state. The temperature of the skin adjacent to tumor tissue was monitored on line and was kept at $36°$- $37°$ C using the same feedback system and rectal probe as mentioned above. Note that the T_1-relaxation time of ^{19}F-spins is not only related to the oxygen tension in tissue, but also to tissue temperature. Therefore, temperature control is important in all experiments.

Data analyses. From 3 independent in vitro measurements the calibration curve ($1/T_1$ (s^{-1}) versus pO_2 (mmHg)) was obtained by linear regression analyses with Graphpad software (Graphpad PRISM, version 2.0, San Diego, USA). As the intercept value of the calibration curve at pO_2= 0 mmHg, the mean $1/T_1$ as measured in 4 dead mice was applied. This calibration curve was used to convert in vivo T_1-relaxation rates (R_1) of ^{19}F-spins to $pO_{2/relaxo}$ values. The standard errors of the intercept value and the slope of the calibration curve were propagated in the calculations of the SEM of absolute mean $pO_{2/relaxo}$ values per tumor slice in experiments without carbogen breathing (n = 2) or were propagated in calculations of the SE of changes in the $pO_{2/relaxo}$ values after 8 and 14 min carbogen breathing. For carbogen breathing experiments the average $pO_{2/relaxo}$ changes of all tumors (n = 13) was analyzed with a paired t-test.

Polarographic measurements of the oxygen tension in tumor tissue.

One day after the ^{19}F-MR experiments invasive pO_2 measurements were performed with a computerized polarographic system (KIMOC 6650, Eppendorf, Hamburg). The details of this technique have been described previously (8, 24). Briefly, the intratumoral pO_2 was registered with a polarographic needle ($pO_{2electode}$) with a diameter of 300 μm. The sensitive membrane-covered cathode has a diameter of 17 μm resulting in a hemispherical measuring volume with a diameter of approximately 50 μm around the tip of the electrode (25).

In order to reduce the resistance of the skin during the insertion of O_2-electrodes in tumors, a small hole was made in the skin adjacent to tumor tissue using a needle with a similar diameter as the O_2-electrodes. Tissue compression artifacts were minimized with forward movements of the O_2-electrode (500 μm) immediately followed by a backward step of 200 μm (26).

Tumor oxygenation measurements were performed along two perpendicular tracks in the comparable tumor slices as used in the slice selective ^{19}F-MR relaxometry. Per track 12 individual $pO_{2/electrode}$ data points were measured. The drift was < 0.4 %. min^{-1}. $PO_{2/electrode}$ values of a track were omitted, when the tumor started bleeding after insertion of the O_2-electrode. The raw data of the $pO_{2/electrode}$ measurements were exported from the KIMOC device into a personal computer for statistical analyses.

Data analyses. Per tumor slice the median $pO_{2/electrode}$ value of both tracks was calculated (n = 24). Next, in the same slice the mean of the $pO_{2/electrode}$values was calculated from these sample points, that coincided with the PFC distribution in the perfused tumor rim (n = 2). These values appeared to be the first and maximum values of the sampled data points in both tracks, therefore this physiological parameter was denoted as the mean maximum $pO_{2/electrode}$ value. Both the median $pO_{2/electrode}$ value and the mean *maximum* $pO_{2/electrode}$were compared to the absolute mean $pO_{2/relaxo}$ values.

Fluorescence microscopy and (immuno)histochemical analyses of the 2D distribution of perfused microvessels, hypoxic- / necrotic areas and macrophages. In complete transverse tumor sections morphometric analyses of perfused microvessels, hypoxic- / necrotic areas and macrophages were performed using a computer-controlled digital-image analyses system connected to a (fluorescence) microscope. One day after the polarographic measurements 0.3 ml of a suspension was injected i.p. which contained the following chemical compounds: 0.5 ml dimethylsulphoxide, 4.5 ml heated peanut oil and 70 mg of the hypoxia marker 7(-)[4'-(2-nitroimidazol-1-yl)-butyl]-theophylline (NITP, a generous gift of Dr. R. Hodgkiss, CRC Gray Laboratory, Mount Vernon Hospital, Northwood, Middlesex, UK). Two hours after administration of the hypoxic marker NITP, a 0.05 ml solution of saline (0.9 %, pH=7.4) containing a fluorescent perfusion marker Hoechst 33342 (15 mg/kg, Sigma, St.Louis, MO, USA) was injected i.v. via a lateral tail vein. One minute after Hoechst injection, mice were rapidly killed by dislocation of their neck, and tumors were quickly removed and frozen in liquid nitrogen preventing the redistribution of fluorescent perfusion marker Hoechst. Tumors were cut in halve: one half was used for quantitative immunohistochemical analyses of perfused microvessels, the total microvascular bed, hypoxic areas and the 2D distribution of macrophages. The other half was used for classical histological staining with eosin (cyto-plasm) and haematoxylin (nuclei). For each tumor half, three frozen tissue sections (5 μm) at comparable locations as the slices in ^{19}F-MR relaxometry experiments were made. The staining with eosin and haematoxylin was used to distinguish viable tumor areas from necrotic areas.

Immunohistochemical analyses. The different cells and cell structures were analyzed in four steps: the perfused microvessels were analyzed first followed by the immunohistochemical staining of hypoxic areas, the endothelium of all microvessels and macrophages. After each staining step, sections were scanned using an extended version of the digital image analyses system as described by Rijken et al (19). After processing all fields of each scan a composite image was reconstructed from the individual processed fields revealing the different structures. If the composite images of the tumor sections obtained after each step were combined, then the new matched image showed the 2D distribution of perfused microvessels, hypoxic areas, the total microvascular bed and macrophages.

For the staining of hypoxic areas, sections were incubated with rabbit anti-theophylline (Sigma, St. Louis, MO, USA) followed by incubation with FITC-labeled donkey anti-rabbit immunoglobulin (Jackson ImmunoResearch Laboratories, West Grove, USA).

The endothelium of all microvessels was first stained with monoclonal rat anti-mouse antibody ME 9F1 (27), followed by the second and third antibody TRITC-labeled goat anti-rat immunoglobulin and donkey anti-goat immunoglobulin (Jackson ImmunoResearch Laboratories, West Grove, USA). In different tumor sections, but adjacent to sections with hypoxic cell staining, the macrophages were stained with monoclonal rat antibody to mouse macrophage (clone F4/80, rat IgG-2b, Caltag laboratories, Burlingame, CA, USA). The second antibody was rhodamine-labeled rabbit anti-rat IgG (Cappel-Organon Technika, Durham, NC, USA). In the same sections as used for the analyses of the macrophage distribution the basal lamina of the tumor vasculature was stained with collagen type IV poly-clonal antibody (goat antitype IV collagen, Southern Biotechnology Associates, Birmingham, AL, USA) and donkey anti-goat immunoglobulin labeled with FITC (Jackson ImmunoResearch Laboratories, West Grove, USA).

Data analyses. Per tumor section the 2D distribution of macrophages, perfused microvessels, hypoxic and necrotic areas was compared to the 2D distribution of PFC compounds in ^{19}F-SE density MR-images and the 2D distribution of high intensity regions in T_2-weighted ^{1}H-SE MR-images, respectively. Per tumor section the hypoxic fraction and the necrotic fraction were calculated. Both parameters are defined as the total hypoxic or necrotic area per total tumor section area. Next, an average necrotic and hypoxic fraction was calculated for all tumors (n = 13).

Results

Calibration curve for oxygen tension measurements by ^{19}F-MR relaxometry.

In vitro ^{19}F-MR relaxometry measurements of the PFC emulsion (40% (v/v) at a temperature of 37° C for 5 different oxygen tensions (pO_2, mmHg) resulted in the following calibration curve, see Eq. [1]:

$$\frac{1}{T_1} = 0.44 + 0.0028. \, pO_2 \qquad\qquad [1]$$

The standard error (SE) of the intercept value (0.44 (s^{-1})) is 2.3 %, and the SE of the slope (0.0028 $(s.mmHg)^{-1}$) is 1%. The $1/T_1$ value obtained from the in vivo ^{19}F-MR relaxometry studies on 4 dead mice was 0.41 ± 0.02 (SEM) s^{-1}. This $1/T_1$ value is not significantly different from the intercept value of the in vitro measurements. For calculations of absolute mean $pO_{2/relaxo}$ values in the following sections this value of 0.41 s^{-1} was used as intercept. It should be noted that the intercept is not needed for calculations of changes in the $pO_{2/relaxo}$ values.

Comparison of the 2D distribution of PFCs in ^{19}F-SE density MR-images and high intensity areas in T_2-weighted ^{1}H-SE MR-images with the 2D distribution of perfused microvessels, hypoxic - / necrotic areas and macrophages.

Three days after intravenous injection of PFCs the 2D distribution of PFCs in ^{19}F-SE density images correspond mainly to the 2D distribution of perfused microvessels in Hoechst images, see e.g. tumors no. 10 and 11 in Figure 5.1A and 5.1B. All tumors were well perfused in the periphery and no perfused microvessels were detected in the center. The nonperfused regions in Hoechst images correlated with high intensity areas in T_2-weighted ^{1}H-SE MR-images (Figure 5.1B and 5.1C). A detailed analysis of such a nonperfused area is shown in Figure 5.2 for tumor no. 10. In eosin and haematoxylin stained sections these areas appeared necrotic (Figure 5.2B). The average necrotic fraction of all 13 tumors was 0.5 ± 0.06 (SEM) (-). In only 5 of the 13 tumors NITP labeled cells (~ hypoxic cells) could be detected. The average hypoxic fraction of these 5 tumors was 0.01 ± 0.0013 (SEM) (-). In general, a thin layer of NITP labeled cells surrounded extensive necrotic cords, see e.g. tumor no. 2 in Figure 5.3A and 5.3B. For this tumor line comparable results were obtained with another hypoxic marker pimonidazole hydrochloride (PIMO) (P. Rijken M.Sc., oral communication, November 1997). In only one tumor a small isolated group of macrophages was observed in the perfused tumor rim (results not shown) of which the 2D distribution did not correlate with the distribution of PFCs.
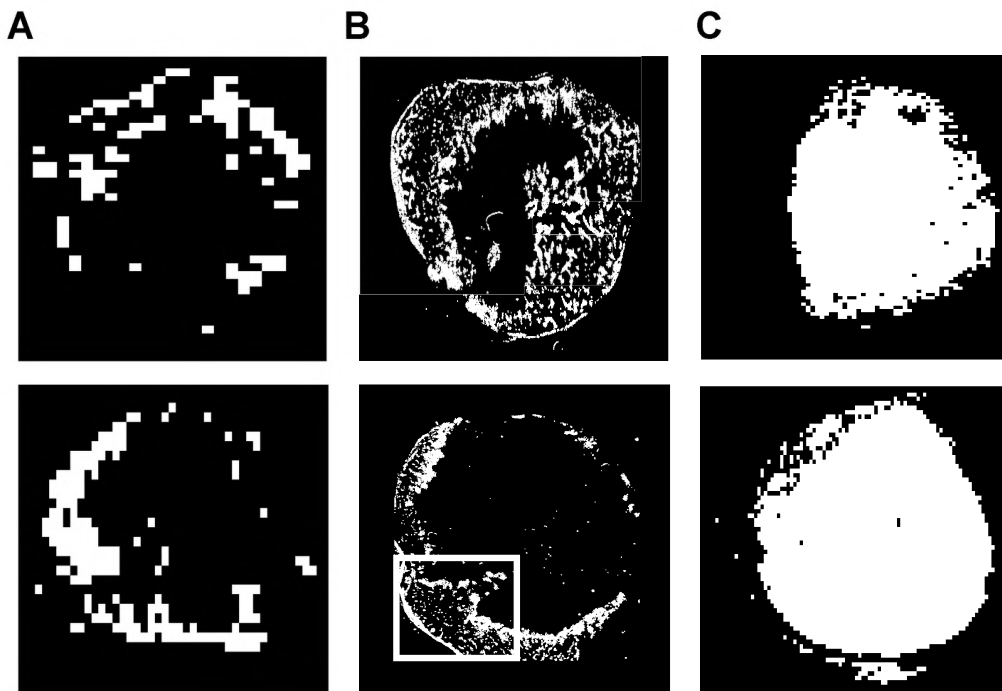
Figure 5.1A shows the PFC distribution in ^{19}F-SE density MR-images of a slice through the center of tumors no. 10 and no. 11. **Figure 5.1B** displays the 2D perfused microvessel (white structures) distribution in fluorescence microscopic Hoechst images of comparable slices and **Figure 5.1C** shows the ^{1}H-signal intensities in T$_2$-weighted ^{1}H-SE MR-images in similar slices as the ^{19}F-MRI studies. Detailed analyses of the delineated area in Figure 5.1B are given in Figure 5.2.

Figure 5.2 Representative results of histological analyses of nonperfused regions in tumor no. 10 are shown in this Figure. An area of Figure 5.1B delineated by the rectangle is analyzed in more detail in Figure 5.2A and 5.2B. **Figure 5.2A** shows the distribution of perfused microvessels (white structures) and in **5.2B** the results of the haematoxylin (nuclei) and eosin (cytoplasm) staining (HE) are displayed. The light gray colors correspond to necrotic areas (N) and the more dark gray colors are related to perfused tumor areas (P) in Figure 5.2A.
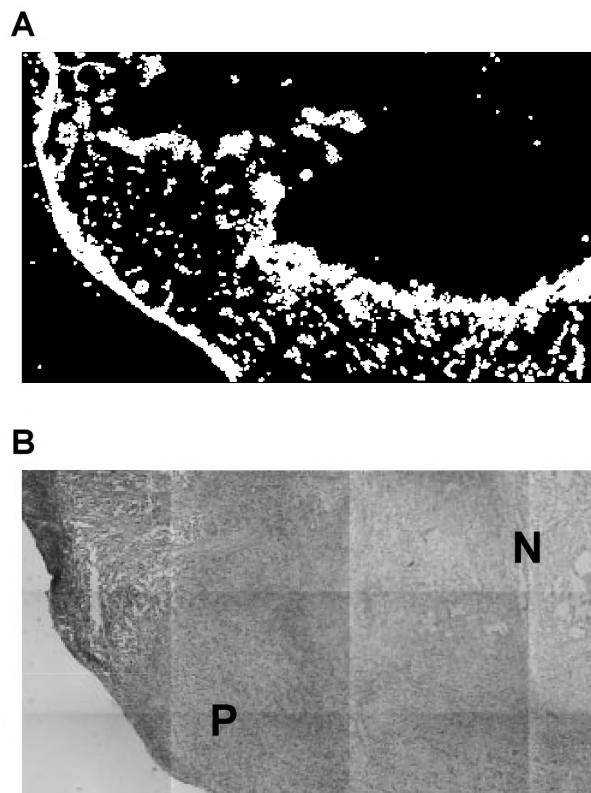
Comparison of median $pO_{2/electrode}$ values with absolute mean $pO_{2/relaxo}$values in tumor tissue slices.

Low S/N ratios in ^{19}F-MR spectra of PFCs in the whole tumor did not permit voxel-selective T_1-measurements or local $pO_{2/relaxo}$ studies within a reasonable time (11). Absolute mean $pO_{2/relaxo}$ values were measured in perfused regions of the tumor throughout the whole MR-slice (see previous paragraph), and ranged from 0.03 to 49.7 mmHg (see Table 5.1). In tumor no. 4 with a mean $pO_{2/relaxo}$ value of 49.7 mmHg an important region with low ^{1}H-signal intensities was found near the center of the tumor in T_2-weighted ^{1}H-SE MR-images, probably corresponding to extravasation of hemoglobin. In this region the blood oxygen tension directly effects the T_1-relaxation time of ^{19}F-spins of PFC compounds, which may result in high $pO_{2/relaxo}$ values.

Polarographic measurements were done in two perpendicular tracks located within the slices, as measured in the corresponding in vivo ^{19}F-MR relaxometry studies. For tumor no. 10 a fluorescence microscopic image (Hoechst image) of the perfused microvessel distribution is displayed in Figure 5.4A including the approximate locations of the tracks. The $pO_{2/electrode}$ values obtained during the stepwise movement of the Eppendorf electrode in one track are shown in Figure 5.4B. The $pO_{2/electrode}$ values decreased from the periphery of the tumor to the center. Median $pO_{2/electrode}$ values of tumors denoted by asterisks in Table 5.1 varied from 0.4 to 3.3 mmHg. Four of the 13 tumors started bleeding during the insertion of O_2-electrodes and data were not further evaluated. Tissue injuries related to the Eppendorf electrode measurements were only observed in two of 9 remaining tumors, but this did not influence the (immuno)histochemical analyses in whole tumor sections, since $pO_{2/electrode}$ values were locally sampled in two tracks.

For the tumors studied by both methods the median $pO_{2/electrode}$ values were generally lower than the mean $pO_{2/relaxo}$ values (Figure 5.5). However, when the mean *maximum* $pO_{2/electrode}$ values which originated from the tumor periphery were compared with mean $pO_{2/relaxo}$ values, a much closer correlation between both data sets was observed as indicated by the solid line in Figure 5.5 (= approaching the line of identity). Finally, no relationships were found between necrotic and hypoxic fractions and mean $pO_{2/relaxo}$ values or median $pO_{2/electrode}$ values.

Figure 5.3 A detailed analysis of hypoxic and necrotic areas of tumor no. 2 are depicted in **A** and **B**, respectively. Three different (cell) structures were labeled in **A**: perfused microvessels (P, blue), endothelium of all microvessels (red) and hypoxic cells (H, green). Hypoxic cells appear at a distance of 100 - 150 μm from perfused microvessels. Differences between the staining of nuclei (haematoxylin) and cytoplasm (eosin) in necrotic regions and areas with viable tissue are shown in **B**. The perfused and viable tissue regions (P) have a more uniformed nuclei staining than necrotic regions (N).

A

B
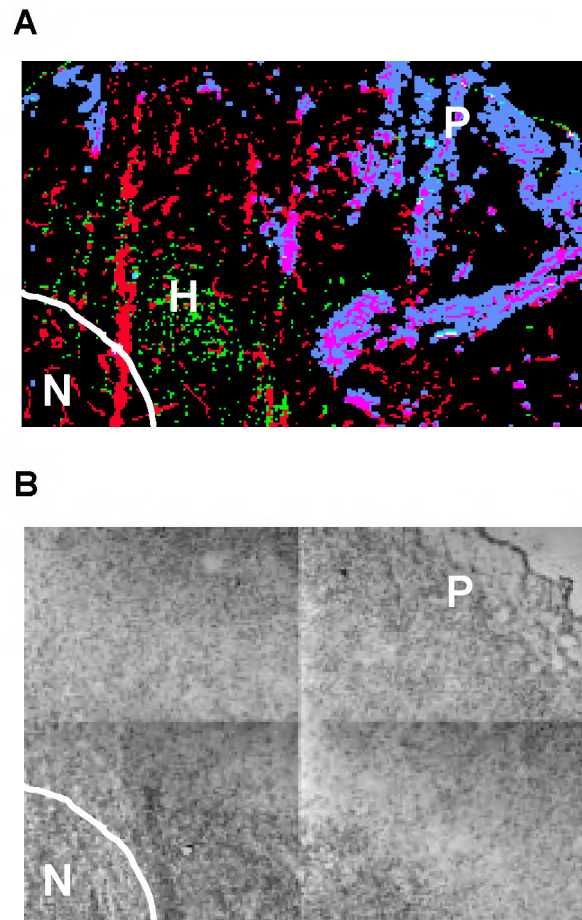
Table 5.1 In vivo ^{19}F-MR relaxometry measurements of absolute mean $pO_{2/relaxo}$ values (mmHg) and changes in $pO_{2/relaxo}$ values relative to baseline ($\Delta pO_{2/relaxo}$, mmHg) after 8 and 14 min carbogen breathing. In tumors denoted by an asterisk the oxygen tension was also measured by polarography (Figure 5.5). The values in column 3 are means ± SEM The values in column 4 and 5 are mentioned with their SE.

No.	Volume (cm^3)	$mpO_{2/relaxo}$	$\Delta pO_{2/relaxo}$ (8 min)	$\Delta pO_{2/relaxo}$ (14 min)
1*	0.70	8.8 ± 0.6	2.8 ± 4.3	0.2 ± 3.0
2*	1.10	0.3 ± 1.0	2.3 ± 3.4	0.7 ± 3.7
3*	0.60	8.6 ± 0.6	4.1 ± 5.1	0.9 ± 4.1
4	*0.41*	*49.7 ± 2.5*	*15.1 ± 11*	*1.7 ± 7.2*
5*	0.56	0.8 ± 0.4	2.7 ± 4.3	3.5 ± 5.0
6*	0.65	2.8 ± 0.9	0.5 ± 3.5	2.1 ± 4.0
7*	0.30	0.03 ± 3.0	5.3 ± 3.7	1.2 ± 3.5
8	0.31	9.1 ± 0.2	9.3 ± 5.8	6.6 ± 3.1
9	0.40	8.4 ± 0.1	5.0 ± 4.0	5.4 ± 3.6
10*	0.41	8.7 ± 0.9	2.8 ± 3.4	0.4 ± 3.7
11*	0.34	0.9 ± 0.4	0.03 ± 3.7	1.3 ± 3.5
12	0.37	13.5 ± 1.4	5.9 ± 3.6	0.1 ± 3.6
13*	0.39	3.1 ± 0.5	0.6 ± 4.9	3.5 ± 5.6

In vivo ^{19}F-MR relaxometry studies of the oxygen tension changes in tumor tissue during carbogen breathing.

Changes in the $pO_{2/relaxo}$ values were measured in complete tumor tissue slices. Table 5.1 presents the $pO_{2/relaxo}$ changes in slices through the center of 13 tumors after 8 and 14 min carbogen breathing. After 8-min carbogen breathing a small increase of the $pO_{2/relaxo}$ tensions relative to baseline was observed in 12 of the 13 mice. The $pO_{2/relaxo}$ changes were rather heterogeneous and varied from 0.03 to 15 mmHg. The average oxygen tension increase ($\Delta pO_{2/relaxo}$) of all tumors (except tumor no. 4) = 3.3 ± 0.8 (SEM) mmHg and was significantly different from zero ($p < 0.01$). In 9 of 13 mice the increase of the $pO_{2/relaxo}$ values reduced after 14-min carbogen breathing: these values relative to baseline varied from 0.1 to 6.6 mmHg. The average $\Delta pO_{2/relaxo}$ was 2.1 ± 0.6 (SEM) mmHg, which still was significant different from zero ($p < 0.05$), but was not significant different from changes after 8 min carbogen breathing ($p > 0.05$).

A

B
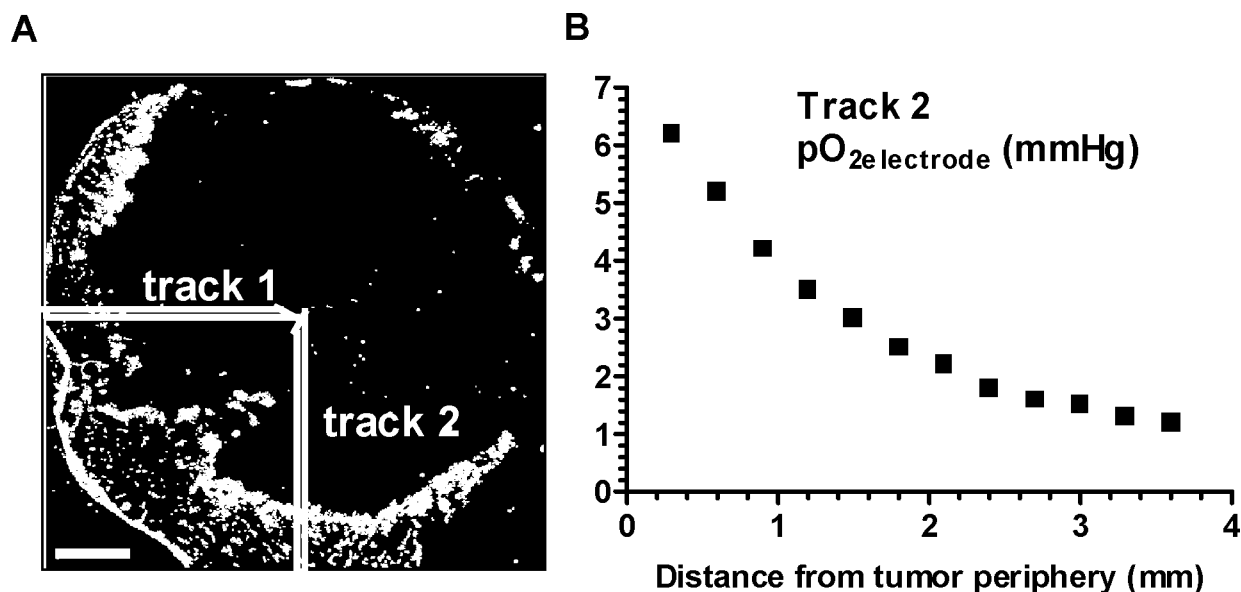
Figure 5.4 A fluorescence microscopic image (Hoechst image) of the 2D distribution of perfused microvessels (white structures) in a slice through the center of tumor no. 10 is shown in **A**.The length of the white bar corresponds to 1 mm. In the same Figure 5.4A, the approximate locations of two perpendicular tracks of the O_2-electrode are displayed. **Figure 5.4B** shows the individual $pO_{2/electrode}$ values (mmHg) of track no. 2 (y-axis) as obtained during the stepwise movement of the Eppendorf electrode from the periphery of the tumor to the center (x-axis) (stepsize 0.3 mm, total length of track 3.6 mm).

Figure 5.5 Comparison between absolute mean $pO_{2/relaxo}$ values (mmHg) per tumor tissue slice and median $pO_{2/electrode}$ values ± SEM (dashed line) or mean *maximum* $pO_{2/electrode}$ values ± SEM (solid line) as detected in 2 perpendicular tracks in comparable slices (Figure 5.4). The lines indicate the results of least-squares linear regression analyses (R^2 = 0.96, solid line and R^2 = 0.95, dashed line) using Graphpad PRISM software (version 2.0, San Diego, USA). Both lines were forced to go through the origin during the regression analyses. Detailed analyses of tumor no. 10 denoted by an asterisk (*) are given in Figure 5.4.
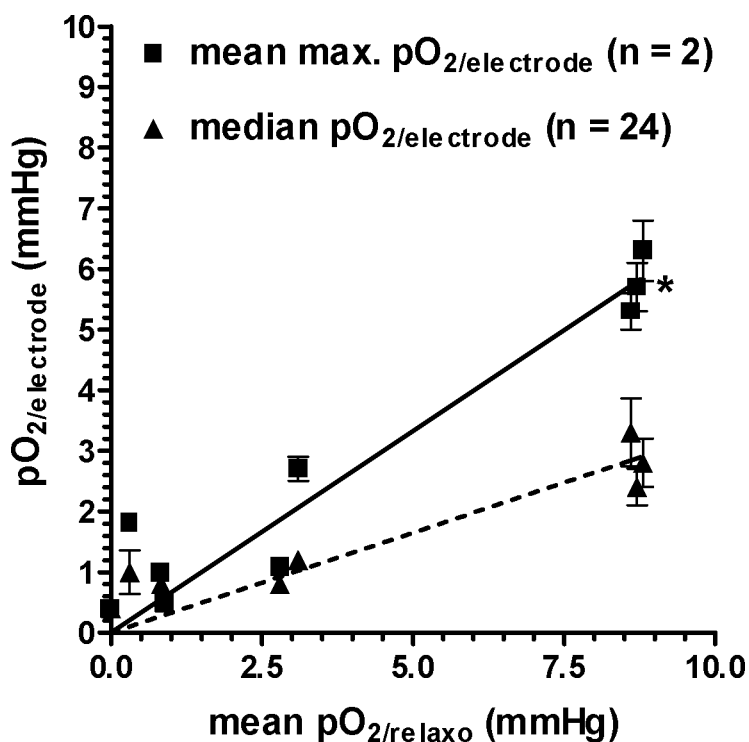
Discussion

In contrast to polarographic measurements, ^{19}F-MR relaxometry of perfluorocarbon compounds permits noninvasive oxygen tension measurements independent of the location of the tumor. However, this new method does not allow direct analyses of the oxygen tension: local oxygen tensions are derived from T_1-relaxation rates of ^{19}F-spins in the perfluorocarbon compounds. These relaxation rates may also depend on other physiological and histological parameters, and therefore $pO_{2/relaxo}$ values have been compared to $pO_{2/electrode}$ values in this study. In addition to ^{19}F-MR relaxometry and polarographic studies, the spatial distribution of PFC compounds over the tumor was determined and correlated to the location of the oxygen electrodes in tumor tissue, and to the distribution of perfused microvessels, hypoxic and necrotic areas. In this way, a proper comparison between both techniques becomes possible, because the tumor areas from which the measured $pO_{2/relaxo}$ and $pO_{2/electrode}$ values originate are known.

Calibration curve.

The relationship between the T_1-relaxation rates ($1/T_1$) of ^{19}F-spins in perfluoro-15-crown-5-ether and oxygen tensions was determined under strict temperature control, because T_1-relaxation rates of PFCs also have an inverse relationship with temperature (11). The intercept and slope value of the calibration curve of the neat perfluoro-15-crown-5-ether obtained in this study were larger than the values reported elsewhere (11). This may be due to a number of differences in experimental conditions, such as the ways to control temperature and to maintain O_2 levels during the in vitro ^{19}F-MR relaxometry examinations. In the present study the intercept values obtained from in vitro studies and ^{19}F-MR experiments on dead mice were not significantly different using the same temperature control system. These results indicate that the temperature of the tumors and the emulsion was comparable and differences in physiological properties such as, salt concentrations, pH, presence of proteins and PFC concentrations do not influence the T_1-relaxation rates of PFCs (16, 28). A simultaneous determination of tissue temperature and tissue oxygen tensions would be necessary to exclude the effect of temperature differences on T_1-relaxation rates of PFCs. This is possible with PFCs, which have two or more resonances in ^{19}F-MR spectra (14), but this cannot be done with perfluoro-15-crown-5-ether, which has 20 equivalent fluorine atoms resonating at a single frequency. The correlation between the $pO_{2/relaxo}$ and $pO_{2/electrode}$ data in this study suggest that the calibration curve is reliable and can be used to convert in vivo $1/T_1$ values of ^{19}F-spins of PFCs to in vivo $pO_{2/relaxo}$ values.

In vivo ^{19}F-MR relaxometry studies and polarographic measurements of oxygen tensions in tissue slices of human glioma xenografts.

Dardzinski and Sotak (11) used a fast MR-imaging technique to measure voxel-selective T_1-relaxation rates of perfluoro-15-crown-5-ether or local oxygen tensions. In the present study, low signal to noise ratios in ^{19}F-MR spectra of PFCs in the whole tumor did not permit to perform such studies within a reasonable time. The signal to noise ratios were lower, because the amount of administrated perfluoro-15-crown-5-ether had to be 2.4 times smaller than the dose used in the studies reported by Dardzinski and Sotak (11). Their dose was lethal to nude mice in our study. In addition, the permeability of microvessels for perfluoro-15-crown-5-ether in RIF-1 tumors may be larger than the permeability of microvessels in the glioma

xenograft line used in the present study. Intertumoral variations of microvessel permeability for perfluoro-15-crown-5-ether were also observed in different glioma xenograft lines (results not shown).

Three days after intravenous administration, the perfluorocarbons became mainly sequestered in the well-perfused rim of the human glioma xenografts as observed in ^{19}F-SE density MR-images and histological analyses. In a previous study these histological analyses of the 2D perfused vascular architecture have been validated by fast dynamic [1]H-MR imaging studies of contrast-agent uptake (29). One minute after bolus injection, the 2D distribution of the contrast agent in [1]H-MR images was found to be similar to the distribution of perfused microvessels 1 min after the injection of the fluorescent marker Hoechst. In the present study, the PFC distribution did not spatially correlate with the distribution of macrophages; thus, these cells as suggested by Longmaid et al (18) do not take up PFCs. The long-term retention of PFCs in perfused regions indicate, however, that they are firmly bound to tissue or cell structures in perfused regions of the tumor rather than redistributed in the whole tumor volume. The latter hypothesis could not be tested with (immuno)histochemical methods applied in the present paper, since analyses at the subcellular level were not possible. Mason et al (15) suggested also that PFCs became sequestered in well-perfused regions of Dunning prostate tumors, but did not provide any evidence for this suggestion. In this study and probably in the study of Mason et al (15), absolute mean $pO_{2/relaxo}$ values and changes in $pO_{2/relaxo}$ tensions are mainly measured in perfused regions of tumors.

However, in the evaluation phase before radiotherapy oxygen tension measurements in chronically hypoxic areas appear of greater interest than pO_2 measurements in perfused regions of tumors. In immunohistochemical analyses of chronically hypoxic cells with the bioreductive chemical probe NITP, a thin layer of NITP labeled cells was found adjacent to extensive necrotic cords in a few human glioma xenografts. In some tumors hypoxic cells as detected by NITP were even absent. In general, hypoxic areas were much smaller than perfused tumor regions that contain most of the PFCs. Therefore oxygen tension measurements in hypoxic areas using ^{19}F-MR relaxometry seems not possible in the tumor line used in the present study. Other human glioma xenograft lines showed larger areas with NITP labeled cells (Paul Rijken M.Sc., oral communication, November 1998). In these tumor models intratumoral injections of PFCs is an attractive alternative compared to i.v. administration of PFCs to assess tissue pO_2 in hypoxic regions (15, 17). However, also in this approach hypoxic areas may not be included, as these cannot be selected beforehand.

In the well-perfused tumor rim, the mean oxygen tensions as measured by ^{19}F-MR-relaxometry ($pO_{2/relaxo}$) were comparable to the mean of the maximum $pO_{2/electrode}$ values of both tracks that originate from the same perfused tumor rim. The absolute mean oxygen tension values in perfused regions were found to be relatively low in both analyses. Others also obtained low oxygen tension values in animal tumor models using polarographic or ^{19}F-MR relaxometry measurements (8, 13, 17, 30-34). Recent phosphorescence quenching microscopic analyses of pO_2 profiles in human colon adenocarcinoma xenografts with a spatial resolution of 10 μm showed that the pO_2 near perfused microvessels was approximately 14 mmHg and decreases monotonically until hypoxic values (< 5 mmHg) at a distance of 70 - 80 μm away from the nearest capillary wall (35). The mean pO_2 along the distance of 80 μm was approximately 8.4 mmHg, which is comparable to maximum $pO_{2/relaxo}$ and $pO_{2/electrode}$ values as measured in the perfused rim of the glioma xenograft line in this study. Although, O_2-consumption rates of tumor cells and O_2-diffusion coefficient may not be similar in human glioma xenografts, these results suggest that slice-selective ^{19}F-MR

relaxometry measurements of PFCs sequestered in the perfused rim of tumors probe a mean oxygen tension of O_2 profiles pertinent to perfused microvessels. The same is probably true for polarographic analyses of oxygen tensions, because the sample area of the O_2-electrode has approximately a diameter of 50 μm (25). Therefore, the mean maximum $pO_{2/electrode}$ values in the perfused tumor rim were comparable to mean $pO_{2/relaxo}$ values. If the median $pO_{2/electrode}$ value of both tracks was calculated, then this value was lower than the mean $pO_{2/relaxo}$ value, since low $pO_{2/electrode}$ values which originated from hypoxic and necrotic areas were also included in calculations of the median $pO_{2/electrode}$ values.

Effect of carbogen breathing on the mean $pO_{2/relaxo}$ values in tumor tissue slices.

In this study, ^{19}F-MR relaxometry measurements of intravenously injected PFCs did not only permit the determination of oxygen tensions in perfused areas, but also oxygen tension changes. A small but significant increase of the $pO_{2/relaxo}$ values was observed after 8 and 14 min carbogen breathing. In 9 of the 13 mice this increase tended to become smaller after 14-min carbogen breathing. If oxygen tension changes in perfused areas may cause radiosensitization, then maximum radiosensitivity is expected within the first 8 min after the start of carbogen breathing. ^{19}F-MR relaxometry measurements alone cannot give an explanation for this small decrease of $pO_{2/relaxo}$ values during carbogen breathing, but we may speculate that this has to do with the redistribution of O_2 by diffusion in tumor tissue after the start of carbogen breathing and/or the time to establish a new equilibrium between the increased O_2-supply and demand.

In the context of radiotherapy the detection of oxygen tension changes in chronically hypoxic areas are of greater interest. Perhaps the use of fluorinated bioreductive chemical probes may assess oxygen tension changes in chronically hypoxic regions noninvasively by ^{19}F-MR spectroscopy, although MR-sensitivity may limit their proper detection (36-39).

Conclusions. If perfluorocarbon compounds are administrated 3 days before the slice-selective ^{19}F-MR relaxometry experiments, then oxygen tensions and oxygen tension changes during carbogen breathing are mainly measured in perfused regions of the tumor throughout the whole MR-slice. In these regions, mean $pO_{2/relaxo}$ tensions have been validated by polarographic measurements. The effect of carbogen breathing on the oxygen tension in perfused areas was small but significant and tended to decrease with time.

References

1. Denekamp J. Does physiological hypoxia matter in cancer therapy? in: Steel GG, Adams GE, Peckham MJ, eds. The Biological Basis of Radiotherapy. Amsterdam, N-Y, Oxford: Elsevier: p. 139-155 (1983).

2. Gray LH, Conger AD, Ebert M, et al. The concentration of oxygen dissolved in tissues at the time of irradiation as a factor in radiotherapy. *Br J Radiol* **26**: 638-648 (1953).

3. Moulder JE, Rockwell S. Hypoxic fractions of solid tumors, experimental technique, methods of analyses and a survey of existing data. *Int J Radiation Oncol Biol Phys* **10**: 695-712 (1984).

4. Chaplin DJ, Horsman MR, Siemann DW. Further evaluation of nicotinamide and carbogen as a strategy to reoxygenate hypoxic cells in vivo: Importance of nicotinamide dose and preirradiation breathing time. *Br J Cancer* **68**: 269 – 273 (1993).

5. Rojas A, Joiner MC, Hodgkiss RJ, et al. Enhancement of tumor radiosensitivity and reduced hypoxia-dependent binding of a 2 nitroimidazole with normobaric oxygen and carbogen: A therapeutic comparison with skin and kidneys. *Int J Radiation Oncol Biol Phys* **23**: 361 – 366 (1992).

6. Siemann DW, Hill RP, Bush RS. The importance of the preirradiation breathing times of oxygen and carbogen (5% CO_2: 95% O_2) on the in vivo radiation response of a murine sarcoma. *Int J Radiation Oncol Biol Phys* **2**: 903 – 911 (1977).

7. Kaanders JHAM, Pop LAM, Marres HAM, et al. Accelerated radiotherapy with carbogen and nicotinamide (ARCON) for laryngeal cancer. *Radiother Oncol* **48**: 115 – 122 (1998).

8. Kallinowski F, Zander R, Hoeckel M, et al. Tumor tissue oxygenation as evaluated by computerized-pO_2-histography. *Int J Radiation Oncol Biol Phys* **19**: 953 –961 (1990).

9. Vaupel P, Schlenger K, Knoop C, et al. Oxygenation of human tumors: Evaluation of tissue oxygen distribution in breast cancers by computerized O_2 tension measurements. *Cancer Res* **51**: 3316 – 3322 (1991).

10. Baldwin NJ, Ng TC. Oxygenation and metabolic status of KHT tumors as measured simultaneously by ^{19}F magnetic resonance imaging and ^{31}P magnetic resonance spectroscopy. *Mag Reson Imaging* **14(5)**: 541 – 551 (1996).

11. Dardzinski BJ, Sotak CH. Rapid tissue oxygen tension mapping using ^{19}F inversion-recovery echo-planar imaging of perfluoro-15-crown-5-ether. *Mag Reson Med* **32**: 88 – 97 (1994).

12. Hees PS, Sotak CH. Assessment of changes in murine tumor oxygenation in response to nicotinamide using ^{19}F NMR relaxometry of a perfluorocarbon emulsion. *Mag Reson Med* **29**: 303-310 (1993).

13. Mason RP, Nunnally RL, Antich PP. Tissue oxygenation: A novel determination using ^{19}F surface coil nmr spectroscopy of sequestered perfluorocarbon compounds. *Mag Reson Med* **18**: 71-79 (1991).

14. Mason RP, Shukla H, Antich PP. In vivo oxygen tension and temperature: simultaneous determination using ^{19}F NMR spectroscopy of perfluorocarbon. *Mag Reson Med* **29**: 296-302 (1994).

15. Mason RP, Antich PP, Babcock EE, et al. Noninvasive determination of tumor oxygen tension and local variation with growth. *Int J Radiation Oncol Biol Phys* **29(1)**: 95 – 103 (1994).

16. Mason RP. Noninvasive physiology: ^{19}F NMR of perfluorocarbons. *Art Cells, Blood Subs, and Immob Biotech* **22(4)**: 1141 – 1153 (1994).

17. Mason RP, Rodbumrung W, Antich PP. Hexafluorobenzene: a sensitive ^{19}F NMR indicator of tumor oxygenation. *NMR Biomed* **9**: 125 – 134 (1996).

18. Longmaid HE, Adams DF, Neirinckx RD, et al. R.P. In vivo ^{19}F imaging of liver, tumor, and abscess in rats: preliminary results. *Invest Radiol* **20**: 141 – 145 (1985).

19. Rijken PFJW, Bernsen HJJA, van der Kogel AJ. Application of an image analyses system to the quantitation of tumor perfusion and vascularity in human glioma xenografts. *Microvascular Res* **50**: 141 – 153 (1995).

20. Bernsen HJJA, Rijken PFJW, Oostendorp T, et al. Vascularity and perfusion of human gliomas xenografted in the athymic nude mouse. *Br J Cancer* **71(4)**: 721 – 726 (1995).

21. van der Sanden BPJ, Heerschap A, van der Toorn A, et al. Effect of carbogen breathing on the physiological profile of human glioma xenografts. *Mag Res Med*, in press (1999).

22. Silver MS, Joseph RI, Hoult DI. Highly selective $\pi/2$ and π pulse generation. *J Mag Reson* **59**: 347 – 351 (1984).

23. Maier CF, Paran Y, Bendel P, et al. Quantitative diffusion imaging in implanted human breast tumors. *Mag Reson Med* **37**: 576 – 581 (1997).

24. Stüben G, Stuschke M, Kühmann K, et al. The effect of combined nicotinamide and carbogen treatments in human tumour xenografts: oxygenation and tumor control studies. *Radiother Oncol*, in press (1998).

25. Vaupel PW, Kelleher DK. Tumor oxygenation, in: Vaupel PW, Kelleher DK, Gunderoth M, eds., Functionsanalyse biologischer Systeme 24, Stuttgart: Gustav Fischer Verlag; 1995: p. 336.

26. Vaupel P, Kallinowski F, Okunieff P. Blood flow, oxygen and nutrient supply and metabolic microenvironment of human tumors: a review. *Cancer Res* **49**: 6449 – 6465 (1989).

27. Westphal JR, van 't Hullenaar RGM, van der Laak JAWM, et al. Vascular density in melanoma xenografts correlates with vascular permeability factor expression but not with metastatic potential. *Br J of Cancer* **76(5)**: 561 – 570 (1997).

28. Thomas SR, Pratt RG, Millard RW, et al. Evaluation of the influence of the aqueous phase bioconstituent environment on the F-19 T1 of perfluorocarbon blood substitute emulsions. *JMRI* **4**: 631 – 635 (1994).

29. van der Sanden BPJ, de Graaf RA, Rijken PFJW, et al. A comparative study of dynamic ^{1}H-MRI studies of Gd_DTPA uptake, perfused vessel distribution and hypoxic areas in human glioma xenografts (Abstr.). Proceedings of the 5th ISMRM meeting, Vancouver 1997: p. 1087.

30. Goda F, O'Hara JA, Rhodes ES, et al. Changes of oxygen tension in experimental tumors after a single dose of X-ray irradiation. *Cancer Res* **55**: 2249 – 2252 (1995).

31. Kelleher DK, Vaupel P. The effect of nicotinamide on microcirculatory function, tissue oxygenation and bioenergetic status in rat tumors. (Abstr.) In: Vaupel P, Eds. Oxygen transport to tissue XV New York, Plenum Press: p. 395 – 402 (1994).

32. Lee I, Boucher Y, Demhartner TJ, et al. Changes in tumour blood flow, oxygenation and interstitial fluid pressure induced by pentoxifylline. *Br J Cancer* **69**: 492 – 496 (1994).

33. Nozue M, Lee I, Hartford A, et al. pO_2 measurements in murine tumors by Eppendorf 'Histograph' : Calibration, reproducibility and comparison with diamond-general device. *Int J of Oncology* **9**: 995 – 962 (1996).

34. Thomas CD, Chavaudra N, Martin L, et al. Correlation between radiosensitivity, percentage hypoxic cells and pO_2 measurements in one rodent and two human tumor xenografts. *Radiation Res* **139**: 1 – 8 (1994).

35. Helmlinger G, Yuan F, Dellian M, et al. Interstitial pH and pO_2 gradients in solid tumors in vivo: High-resolution measurements reveal a lack of correlation. *Nature Med* **3(2):** 177 – 182 (1997).

36. Aboagye EO, Maxwell RJ, Kelson AB, et al. Preclinical evaluation of the fluorinated 2-nitroimidazole N-(2-hydroxy-3,3,3-trifluoropropyl)-2-(2-nitro-1-imidazolyl) acetamide (SR-4554) as a probe for the measurement of tumor hypoxia. *Cancer Res* **57**: 3314 – 3318 (1997).

37. Kwock L, Gill M, McMurry HL, et al. Evaluation of a fluorinated 2-nitroimidazole binding to hypoxic cells in tumor-bearing rats by ^{19}F magnetic resonance spectroscopy and immunohistochemistry. *Radiation Res* **129**: 71 – 78 (1992).

38. Maxwell RJ, Workman P, Griffiths JR. Demonstration of tumor-selective retention of fluorinated nitroimidazole probes by ^{19}F magnetic resonance spectroscopy *in vivo*. *Int J Radiation Oncol Biol Phys* **16**: 925 – 929 (1988).

39. Raleigh JA, Franko AJ, Kelly DA, et al. Development of an *in-vivo* ^{19}F magnetic resonance method for measuring oxygen deficiency in tumors. *Mag Reson Med* **22**: 451 – 466 (1991).

Chapter 6

In vivo ^{31}P magnetic resonance spectroscopy and
morphometric analyses of the perfused vascular
architecture of human glioma xenografts
in nude mice

Boudewijn P.J. van der Sanden
Paul F.J.W. Rijken
Arend Heerschap
Hans J.J.A. Bernsen
Albert J. van der Kogel

Abstract

The relationship between the bioenergetic status of human glioma xenografts in nude mice and morphometric parameters of the perfused vascular architecture was studied using ^{31}P-magnetic resonance spectroscopy (MRS), fluorescence microscopy and two-dimensional digital image analyses. Two tumor lines with a different vascular architecture were used for this study. Intercapillary distances and nonperfused area fractions varied greatly between tumors of the same line and tumors of different lines. The inorganic phosphate-nucleoside triphosphate (P_i/NTP) ratio increased rapidly as mean intercapillary distances increased from 100 µm to 300 µm. Two morphometric parameters - the percentage of intercapillary distances larger than 200 µm (icd_{200}) and the nonperfused area fraction at a distance larger than 100 µm from a nearest perfused vessel ($area_{100}$) - were deduced from these experiments and related to the P_i/NTP ratio of the whole tumor. It is assumed that an aerobic to anaerobic transition influences the bioenergetic status: i.e. the P_i/NTP ratio increased linearly with the percentage of icd_{200} and the $area_{100}$.

Introduction

Phosphorus magnetic resonance spectroscopy (^{31}P-MRS) studies of the bioenergetic status of tumors have been compared directly with tumor tissue pO_2 (1) and with several physiological parameters that affect pO_2 in tumor tissue, such as the intravascular concentration of oxyhaemoglobin (2) and tumor blood perfusion (3). ^{31}P-MRS has been demonstrated to be sensitive to tumor size (4, 5), with an increase in tumor size being supposed to have a negative influence on perfusion- and diffusion limited oxygen delivery and nutrient (6). The global bioenergetic status of a tumor, expressed as the P_i/NTP ratio, depends on the balance between the oxygen and nutrient supply, and the consumption rates of the tumor cells, which is related to the type of energy metabolism. This balance between supply and consumption determines the critical diffusion distances for oxygen and nutrients in tumor tissue. The total oxygen supply and nutrient supply depends on the tumor microcirculation and on the diffusion geometry.

The purpose of this study was to investigate the existence of a possible relationship between the global bioenergetic status and the diffusion geometry of human glioma xenografts in nude mice. A two-dimensional morphometrical analyses of the perfused vascular architecture of complete transverse tumor sections was performed. Morphometric parameters such as the percentage of large intercapillary distances and the fraction of nonperfused areas in a tumor section area are related to the diffusion limited oxygen delivery and nutrient delivery. Critical diffusion distances for oxygen and nutrients per perfused vessel can be estimated using a Krogh model (7-12). For example, the mean critical oxygen diffusion distance in gliomas using a Krogh model is approximately 100 μm. When tumor cells have an aerobic energy metabolism, changes in the percentage of intercapillary distances larger than approximately 200 μm are expected to effect the global bioenergetic status (P_i/NTP ratio). This indeed was observed. In addition, the mean fraction of the nonperfused tumor area at a distance larger than ~ 100 μm from the edge of a nearest perfused vessel was also found to be related to the global bioenergetic status of a tumor.

Material and Methods

Animal model. The same tumors of chapter 4, with a homogeneously (E98, n=10) and heterogeneously perfused vascular architecture (E49, n=14) were used in this study. The local ethical committee for animal use approved the experimental procedures.

In vivo ^{31}P-magnetic resonance spectroscopy. MRS measurements were performed on a vertical-bore Bruker spectrometer (4.7 T) employing a home-built $^{1}H/^{31}P$ double tunable three-turn solenoid coil with an inner diameter of 13 mm. The solenoid coil was fitted with a Faraday shield to eliminate spurious signals from normal tissue adjacent to the tumor. Mice with human glioma xenografts were excluded if host tissue was partially present in the volume sampled by the solenoid (tumor weight < 0.3 g) and when tumors were too large to fit completely in the solenoid (tumor weight > 0.9 g).

The mice were anaesthetized with a flow of 1.5 % enflurane in an oxygen-nitrous oxide (3:7) mixture applied through a nose-cone. Body temperature was monitored by a rectal probe (36-gauge wire, Hewlet Packard) and maintained at 36.5° - 37° C by a warm water blanket with a feedback system. ^{31}P-MR spectra were obtained with a one-pulse sequence with a hard pulse of 12 μs (optimized for maximum signal intensity) and a pulse repetition time of 5 s. The number of scans was 320.

As the ^{31}P-MRS experiments were carried out with an interpulse delay shorter than three times the T_1 of the ^{31}P spins of the P_i (i.e. approximately 4 s), the area of the P_i peak is not strictly proportional to its concentration (13). However, all in vivo spectra were run with the same acquisition parameters and in this group of tumors little effect is expected on the calculations of the P_i/NTP ratio at a pulse repetition time of 5 s.

Fluorescence Microscopy. After the MRS experiments, 0.05 ml solution of phosphate-buffered saline (PBS, pH=7.4) containing a fluorescent perfusion marker, Hoechst 33342 (15mg.kg^{-1}, Sigma, St.Louis,MO, USA), was injected i.v. via a lateral tail vein. One minute after injection, the mice were killed and tumors were quickly removed and frozen in liquid nitrogen, preventing the dye from diffusing too far into tissue. The tumor was cut in two halves: one half was used for the analyses of the perfused vascular architecture and the other half was used for classical histological staining with eosin (cytoplasm) and haematoxylin (nuclei).

Fifteen frozen tissue sections (5 μm) at random locations were made using a freeze microtome. Sections were processed at room temperature by a 15-min incubation with collagen Type IV polyclonal antibody (rabbit serum, Euro-Diagnostics, Oss, The Netherlands), a marker for the basal lamina of the tumor vasculature. Next, the sections were incubated with a second antibody, goat anti-rabbit immunoglobulin labelled with Tritc (Tago, Birlingame, CA, USA).

The whole tumor sections were analyzed in the fluorescence microscope using a digital-image processing system. A detailed description of this method is given by Rijken et al (14). Briefly, each section was scanned twice on a computer-controlled motorized stage of a
fluorescence microscope using two different excitation-emission filters. After processing all fields of each scan, a composite image was reconstructed from the individual processed fields, revealing the perfused vessels (Hoechst image) and the total vascular bed (collagen image) in separate scans. When both images were combined, the new matched image showed the perfused and nonperfused vessels.

In the next step, the fluorescent rim of Hoechst dye around perfused vessels, due to Hoechst diffusion into adjacent tissue, was deleted by image processing. In Hoechst images only, vascular areas are slightly overestimated.

Data analyses.

^{31}P-MR spectra. Zero filling and the convolution difference technique with line broadenings of 30 and 1000 Hz were applied to the free induction decay (FID). The peaks of the α,β,γ-NTP, P_i and, when present, phosphocreatine (PCr) were fitted to Lorentzian line shapes with NMR1 software (New Methods Research, Syracuse, NY, USA). The integral of the P_i peak and the sum of the integrals of the α,β,γ-NTP peaks were used in the calculation of the P_i/NTP ratio.

Calculation of the pH$_{mrs}$. The pH was deduced from the chemical shift of the P_i signal with respect to the chemical shift of the PCr signal, or the α-NTP signal in the absence of a PCr resonance. A modified Henderson-Hesselbach equation was used, with the following parameters: pK = 6.75, a (acid shift) = 3.29, b (base shift) = 5.7 (15, 16).

Vascular morphology of perfused vessels.

The percentage of intercapillary distances > 200 μm (icd$_{200}$). For each perfused vessel, a domain (17), i.e. the area of tumor tissue which is supposed to be supplied by the nearest perfused vessel, was determined in matched images. As a consequence, one domain contains one perfused vascular structure, and may contain nonperfused vascular structures and avascular regions. With the help of an image analyses system, line networks in Figure 6.1 represent contours of these domains. The shortest distance between neighbouring perfused vascular structures was used as an estimation of the icd. Note that neighbouring perfused vascular structures have adjacent domains. Thus, intercapillary distances were not determined between perfused vascular structures that did not have adjacent domains. Calculations of distances were started from perfused vessel walls. Icds obtained by a domain analyses are always larger than icds between perfused vessels, measured in perfused regions only (18). For each tumor, the frequency distribution of the icds was determined for all values calculated in the 15 tumor sections (Statistica, StatSoft, Tulsa, OK, USA). The percentage of intercapillary distances > 200 μm (icd$_{200}$) was obtained from the cumulative frequency distribution for the whole tumor.

The fraction of the nonperfused tumor area at a distance larger than 100 μm from a nearest perfused vessel (area$_{100}$). In matched images, a circle with a radius of 100 μm was drawn around every perfused vessel. For each tumor section, the tumor area outside the circles was determined and divided by the total tumor section area. Next, a mean nonperfused area fraction at a distance > 100 μm from a nearest perfused vessel was calculated for all 15 tumor sections.

The morphological parameter - the percentage of icd$_{200}$ - is probably less sensitive to the total nonperfused area than the parameter area$_{100}$. Only a few long icds (> 200 μm) may be responsible for the determination of a large nonperfused area. In other words, the weight of a few long icds in comparison with all icds is of less importance than the weight of the nonperfused areas in relation to the total tumor area.

Analyses of the relationship between the P_i/NTP ratio and the morphometric parameters.

Linear regression analyses was performed between the morphometric parameters, mentioned above, and the P_i/NTP ratios using Graphpad (Graphpad PRISM version 2.0, San Diego, USA). The goodness of the fit (R^2), the 95% confidence intervals and the p-value of the slope are given, i.e. test result of the significant difference of the slope from zero. Values presented in the text are means ± standard deviations (SD).
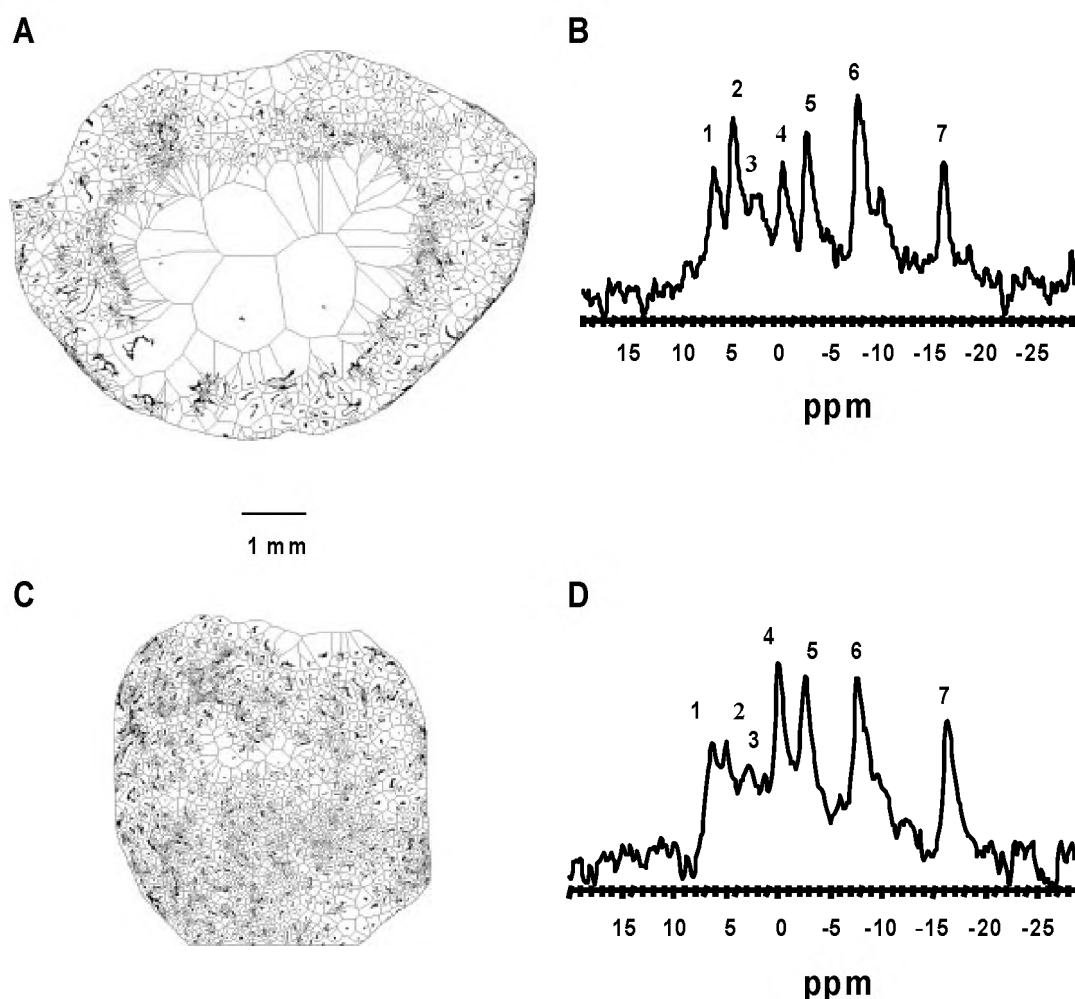
Figure 6.1 Matched digital images of a scanned tumor section at the centre of an E49 tumor no. 4 (**A**) and E98 no.15 (**C**) with the corresponding ^{31}P-MR spectra of the whole tumor (**B** and **D**). The perfused vessel structures are situated in a vessel domain delineated by the lines. Peak assignments of ^{31}P-MR spectra in **B** and **D**: 1, phosphomonoesters; 2, P_i; 3, phosphodiesters; 4, PCr; 5, γ-phosphate of NTP; 6, α-phosphate of NTP; 7, β-phosphate of NTP. The tumors depicted in this figure are similar to the tumors of Figure 4.4 in chapter 4.

Results

Comparison of vascular morphometric analyses of perfused vessels between the tumor lines (E49, E98) and host tissue.

In Figure 6.2, a frequency histogram of the icds is given for a single tumor and host tissue, i.e. skeletal muscle of the hindlimb. Tumor tissue showed an important tail of long icds in comparison with host tissue. Icds larger than 200 μm were not observed in host tissue; thus, the percentage of icd$_{200}$ = 0. The mean icd of host tissue was 35 ± 21 μm, which was much smaller than the mean icds per tumor for both lines, which varied between 102 ± 255 μm (E98, no. 6) and 526 ± 613 μm (E49, no. 23) (Figure 6.3). In skeletal muscle of the hindlimb, the mean area$_{100}$ was 0.07 ± 0.02 (-) and is smaller than the mean area$_{100}$ values found for the tumor line E49 & E98, which varied between 0.09 ± 0.02 (E98, no.1 & no. 6) and 0.84 ± 0.02 (E49, no. 23) (Figure 6.5).

Figure 6.2 Example of a frequency histogram of intercapillary distances in tumor tissue (E49, no.13) (□) and skeletal muscle (host tissue) (●). The percentage of cases per icd-interval of 20 μm (x-axis) is depicted on the y-axis. The figure is truncated at icds > 600 μm. The maximum icd of no.13 is 1918 μm.
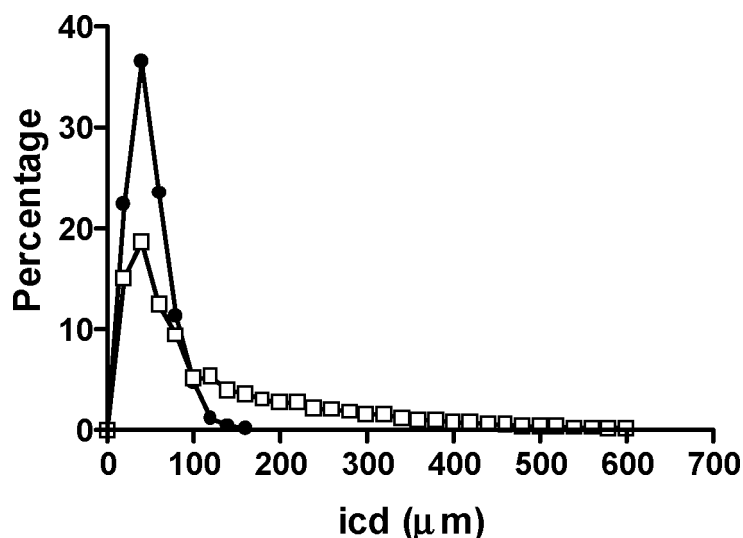
Vascular morphometric analyses of perfused vessels and ^{31}P-MRS.

The integral of the peaks in the ^{31}P-MR spectra reflects the quantity of phosphorylated metabolites (α,β,γ-NTP, P$_i$, PCr, PME, PDE) in viable tumor cells (19), in the volume sampled by the solenoid (approximate tumor volume). The P$_i$/NTP ratio is accepted as an indication of the energy status of cells (1, 2), where NTP is broken down to NDP and P$_i$ by the action of NTPases during cellular activities.

There was little or no contamination by PCr and NTP signals from muscle tissue. ^{31}P-MR spectra of tumors with similar weights showed PCr-peaks smaller than NTP-peaks, except some well-perfused tumors, e.g. E98 no. 15 (Figure 6.1). An example of the domain analyses for two different tumor sections of E49 no.4 and E98 no.15 is shown in Figure 6.1A & 6.1C with the corresponding ^{31}P-MR spectra of the whole tumors (Figure 6.1B and 6.1D). In Figure 4.4, the HDO-uptake curve of the same tumors is shown. Tumor E49 no. 4 showed a large nonperfused area in the centre, whereas tumor E98 no.15 showed a homogeneously perfused vessel distribution. The tumors had the following values for the morphometric

parameters: no. 4, percentage of icd_{200} = 22, mean $area_{100}$ = 0.52 ± 0.07; no. 15, percentage of icd_{200} = 7 and mean $area_{100}$ = 0.12 ± 0.04. The P_i/NTP ratio of no. 4: i.e. 0.45, was higher than the ratio of no. 15: i.e. 0.17.

P_i/NTP ratio and the mean intercapillary distance.

Figure 6.2 shows that a frequency distribution of icds in tumor tissue is not a normal distribution. An important tail of large icds (> 200 μm) was found in all tumors (results not shown here). Standard deviations were mostly larger than mean icds, with the exception of most E98 tumors, which showed a more homogeneously perfused vessel distribution. Therefore, the mean icd can only be used as a rough indication for differences in the icd distribution between tumors. In Figure 6.3, the mean icd per tumor for both lines is related to the P_i/NTP ratio. The P_i/NTP ratio showed the largest changes between a mean icd of approximately 100 μm and approximately 300 μm; the P_i/NTP ratio increased around a mean icd of approximately 200 μm.

Figure 6.3 Plot of the P_i/NTP ratio (-) vs the mean icd (μm) per tumor for the lines E49 (□) and E98 (■). One square represents one tumor.
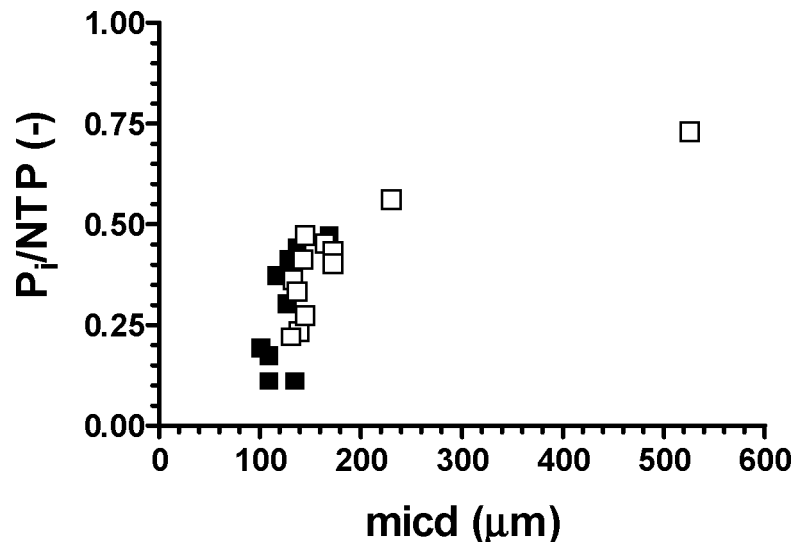
P_i/NTP ratio and the percentage intercapillary distance greater than 200 μm.

In Figure 6.4, the relationship between the P_i/NTP ratio and the percentage of icd_{200} is shown for the tumor lines E49 and E98. A linear relationship was found with a goodness of the fit (R^2) = 0.70. The slopes of the regression lines from both tumor lines were not significantly different (p > 0.01). The pooled slope was significantly different from zero (p < 0.0001). No relationship was found between the P_i/NTP ratio and the percentage of icds > 100 μm and the percentage of icds > 300 μm (results not shown here). The P_i/NTP ratio for the host tissue (hindlimb skeletal muscle) was 0.09 ± 0.01 and the percentage of icd_{200} = 0. The datapoint of the host tissue is depicted in Figure 6.4, but was not used in the regression analyses. The energy metabolism in muscle tissue cells probably differs from the energy metabolism in glioma tumor cells, so a direct comparison is not allowed.

P_i/NTP ratio and the nonperfused area fraction at a distance larger than 100 μm from a nearest perfused vessel (area$_{100}$).

In Figure 6.5, the relationship between the P_i/NTP ratio and the mean area$_{100}$ is shown. For both tumor lines, there was a linear relation between the P_i/NTP ratio and the area$_{100}$: $R^2 = 0.76$. The slopes of the linear regression lines of the tumor lines E49 & E98 were not significantly different ($p > 0.01$), but the pooled slope was significantly different from zero ($p < 0.0001$). No relationship was found between the P_i/NTP ratio and the mean area$_{50}$ and the mean area$_{150}$, as expected from the results obtained for icds as shown in the previous paragraph.

The goodness of the fit in Figure 6.5 was slightly better than in Figure 6.4, i.e. the morphometric parameter mean area$_{100}$ showed a better correlation with the P_i/NTP ratio than the percentage of icd$_{200}$. The datapoint of the host tissue was lower than the datapoints of the different tumors and was not used in the regression analyses (see previous paragraph).

pH_{mrs} and morphometric analyses of perfused vessels.

pH_{mrs} (approximate pH_i) was independent of the percentage of icd$_{200}$ and the area$_{100}$ over a large range of values (results not shown). All tumors showed a single P_i peak corresponding to pH_{mrs} values from about neutral ($pH \sim 7.0 \pm 0.1$) to basic ($pH \sim 7.3 \pm 0.1$). There were two exceptions in the E49 line: tumor no. 16 showed a split P_i peak, corresponding to pH values of 7.3 ± 0.2 and 6.8 ± 0.1; Tumor no. 23 had pH_{mrs} values of 7.12 ± 0.1 and 6.7 ± 0.1. The tumors had the following values for the morphometric parameters: no. 16, percentage of icd$_{200}$ = 37, mean area$_{100}$ = 0.63 ± 0.19; no. 23, percentage of icd$_{200}$ = 43 and mean area$_{100}$ = 0.84 ± 0.1.
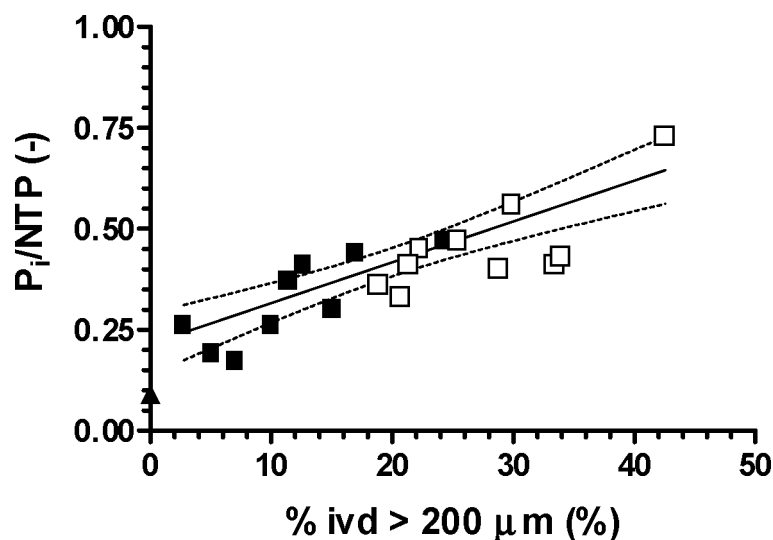
Figure 6.4 Plot of the correlation between the P_i/NTP ratio (-) and the percentage of intercapillary distances larger than 200 μm (icd$_{200}$ (%)). The line indicates the results of least-squares linear regression analyses ($R^2 = 0.70$) of the data for the tumor lines E49 (□), E98 (■): $y = 0.18 \pm 0.04 + 0.01 \pm 0.002 \times x$. The dashed lines show the 95% confidence intervals. One square represents one tumor. The P_i/NTP ratio (▲) for the host tissue (skeletal muscle hindlimb) is 0.09 ± 0.01 and the percentage of icd$_{200}$ = 0. The datapoint of the host tissue was not used in the regression analyses.
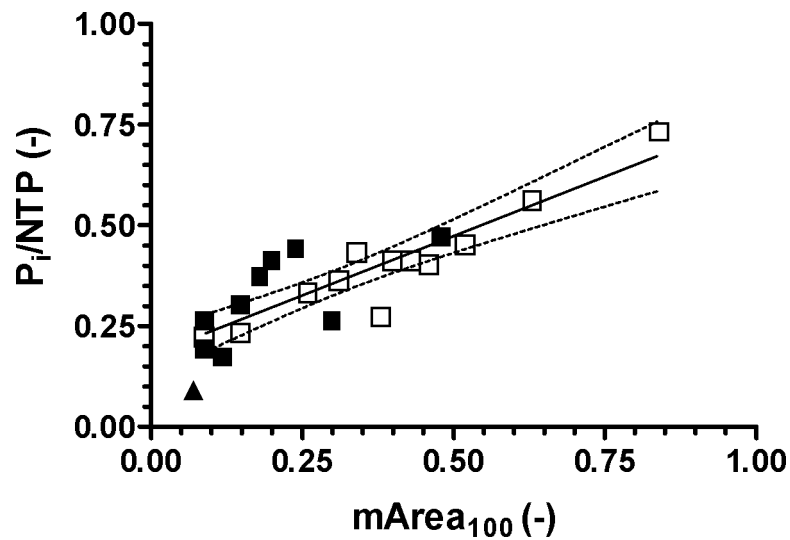
Figure 6.5 Plot of the correlation between the P_i/NTP ratio (-) and the mean area$_{100}$ (-) for the tumor lines E49 (□) and E98 (■). The line indicates the results of least-squares linear regression analyses (R^2 = 0.76) of the data for the tumor lines E49 (□), E98 (■): y = 0.17 ± 0.03 + 0.59 ± 0.07 × x. The dashed lines show the 95% confidence intervals. One square represents one tumor. The P_i/NTP ratio (▲) for the host tissue (skeletal muscle hindlimb) is 0.09 ± 0.01 and the area$_{100}$ = 0.07 ± 0.02. The datapoint of the host tissue was not used in the regression analyses.

Discussion

The relationship between the P_i/NTP ratio and the morphometric parameters.

In this study, the perfused vascular architecture of complete transverse tumor sections was analyzed by two-dimensional morphometric analyses. Two morphometric parameters were evaluated: **(a)** the percentage of large intercapillary distances and **(b)** the nonperfused area fraction. These were compared with the bioenergetic status of the whole tumor. To our knowledge this is the first study, which has related morphometric analyses of the perfused vascular architecture directly to the global bioenergetic status of the same tumor, measured by ^{31}P-MRS.

A domain analyses was used for the calculation of intercapillary distances. A domain included nonperfused vascular structures and avascular regions. Polymer infusion techniques can provide similar morphometric information about icds, but only of perfused regions (18). Morphometric analyses of only well perfused regions will probably fail to correlate with the bioenergetic status of the whole tumor, because avascular and nonperfused vascular regions will have a negative impact on the global bioenergetic status if these regions are hypoxic and are lacking nutrients.

The total bioenergetic status (P_i/NTP ratio) of a tumor depends on the balance between the oxygen supply and nutrient supply and the consumption rates of the tumor cells, which is related to the type of energy metabolism in the different tumor cells. This balance between supply and consumption determines the critical diffusion distances for oxygen and nutrients in tumor tissue. The total oxygen supply and nutrient supply depends on the tumor microcirculation and on the diffusion geometry. This study was restricted to the analyses of the relationship between the diffusion geometry of a tumor and its bioenergetic status. The P_i/NTP ratio was found to increase rapidly between a mean icd of approximately 100 μm and approximately 300 μm (Figure 6.3). This is in agreement with preliminary histological analyses of critical oxygen diffusion distances in tumor sections, using a bioreductive chemical probe for hypoxic cells (20). With use of the bioreductive chemical probe NITP (N-imidazole-theophylline, a generous gift of Dr R Hodgkiss, Gray Laboratory, England) and the perfusion marker Hoechst, hypoxic areas and perfused vessels were stained simultaneously in the same tumor section. The distances between perfused vessels and hypoxic areas varied from approximately 50 μm to approximately 150 μm, with a mean distance of 113 ± 46 μm. This correspond to a mean icd of approximately 200 μm. The complete study will be published separately. The mean critical oxygen diffusion distance of appraximately 100 μm was used as a cut off value in the definition of the morphometric parameters, i.e. the percentage of icds > 200 μm (icd_{200}) and the nonperfused area fraction at a distance > 100 μm from a nearest perfused vessel.

At a mean distance of approximately 100 μm from a perfused vessel, the probability of an aerobic to anaerobic transition is high. A main question in this study was whether this transition could influence the global bioenergetic status of a tumor? Are there sufficient tumor cells with an aerobic energy metabolism, depending on oxygen for an efficient NTP-production or may other substrates such as glucose assure the NTP-production by an intensified (an)aerobic glycolysis ?

In vitro studies on tumor cells (21, 22) and ex vivo studies on perfused tumours (23) showed the effect of a reduced oxygen supply on the oxidative phosphorylation or the inhibition of oxidative phosphorylation (24).

Pianet et al (21), Gerweck et al (22) and Eskey et al (23) found in vitro and ex vivo, that the reduction of the oxygen tension has little influence on the NTP/P_i ratio in the presence of high glucose concentrations. They argued that (an)aerobic glycolysis is capable of maintaining the energy status. In vivo (DS sarcoma), Vaupel et al (25) reported that after reduction of the tumor blood flow the amount of NTP remains nearly constant. These findings were explained by an intensified glycolysis due to the recruitment of glucose from the interstitial reservoir of the tumor. Only for tumors with a median oxygen tension below 10-15 mmHg was NTP depletion observed. These conditions were found for tumor masses larger than 1.5 % of the body weight. Okunieff et al (26) observed with ^{31}P-MRS for large tumors (murine fibro-sarcoma FSaII, approximately 2.5 % of the body weight) that i.p. injection of glucose had a positive effect on tumor energy metabolism, and no significant effect on the energy metabolism of small tumors (approximately 0.7 % of the body weight).

What can we expect in our glioma tumor model? For a given consumption rate and diffusion coefficient of oxygen and glucose, critical diffusion distances can be estimated using the Krogh model. The consumption rate of oxygen and glucose is related to the energy metabolism of cells. Histochemical evaluation of this metabolism in rat C6 gliomas (27) revealed that the energy production is more dependent on aerobic glycolysis than on oxidative phosphorylation: enzymes of the energy-producing tricarboxylic acid cycle and the electron-transport system were reduced, although still present. Rhodes et al (28) found for human gliomas in vivo, using Positron Emission Tomography (PET), a metabolic uncoupling between the regional oxygen consumption and glucose consumption. The latter is indicative of an increased aerobic glycolysis. In order to determine the importance of the mitochondrial oxidative phosphorylation vs aerobic glycolysis, the in vivo determination of the oxygen and glucose consumption is important. Mean oxygen and glucose consumption rates for macroscopic tissue volumes of human high-grade gliomas (PET derived data) were estimated to be approximately 0.5 $\mu mol.g^{-1}.min^{-1}$ for oxygen and approximately 0.5 $\mu mol.g^{-1}.min^{-1}$ for glucose (11). The mean consumption rate of oxygen and glucose was found to be equal in high-grade gliomas, which means an increased aerobic glycolytic activity and/or an increased activity of the pentose phosphate shunt for DNA synthesis (27) in comparison to normal brain tissue.

Rough estimations of the oxygen and glucose Krogh radii is possible, using mean consumption rates, mean concentrations in perfused vessels and constant diffusion coefficients (Figure 6.6). The Krogh radii are approximately 100 μm for oxygen and approximately 200 μm for glucose (7, 9-12). In vivo, a large distribution of Krogh radii will be found, depending on: (a) the distance in a perfused capillary from the inlet, because the pO_2 and the glucose concentration in a capillary decreases between the inlet and outlet; (b) further, the energy metabolism and the related consumption rates of tumor cells may be heterogeneous, i.e. cell regions with aerobic and anaerobic energy metabolism may exist. However, the mean critical oxygen diffusion distance in Figure 6.6 corresponds well to the mean distance between perfused vessels and hypoxic areas as determined by the use of the bioreductive chemical probe NITP. In addition, the percentage of icd_{200} and the mean $area_{100}$ were linearly related to the P_i/NTP ratio, whereas no relationship was found between the P_i/NTP ratio and higher or lower values than the cut off value of approximately 100 μm used in the definition of both morphometric parameters.

The results lead to the following hypothesis: the linear relationship between the P_i/NTP ratio and the morphometric parameters in Figure 6.4 and 6.5 is due to a slowly changing metabolic steady state: (aerobic) glycolysis + oxidative phosphorylation -> anaerobic glycolysis, in which the glioma cells attempt to maintain NTP synthesis by the anaerobic glycolysis during a progressively decreasing glucose supply. At an intercapillary distance of approximately 200 μm, the probability of an aerobic to anaerobic transition is high and consequently will affect the local bioenergetic status of glioma cells, which consume oxygen. The relationships found between the P_i/NTP ratio and the morphometric parameters possibly indicate that the diffusion-limited supply of oxygen is a major determinant of tissue oxygenation in our glioma tumor model.

    As a next step, in vivo and/or in vitro measurements of the oxygen consumption rates of tumor cells in human glioma xenografts, used in this study, will be performed and related to critical diffusion distances of oxygen in vivo.

Figure 6.6 Plot of the relative values of the pO_2 (%) (-△-) and [glucose] (%) (-▲-) in glioma tissue (y-axis) and their Krogh radii r (x-axis) for one perfused vessel (x = 0) calculated with use of the following parameters:**Oxygen** (9,10,12): mean pO_2 = approximately 70 mmHg (mean pO_2 vessel), mean consumption rate gliomas (11): 0.011 ml.g^{-1}.min^{-1}, radius of tissue cylinder: 0.0105 cm, Krogh's diffusion constant: 2.5 x 10^{-8} ml.cm^{-1}.min^{-1}.mmHg^{-1}. **Glucose** (7,9): mean [glucose]: approximately 5.5 x 10^{-3} mmol.ml^{-1}, mean consumption rate gliomas: 5 x 10^{-4}mmol.g^{-1}.min^{-1}, radius of tissue cylinder: 0.031 cm, diffusion coefficient: 1.2 x 10^{-4} cm^2.min^{-1}. For both calculations the mean radius of vessels is 4 μm.
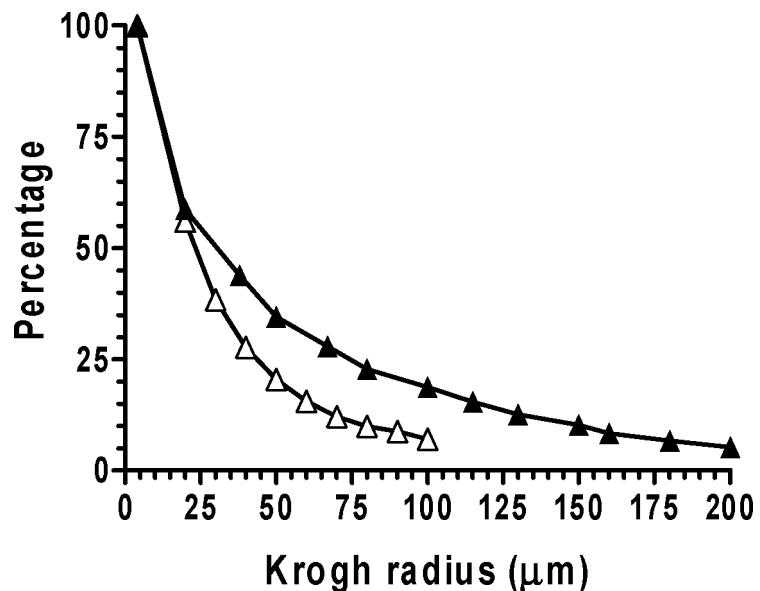
pH$_{mrs}$.

Two tumors (E49, nos 16 and 23) with 36% extracellular volume, estimated from the eosin- and haematoxylin-stained tumor sections, showed a split P_i peak. These tumors had the highest values for the percentage of icd$_{200}$ and the mean area$_{100}$. For no.16, the percentage of icd$_{200}$ = 37 and the mean area$_{100}$ = 0.63. For no.23, the percentage of icd$_{200}$ = 43 and the mean area$_{100}$ = 0.84. Stubbs et al (29) suggested that a split P_i peak is quite possible when the contribution of extracellular P_i is 35% or more. The pH across the plasma membrane would have to be > 0.3-0.4 pH units. Gerweck et al (30) showed for murine fibrosarcoma cells (FSaII) that the pH$_i$ is relatively resistant to changes in pH$_e$ above 6.9. Below a pH$_e$ of 6.9 a pH gradient is maintained with pH$_i$ being consistently more basic than pH$_e$ by ± 0.35 pH units.

The results of Gerweck et al (30) and Stubbs et al (29) agree with our findings: for tumor nos 16 and 23 the mean pH_e is 6.8 ± 0.1 and 6.7 ± 0.1 and the mean pH_i is $6.8 + 0.35 = 7.2$ and $6.7 + 0.35 = 7.1$.

No relationship was found between the pH_{mrs} and the morphometric parameters. Spatially resolved bioluminescence and fluoroscopic imaging studies of pH values in tumor tissue showed a relationship with the distribution of perfused and nonperfused areas (31), but global pH_{mrs} measurements failed in this study.

References

1. Vaupel P, Okunieff P, Kallinowski F and Neuringer LJ. Correlations between ^{31}P-NMR Spectroscopy and Tissue O_2 Tension Measurements in a Murine Fibrosarcoma. *Radiation Res* **120**: 477-493 (1989).

2. Rofstad EK, Demuth P, Fenton BM and Sutherland RM. ^{31}P Nuclear Magnetic Resonance Spectroscopy Studies of Tumor Energy Metabolism and Its Relationship to Intravessel Oxyhemoglobin Saturation Status and Tumor Hypoxia. *Cancer Res* **48**: 5440-5446 (1988).

3. Evelhoch JL, Sapareto SA, Nussbaum GH and Ackerman JJH. Correlations between ^{31}P NMR Spectroscopy and ^{15}O Perfusion Measurements in the RIF-1 Murine Tumor in-vivo. *Radiation Res* **106**: 122-131 (1986).

4. Okunieff PG, Koutcher JA, Gerweck L, McFarland E, Hitzig B, Urano M, Brady T, Neuringer L and Suit HD. Tumor Size Dependent Changes in a Murine Fibrosarcoma: Use of in-vivo ^{31}P NMR for Noninvasive Evaluation of Tumor Metabolic Status. *Int J Radiat Oncol Biol Phys* **12**: 793-799 (1986).

5. Wendland MF, Sujata BI, Karen KF, Lam KN and James TL. Correlations between in-vivo ^{31}P MRS Measurements, Tumor Size, Cell Survival, and Hypoxic Fraction in the Murine EMT6 Tumor. *Mag Res Med* **25**: 217-232 (1992).

6. Vaupel P. Microcirculation and Blood Flow: Major Determinants of Tumor Tissue Oxygenation In rHErythropoietin in Cancer Supportive Treatment, Smith JF, Boogaerts MA and Ehmer BRM (eds), pp. 206-213. Marcel Dekker: New York (1996).

7. Vaupel P. Atemgaswechsel und Glucose-stoffwechsel von Implantations-tumoren (DS-Carcinosarkom) in-vivo. *Akademie der Wissenschaften und der Literatur, Mainz* **1**: 78-97 (1974).

8. Kreuzer F. Oxygen supply to tissues: The Krogh model and its assumptions. *Experientia* **38**: 1415-1426 (1982).

9. Kallinowski F, Runkel S, Fortmeyer HP, Förster H and Vaupel P. L-Glutamine: a major substrate for tumor cells in-vivo? *J Cancer Res Clin Oncol* **113**: 209-215 (1987).

10. Groebe K and Vaupel P. Evaluation of Oxygen Diffusion Distances in Human Breast Cancer Xenografts Using Tumor-Specific In-vivo data: Role of Various Mechanisms in the Development of Tumor Hypoxia. *Int J Radiat Oncol Biol Phys* **15**: 691-697 (1988).

11. Vaupel P, Kallinowski F and Okunieff P. Blood Flow, Oxygen and Nutrient Supply, and Metabolic Microenvironment of Human Tumors: a review. *Cancer res* **49**: 6449-6465 (1989).

12. Dewhirst MW, Secomb TW, Ong ET and Gross JF. Determination of Local Oxygen Consumption Rates in Tumors. *Cancer Res* **54(13)**: 3333-3336 (1994).

13. Certaines de JD, Larsen VA, Podo F, Carpinelli G, Briot O and Henriksen O. Review paper: In-vivo ^{31}P MRS of Experimental Tumors, *NMR Biomed* **6**: 345-365 (1993).

14. Rijken PFJW, Bernsen HJJA and van der Kogel AJ. Application of an Image Analyses System to the Quantitation of Tumor Perfusion and Vascularity in Human Glioma Xenografts. *Microvascular Res* **50**: 141-153 (1995).

15. Moon RB and Richards JH. Determination of Intracellular pH by ^{31}P Magnetic Resonance. *J Biol Chem* **248**: 7276-7280 (1973).

16. Seo Y, Murahami M, Watari H, Imal LY, Yoshizaki K, Nishihawa H and Morimoto. Intracellular pH Determination by ^{31}P NMR Technique. *J Biochem* **94**: 729-733 (1983).

17. Yoshii Y and Sugiyama K. Intercapillary Distance in the Proliferating Area of Human Glioma. *Cancer Res* **48**: 2938-2941 (1988).

18. Less JR, Skalak TC, Sevick EM and Jain RK. Microvascular Architecture in a Mammary Carcinoma: Branching Patterns and Vessel Dimensions. *Cancer Res* **51**: 265-273 (1991).

19. Tozer GM and Griffiths JR. The Contribution made by Cell Death and Oxygenation to ^{31}P MRS Observations of Tumor Energy Metabolism, *NMR Biomed* **5**: 279-289 (1992).

20. Hodgkiss RJ, Jones G, Long A, Parrick J, Smith KA, Stratford MRL and Wilson GD. Flow Cytometric Evaluation of Hypoxic Cells in Solid Experimental Tumors using Fluorescence Immunodetection, *Br J Cancer* **63**: 119-125 (1991).

21. Pianet I, Merle M, Labouesse J and Canioni P. Phosphorus-31 nuclear magnetic resonance of C6 glioma cells and rat astrocytes: Evidence for a modification of the longitudinal relaxation time of NTP and P_i during glucose starvation. *Eur J Biochem* **195**: 87-95 (1991).

22. Gerweck LE, Seneviratine T and Gerweck KK. Energy Status and Radiobiological Hypoxia at Specified Oxygen Concentrations. *Radiation Res* **135**: 69-74 (1993).

23. Eskey CJ, Korestky AP, Domach MM and Jain RK. Role of oxygen vs. glucose in energy metabolism in a mammary carcinoma perfused ex vivo: Direct measurement by ^{31}P NMR. *Proc Natl Acad Sci* USA **90**: 2646-2650 (1993).

24. Loesberg C, van Rooij H, Nooijen WJ, Meijer AJ and Smets LA. Impaired Mitochondrial Respiration and Stimulated Glycolysis by m-Iodobenzylguanidine (MIBG). *Int J Cancer* **46**: 276-281 (1990).

25. Vaupel P, Kelleher DK and Engel T. Stable bioenergetic status despite substantial changes in blood flow and tissue oxygenation in a rat tumor. *Br J Cancer* **69**: 46-49 (1994).

26. Okunieff P, Vaupel P, Sedlacek R and Neuringer LJ. Evaluation of Tumor Energy Metabolism and Microvascular Blood Flow after Glucose or Mannitol Administration using ^{31}P Nuclear Magnetic Resonance Spectroscopy and Laser Doppler Flowmetry. *Int Radiat Oncol Biol Phys* **16**: 1493-1500 (1989).

27. Ikezaki K, Black KL, Conklin SG and Becker DP. Histochemical evaluation of energy metabolism in rat glioma. *Neurol. Res* **14(4)**: 289-293 (1992).

28. Rhodes CG, Wise RJ, Gibbs JM, Frackowiak RS, Hatazawa J, Palmer AJ, Thomas DG and Jones T. In-vivo disturbance of the oxidative metabolism of glucose in human cerebral gliomas. *Ann Neurol* **14(6)**: 614-626 (1983).

29. Stubbs M, Bhujwalla ZM, Tozer GM, Rodriques LM, Maxwell RJ, Morgan R, Howe FA and Griffiths JR. An Assessment of ^{31}P MRS as a Method of Measuring pH in Rat Tumors. *NMR Biomed* **5**: 351-359 (1992).

30. Gerweck LE and Fellenz MP. The Simultaneous Determination of Intracellular pH and Cell Energy Status. *Radiation Res* **125**: 257-261 (1991).

31. Hossmann KA, Linn F and Okada Y. Bioluminescence and Fluoroscopic Imaging of Tissue pH and Metabolites in Experimental Brain Tumors of Cat. *NMR Biomed* **5**: 259-264 (1992).

Chapter 7

Effect of carbogen breathing on the physiological profile of human glioma xenografts

Boudewijn P.J. van der Sanden
Arend Heerschap
Louis Hoofd
Arjan W. Simonetti
Klaas Nicolay
Annette van der Toorn
Willy N.J.M. Colier
Albert J. van der Kogel

Abstract

The aim of this study was to evaluate the effect of carbogen breathing on the physiological profile of human glioma xenografts. Near infrared spectroscopy was used to investigate changes in oxy- and deoxyhemoglobin concentrations in tumor blood. Oxygen tension changes in tumor tissue were evaluated by ^{19}F-MR relaxometry, using perfluoro-15-crown-5-ether, and modifications of tumor blood perfusion (TBP) were analyzed by fast dynamic ^{1}H-MR imaging of Gd_DTPA uptake. Finally, changes of the bioenergetic status and pH of tumor cells were analyzed by ^{31}P-MRS.

After 5 to 8 min carbogen breathing the average oxygen tension increase in tumor tissue was 4.6 ± 1.3 mmHg, which is in agreement with an increase of the oxyhemoglobin concentration in tumor blood ($\Delta[O_2Hb]$ = 9.2 ± 3 μM). However, simultaneously the TBP was reduced, the bioenergetic status was diminished and pH was decreased.

As 100 % O_2 breathing alone did not result in a detectable increase of oxyhemoglobin in tumor blood, the increase of the tumor oxygenation by carbogen appears to be mediated by its CO_2 content. This component may cause a nutrient-limited decrease of oxidative energy metabolism, indirectly via a steal-effect and/or by inhibition of the glycolytic rate resulting from tissue acidification.

Introduction

The hypoxic cell fraction in tumor tissue plays an important role in the sensitivity of a tumor to radiotherapy (1,2). The oxygen tension in tumor tissue depends on the balance between the oxygen supply and the oxygen consumption rate of the tumor cells. This balance determines the critical O_2 diffusion distances pertinent to perfused vessels in tumor tissue. Tumor regions beyond this critical distance are regarded as chronically hypoxic (3, 4). A fraction of perfused vessels may have intermittent blood perfusion. These vessels transiently open and close in such a way that hypoxic regions may appear acutely (3, 4).

Breathing of carbogen (95% O_2/5% CO_2) in combination with nicotinamide and/or perfluorocarbon compounds has been introduced to decrease the fraction of chronically - and acutely hypoxic cells. (3-5). This treatment modality has produced a drastic improvement in local control of advanced laryngeal tumors (6). Carbogen is thought to reduce chronic hypoxia by increasing the amount of dissolved oxygen in blood plasma and by saturating hemoglobin with oxygen (5, 7). This is expected to extend the tissue area supplied with oxygen by diffusion from perfused vessels and hence reduce the number of chronically hypoxic cells (3), provided that no changes occur in the tumor blood perfusion (TBP) and the O_2 consumption of tumor cells. In addition, the acidification of blood and tissue due to the CO_2-component of carbogen may cause increased systemic blood pressure and vasodilation of microvessels possessing responsive smooth musculature, which can change tumor blood perfusion (8-10). Tissue acidification may also inhibit the glycolytic rate of cells (11,12).

Although the effect of carbogen breathing on arterial blood gases appears comparable in different animal models (S. Robinson and M. Stubbs, personal communications), the effect on tumor blood perfusion and oxygenation was found to vary between different experimental and human tumors (13) and also intratumoral variations were observed (14). As tumors may contain residual normal host vessels supplied with responsive smooth musculature, the vasodilating effect of the CO_2-component on TBP may depend on the proportion of such host vessels in tumor tissue (9, 13). In addition, the vasodilating effect of the CO_2-component on TBP is also determined by the configuration of the tumor vascular bed in relation to the vasculature of host tissue (8-10). If the tumor vasculature runs in parallel to the vasculature of the host, then carbogen breathing may increase the blood perfusion in host tissue at the expense of the tumor blood perfusion; the so-called steal-effect (10). Thus, differences in tumor implantation sites and the extent of neovascularization are among the factors determining the effect of carbogen on TBP.

As the ultimate effect of carbogen breathing on tumor physiology evolves from changes in multiple processes, this effect can only be understood when all relevant factors are taken into account. Therefore, the aim of this study was to perform a comprehensive analysis of the effects of carbogen breathing on the physiological profile of human glioma xenografts.

The changes of oxyhemoglobin concentrations in tumor and arterial blood were studied using near infrared spectroscopy (NIRS) (15, 16) and blood analyses. The effect of carbogen breathing on the tumor tissue oxygenation was evaluated by ^{19}F-MR relaxometry, using perfluoro-15-crown-5-ether as oxygen sensor (17). Changes in the tumor blood perfusion were analyzed by fast dynamic [1]H-MRI studies of the gadolinium diethylenetriaminepentaacetic acid (Gd_DTPA) uptake in the extracellular volume of the tumor (18). Finally, the effect of carbogen breathing on the bioenergetic status (P_i/NTP ratio) and on the intracellular pH of tumor cells was studied by ^{31}P-MR spectroscopy (19). If carbogen breathing results in an extension of the tissue area supplied with oxygen, then the P_i/NTP ratio of tumor cells may decrease due to an enhanced oxidative energy metabolism. Changes in the intracellular pH of tumor cells (pH_{mrs}) may correlate with changes in energy metabolism (11, 12).

Material and Methods

Animal model. Human glioma xenografts (line E49) established from human tumor material were grown subcutaneously in the hindlimbs of athymic mice (Balb/c nu/nu, BonholdGard Denmark) (20). Mice were anesthetized with a flow of 2 % enflurane in an O_2/N_2O (30 % O_2) gas mixture applied through a nose cone. To study the effect of carbogen breathing the O_2/N_2O gas mixture was switched to carbogen (95% O_2/5% CO_2) or to other O_2/CO_2 gas mixtures in NIRS experiments (see below). The percentage of enflurane was kept constant during, and after the switch. The flow velocity was 1 $l.min^{-1}$ in all experiments and the composition of gas mixtures was analyzed on-line at the inlet of the nose cone with a gas monitor (Datascope Multinex, Datascope Corp. Paramus, N.J., USA). All experiments (except NIRS) were started 5 minutes after the beginning of carbogen breathing. The 5 min pre-breathing time was based on results of the NIRS experiments, which showed that after 5 min the oxyhemoglobin concentration ([O_2Hb]) and deoxyhemoglobin concentration ([HHb]) were close to a steady state. Body temperature was monitored with a rectal probe (36-gauge wire, Hewlett Packard) and maintained at 36.5° - 37° C by a warm water blanket with a feedback system.

The following experiments were done on different groups of mice. The tumor line and implantation site were the same among these groups. Therefore average changes of blood and tissue parameters per experiment on a mouse series can be compared. The tumor weights varied from 0.6 to 0.9 g in all mice studied. The local ethical committee for animal use approved the experimental procedures.

Blood gas analyses. The effect of carbogen breathing on blood gases was analyzed by cannulating the carotid artery of 5 nude mice. Three 150 μl arterial blood samples were taken at the following times: 1) before carbogen breathing, 2) 8 min - and 3) 16 min after the start of carbogen breathing. Changes in the free oxygen tension in blood (pO_{2blood}), free CO_2 tension in blood (pCO_{2blood}) and pH in blood (pH_{blood}) were analyzed with the Blood Gas Manager 1312 (Instrumentation Laboratory, USA), and the total hemoglobin concentration ([tHb]) and hemoglobin saturation (SaO_2) were measured with the CO-oximeter 482 (Instrumentation Laboratory, USA).

Near Infrared Spectroscopy. Near infrared spectroscopy is based on the oxygen-dependent absorption of near infrared light by hemoglobin (15), with different absorption characteristics for oxyhemoglobin and deoxyhemoglobin. Therefore, relative changes of the oxyhemoglobin and deoxyhemoglobin concentration in the blood volume of tissue can be followed simultaneously during e.g. carbogen breathing. This technique cannot measure absolute concentrations of both chromophores.

Fourteen mice with tumors were placed in closed tubes with an inlet near the head of the mice for the introduction of different O_2/CO_2 gas mixtures and an outlet near the mouse's tail for on-line gas analyses with a gas monitor (see above). Tumors were placed without any compression through a hole in the tube wall adjusted to the tumor diameter. The fiber optodes of the NIRS instrument (Radiometer Medical A/S, Denmark) were placed on the surface of the subcutaneous tumors with an inter-optode distance of ~ 1 cm and an angle of ~ 90° between the input- and output optode. Using this configuration the volume of tissue probed by NIRS has a banana-shaped form with a penetration depth of approximately 10 mm (21). The tumor diameters in this study varied from 10 to 12 mm; thus, only a very small percentage of the photons originated from underlying muscle tissue and overlaying skin.

If the chromophore signal intensities were in a steady state under condition of basal anaesthesia (see first paragraph animal model), then different O_2/CO_2 gas mixtures were generated on-line using a gas blending system (H. Wösthoff, Bochum, Germany). The CO_2 content of the gas mixtures was increased in steps of 1 % with 5-min intervals, and the mixture was led through the tube with a flow velocity of 1 $l.min^{-1}$. In three animals the effect of 100 % O_2 breathing on the NIRS signals was analyzed with the same flow velocity.

Data analyses. In the last minute of each time interval of 5 min, when the chromophore signal intensities were in a steady state, the mean apparent concentration changes of the chromophores (μM) were calculated (22). Absolute quantification of concentration changes per tissue volume were not possible because, the differential path length factor (DPF (-)) was not known for tumor tissue. This factor is related to the scattering properties of tissue (22). In this paper, the term concentration changes refers to apparent concentration changes and is equal to real concentration changes multiplied with the differential path length factor for tumor tissue. The sum of oxyhemoglobin concentration ([O_2Hb]) and deoxyhemoglobin concentration ([HHb]) changes is a measure of the total hemoglobin concentration changes ([tHb]) in the region seen by the optodes. At constant blood hemoglobin concentrations this will reflect total blood volume changes (22). Concentration changes were analyzed with a paired t-test.

^{19}F-MR relaxometry. In vivo ^{19}F-MR relaxometry measurements were performed on 13 tumors using an SMIS spectrometer interfaced to a vertical bore magnet (4.3 T) and employing a home-built ^{1}H/^{19}F double tunable solenoid ($\varnothing$ 13 mm). A detailed description of this method is given in ref. 23 and chapter 5. Briefly, 3 or 4 days before the NMR experiments 0.15 ml of the 40% (v/v) perfluoro-15-crown-5-ether emulsion (HemaGen/PFC, St. Louis, MO) was injected via a tail vein (dose: 4.2 g/kg).

For the appropriate positioning of a coronal slice for slice-selective ^{19}F-MR relaxometry measurements through the center of the tumor, multi-slice coronal ^{1}H-Spin Echo (SE) images were acquired (TR = 1 s, TE = 0.06 s, NS = 2, matrix size = 128 x 128, FOV 15 x 15 mm, slice thickness 1.5 mm). Next, ^{19}F-SE density images were obtained at the same position as the ^{1}H-SE images using the following parameters: TR = 8 s, TE = 0.03 s, NS = 2, matrix size = 64 x 64, FOV = 15 x 15 mm and slice thickness 4 mm. The ^{19}F-SE density images were used for analyses of the 2D distribution of PFCs in similar slices as used in in vivo ^{19}F-MR relaxometry studies.

In vivo ^{19}F-MR relaxometry was performed using a slice-selective inversion-recovery T_1-sequence with a 180° adiabatic full passage inversion pulse (24) and a 90°sinc excitation pulse, optimized for a 4 mm thick slice. Eight inversion delay times were used between 0.8 and 8 s, TR = 12 s, NS = 4, total measurement time 384 s. Two T_1 measurements were performed before carbogen breathing and subsequently two during carbogen breathing.

Data analyses. An in-vitro calibration curve (see chapter 5 and ref. 23) was used to convert in vivo T_1-relaxation rates (R_1) of ^{19}F-spins to $pO_{2/tissue}$ values. The standard errors of the intercept value and the slope of the calibration curve were propagated in the calculations of the SEM of absolute mean $pO_{2/tissue}$ values per tumor slice in experiments without carbogen breathing (n = 2) or were propagated in calculations of the SE of changes in the $pO_{2/tissue}$ values after 8 and 14 min carbogen breathing. For carbogen breathing experiments the average $pO_{2/tissue}$ changes of all tumors (n = 13) was analyzed with a paired t-test.

Fast dynamic ^{1}H-MRI studies of Gd_DTPA uptake. Cannulae (Neoflon $\emptyset$ 0.6/19mm, 24 G) were inserted in tail veins of 8 mice with tumors for on-line administration of tracer. ^{1}H-MRI measurements were performed on a SISCO 200/400 spectrometer interfaced to a horizontal bore magnet (4.7 T). A home-built inductively coupled ^{1}H-surface coil ($\emptyset$ 3 cm) was used as transmitter and receiver. Global shimming was performed on the total tumor. For the position of a coronal slice through the center of the tumor parallel to the surface coil, multi-slice sagittal and coronal ^{1}H-SE-images were made (TR = 0.3 s, TE = 0.023 s, matrix size 256 x 64, FOV 5 x 5 cm, slice thickness = 1.5 mm). After positioning of the coronal slice, a fast RF-spoiled T_1-weighted FLASH sequence was used to obtain sensitivity to T_1-relaxation time changes of water protons induced by the Gd_DTPA uptake in the extracellular space of tumor tissue. The uptake of Gd_DTPA causes a decrease of the T_1-relaxation time of ^{1}H spins of water in tumor tissue and consequently increases the signal intensity in T_1-weighted ^{1}H-MR FLASH images. It should be noted that the O_2-component of carbogen can have a similar effect on the signal intensities in T_1-weighted ^{1}H-MR images, but we observed that the maximum decrease of T_1-relaxation times was 6 % in the presence of carbogen. This decrease was much smaller than the T_1-relaxation time decrease in the presence of Gd_DTPA at a dose of 0.1 mmol.kg^{-1}, which was approximately 38 %.

A Gd_DTPA-uptake experiment consisted of 60 consecutive T_1-weighted FLASH images with a total acquisition time of 50 s. An i.v. bolus injection (0.2 ml, duration: 2 s, 0.1 mmol.kg^1) of a Gd_DTPA solution in saline (Schering, Berlin, Germany) was given after 7 precontrast images. The rate of bolus injection was constant for all experiments. After 4 images the precontrast signal intensity was in a steady state. The Gd_DTPA uptake has only been analyzed during 42 s after bolus administration, because the [Gd_DTPA] in the extracellular volume of the tumor region of interest decreases 1 min after bolus administration due to the Gd_DTPA clearance from the blood compartment (25). The acquisition parameters for the RF-spoiled T_1-weighted FLASH were TR= 13 ms, TE= 4 ms, flip angle= 5°, matrix size= 64 x 64, FOV= 4 x 4 cm and slice thickness= 1.5 mm.

The experiments with carbogen breathing were carried out as follows: the series was started with a Gd_DTPA uptake experiment without carbogen breathing; the second Gd_DTPA uptake experiment was started 2 h later to allow clearance of the first Gd_DTPA dose. After 2 h the signal intensity in T_1-weighted FLASH images was similar to the 7th precontrast image of the first Gd_DTPA-uptake experiment. In the second experiment carbogen breathing was started 5 min before the second bolus contrast injection. For 3 mice the set of experiments was repeated without carbogen breathing in order to test the reproducibility of the Gd_DTPA uptake under identical experimental conditions.

Data analyses. In 60 consecutive T_1-weighted FLASH images ^{1}H-signal intensity changes were analyzed using ImageBrowser software (version 1.0, Spectroscopy Imaging Systems, CA, USA). Before the analyses per Gd_DTPA-uptake experiment the 7th precontrast FLASH image was subtracted from all images. For different regions of interest (ROI) in perfused tumor areas the mean signal intensity changes (postcontrast - precontrast signal intensity) were calculated in all 60 consecutive subtracted FLASH images and normalized to the maximum intensity change (100 %) in the series. Each ROI contains several pixels with different signal intensity changes; the standard deviation, as shown in Figure 7.3B-C, is taken as an indicator of the variation of pixel signal intensity changes per ROI. In the ROIs the pixels containing the skin as identified in ^{1}H-SE images were left out. For the given doses the signal intensity increase in subtracted T_1-weighted FLASH images was linearly related to [Gd_DTPA] (26, 27).

^{31}P-MRS. The effects of carbogen breathing on the P_i/NTP ratio and pH_{mrs} were measured by ^{31}P-MRS in 5 mice with tumors and in muscle tissue of the hindlimb of 3 mice. These measurements were performed on a Bruker spectrometer interfaced to a vertical bore magnet (4.7 T) employing a home-built ^{1}H/^{31}P double tunable 3 turn solenoid coil with an inner diameter of 13 mm. The solenoid coil was fitted with a Faraday shield to eliminate spurious signals from normal tissue adjacent to the tumor. It should be noted that the P_i/NTP ratio reflects the average bioenergetic status of the tumor cells and the pH_{mrs} is an approximate measure of the average intracellular pH in a volume sampled by the solenoid (= approximate tumor volume). ^{31}P-MRS spectra were obtained with a one-pulse sequence with a hard pulse of ~12 μs (optimized for maximum signal intensity), TR = 3 s, NS = 320. The total acquisition time per ^{31}P-MRS experiment was 16 min. One ^{31}P-MRS experiment was completed before carbogen breathing was initiated, and 2 consecutive experiments were performed 5 min after the start of carbogen breathing.

Respiration of 100 % oxygen for 30 min reduced the T_1-relaxation time of the inorganic phosphate (P_i) from ~ 4 s to ~ 3 s in tumors (28). With a pulse repetition time of 3 s and in the absence of carbogen (T_1 of P_i ~ 4 s) the magnetization in the x-y plane has the following steady state value (29):

$$M_{xy\ saturated} = 0.53 * M_0 (= (1\text{-exp}^{(-TR/T1)}) * \text{equilibrium z magnetization}).$$

In the presence of carbogen (95 % O_2) the extent of saturation decreases, because the T_1-relaxation time decreases by approximately 1 s (see above): $M_{xy\ saturated} = 0.63 * M_0$. No further effects of carbogen on the T_1-relaxation times of NTP resonances were reported: thus, changes in the P_i/NTP ratio larger than about 119 % ({0.63 * M_0/0.53 * M_0} * 100) were related to changes in the bioenergetic status of tumor tissue.

Data analyses. Zero filling and the convolution difference technique with line broadenings of 30 and 1000 Hz were applied to the free induction decay. The peaks were fitted to Lorentzian line shapes with NMR1 software (New Methods Research, Inc., Syracuse, NY, USA). Per tumor the integral of the P_i peak was divided by the sum of the α -, β - and γ-NTP peak integrals. P_i/NTP ratio changes ($\Delta(P_i/NTP)$) after the start of carbogen breathing were related to the P_i/NTP ratio without carbogen breathing (100 %). The mean P_i/NTP ratio changes of 5 tumors or 3 muscle tissues were analyzed with a paired t-test. The pH as measured with ^{31}P-MRS (pH_{mrs} ~ intracellular pH) was deduced from the chemical shift of the P_i signal with respect to the chemical shift of the phosphocreatine (PCr) signal or the α-NTP signal in the absence of a PCr resonance. A modified Henderson-Hasselbach equation was used with the following parameters for tumors: pK = 6.75, a(acid shift) = 3.29, b(base shift) = 5.7 (30, 31). For muscle tissue the parameters were as follows: pK = 6.75, a(acid shift) = 3.26, b(base shift) = 5.75. Changes of the pH_{mrs} in comparison with baseline values were analysed with a paired t-test.

Results

Blood gas analyses of arterial blood samples before and after carbogen breathing.

Results of arterial blood gas analyses sampled before and 8 & 16 min after carbogen breathing are shown in Table 7.1. The normal pH value of whole blood (pH_{blood}) in unanesthetized mice was 7.4 and is related to a pCO_{2blood} value of ~ 40 mmHg as estimated from in vivo carbon dioxide dissociation curves for mammals (32, 33). The pH_{blood} and pCO_{2blood} values of anesthetized mice were 7.2 and 56 mmHg, respectively (see Table 7.1). The observed increase of the pCO_{2blood} is compatible with the pH_{blood} decrease as expected from the in vivo carbon dioxide dissociation curves. Carbogen breathing caused an additional pH_{blood} shift of -0.05 corresponding to a ΔpCO_{2blood} of 16 mmHg (see Table 7.1). Next, carbogen breathing resulted in a 6.6 % increase of the hemoglobin saturation in arterial blood (SaO_2). The average increase of dissolved oxygen in blood plasma (ΔpO_{2blood}) was 347 mmHg.

Table 7.1 Results of arterial blood gas analyses (n = 5). Values are means ± SEM (Relative to baseline). The mean total hemoglobin concentration [tHb] of all blood samples was 10.4 ± 0.2 mM (= monomeric concentration) or 2.6 mM (= tetrameric concentration).

Base line[a]	8 min carbogen[b]	16 min carbogen[b]
pH_{blood} = 7.21 ± 0.04	ΔpH_{blood} = - 0.05 ± 0.004	ΔpH_{blood} = - 0.05 ± 0.009
pCO_{2blood} = 56.4 ± 2.5 mmHg	ΔpCO_{2blood} = 16 ± 1.8 mmHg	ΔpCO_{2blood} = 16 ± 0.9 mmHg
SaO_2[c] = 94 ± 1.8 %	SaO_2 increase = 6.6 ± 0.7 %	SaO_2 increase = 6.6 ± 0.7 %
pO_{2blood}[d] = 131 ± 7.2 mmHg	ΔpO_{2blood} = 338 ± 47 mmHg	ΔpO_{2blood} = 356 ± 49 mmHg

a) Anaesthesia: 2 % enflurane, 25 % O_2, 73 % N_2O
b) Anaesthesia + carbogen breathing: 2 % enflurane, 94 % O_2, 4 % CO_2.
c) SaO_2 = Hemoglobin (Hb) saturation (%).
d) pO_{2blood} = Blood oxygen tension (mmHg).

Near infrared spectroscopy (NIRS) studies of concentration changes of oxy- and deoxyhemoglobin in tumor blood during breathing of different CO_2/O_2 gas mixtures.

Changes of the absorption characteristics of the oxygen-dependent chromophores in approximately the whole tumor blood volume of 14 mice have been observed with NIRS during 25 min. Figure 7.1 shows mean concentration changes (μM) of oxyhemoglobin (O_2Hb), deoxyhemoglobin (HHb) and the total hemoglobin (tHb). The CO_2 content of the O_2/CO_2 gas mixture was increased in steps of 1 % with 5 min intervals. The mean concentration of O_2Hb and HHb changed immediately after breathing the 99% O_2 / 1% CO_2 mixture. The total hemoglobin concentration remained constant (p > 0.05), but the mean O_2Hb and HHb concentration changes in blood were highly significant (p < 0.001) for all gas mixtures in comparison with control experiments. The maximum change in the mean [O_2Hb] and [HHb] was obtained at a gas mixture with 4 % CO_2: 46.3 ± 6.5 (SEM) μM and -34.9 ± 2.7 (SEM) μM, respectively. However, during the increase of the CO_2 content from 1 % to 5 %, the maximum change of the mean concentration was only significant for HHb (p < 0.02) and was not significant for O_2Hb (p > 0.05) in comparison with the 99% O_2 / 1% CO_2 mixture.
Further, no significant changes of the [O_2Hb] and [HHb] were observed in 3 human glioma xenografts during breathing of 100 % O_2 (results not shown here).
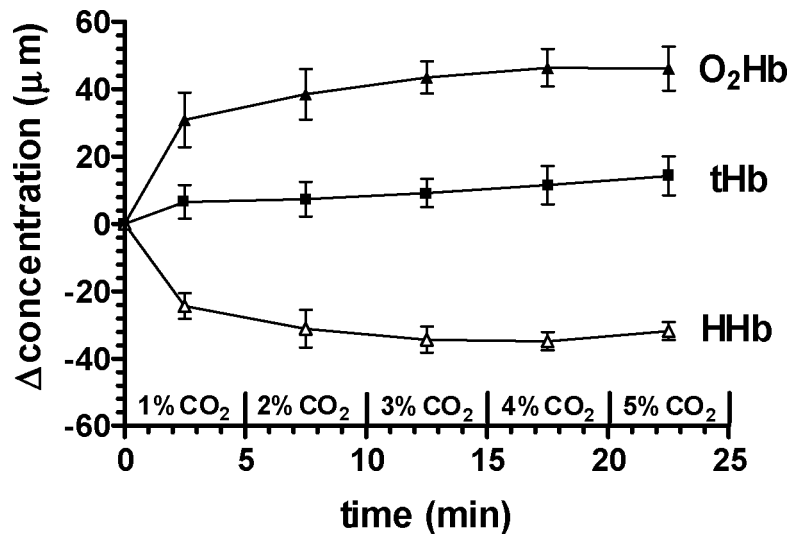
Figure 7.1 Mean concentration changes (μM) ± SEM of oxygen-dependent chromophores in approximately the whole blood volume of 14 E49 tumors, as measured by near infrared spectroscopy, are shown when the CO_2 content of the O_2/CO_2 gas mixtures was increased in steps of 1 % with 5 min intervals.

^{19}F-MR relaxometry studies of the oxygen tension changes in tumor tissue during carbogen breathing.

For the interpretation of the in vivo ^{19}F-MR relaxometry studies analyses of the PFC distribution within tumor slices is crucial. Figure 7.2A shows an example of a ^{19}F-SE density image through the center of a representative tumor at the same location as the slice of the ^{19}F-MR relaxometry measurement (see also Figure 5.1). In this image the distribution of PFCs was heterogeneous. In chapter 5 we observed spatial correlations between the perfused microvessel distribution and the PFC distribution in tumor tissue slices (23). In this chapter, the PFC distribution also appeared comparable with the Gd_DTPA distribution, see next paragraph. In all tumors, the PFC's became sequestered in the perfused periphery of the tumor. Furthermore, $pO_{2tissue}$ values as probed with Eppendorf O_2-electrodes in the perfused periphery of the tumor corresponded to $pO_{2tissue}$ measured with^{19}F-MR relaxometry. The $pO_{2tissue}$ values in necrotic regions as measured with Eppendorf O_2-electrodes were much lower than the $pO_{2tissue}$ values observed with ^{19}F-MR relaxometry. The latter indicates that PFC's preferentially accumulate in perfused regions of the tumor, and not in necrotic regions of the tumor. Thus, slice-selective ^{19}F-MR measurements probe average $pO_{2/tissue}$ values or changes in the average $pO_{2/tissue}$ in perfused regions of the tumor throughout the whole MR-slice.

In the absence of carbogen absolute $pO_{2/tissue}$ values varied from 0.32 ± 0.7 mmHg to 8.7 ± 2.7 mmHg (Chapter 5 and ref. 23). The changes of $pO_{2/tissue}$ relative to baseline ($\Delta pO_{2/tissue}$, mmHg) in slices through the center of 13 tumors after 8 min carbogen breathing are shown in Figure 7.2B (see also Table 5.1). The effect of carbogen showed large variations: the $\Delta pO_{2/tissue}$ varied from approximately 0 to 15 mmHg. After 8 min of carbogen breathing the mean $\Delta pO_{2/tissue}$ relative to baseline was 4.6 ± 1.3 mmHg (p < 0.01), and after 14 min carbogen breathing, the mean $\Delta pO_{2/tissue}$

relative to basline was 1.7 ± 0.8 mmHg ($p < 0.05$). The mean $\Delta pO_{2/tissue}$ tended to decrease with time, but the difference between the mean $\Delta pO_{2/tissue}$ values was not significant ($p > 0.05$).
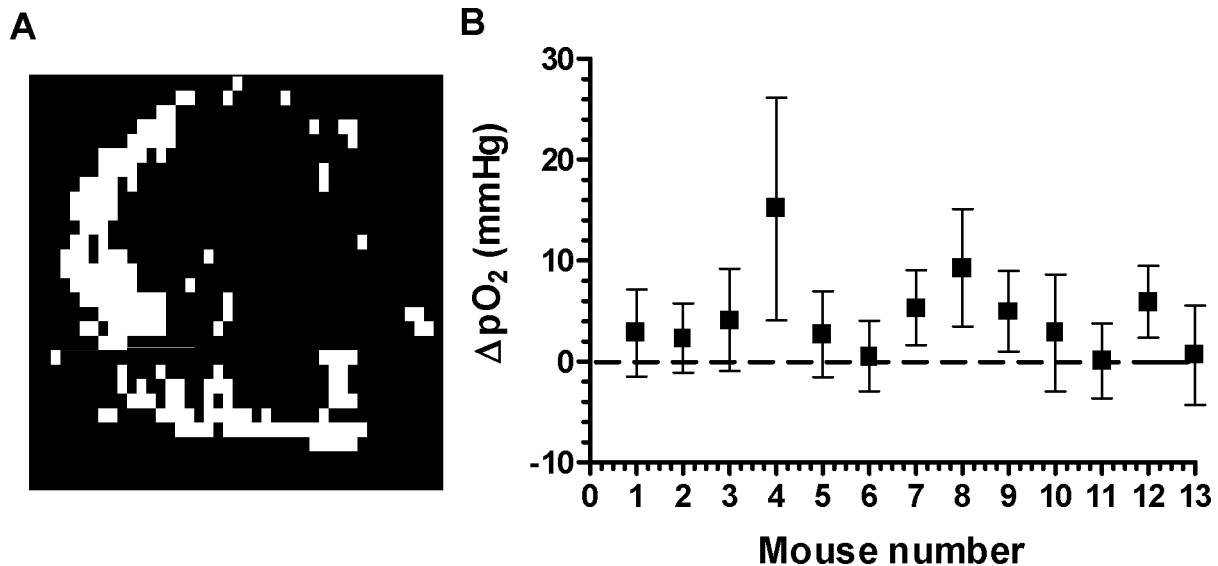
Figure 7.2 The PFC distribution in a ^{19}F-SE density image of a slice through the center of a representative tumor is shown in **Fig. 7.2A**. In **Figure 7.2B**, changes of the oxygen tension ± SE ($\Delta pO_{2/tissue}$, mmHg) after 8 min carbogen breathing in slices through the centers of 11 E49 tumors are shown. The numbers on the x-axis indicates individual mice.

Fast dynamic ^{1}H-MRI studies of the Gd_DTPA uptake in perfused tumor regions in the absence and presence of carbogen.

The ^{1}H-signal intensity in T_1-weighted FLASH images increases when the T_1-relaxation time of tissue water protons decreases due to the Gd_DTPA uptake in the extracellular space of perfused tumor regions. In all T_1-weighted FLASH images of tumor tissue slices an increase of the ^{1}H-signal intensity, or Gd_DTPA uptake, was observed in the well perfused periphery, but no changes were observed in the center during 42 s after bolus injection. Figure 7.3A shows a subtracted T_1-weighted FLASH image (Signal Intensity$_{postcontrast}$ - Signal Intensity$_{precontrast}$) of a slice through the center of a representative tumor 42 s after bolus injection of a Gd_DTPA solution in saline. In 5 mice two Gd_DTPA-uptake experiments were done: one without and another with carbogen breathing. The latter breathing condition was assessed two hours later to allow for Gd_DTPA clearance. For the regions of interest (ROIs) delineated in Figure 7.3A the mean relative signal intensity changes (mean ΔSI (%)) are shown in Figures 7.3B-C for both experiments. In all tumors the Gd_DTPA-uptake rate decreases in the perfused rim during carbogen breathing.

In subtracted T_1-weighted FLASH images obtained 42 s after bolus injection in the presence of carbogen no detectable change of the perfused areas was observed in comparison with the same images without carbogen breathing. This was in agreement with the NIRS experiments where no significant change of the [tHb] was detected. Both observations indicate that the blood fraction in the volume of interest was not increased significantly due to carbogen breathing.

In 3 tumors the reproducibility of the Gd_DTPA-uptake experiments was tested. The bolus injection of a Gd_DTPA solution in saline was repeated after a time interval of 2 h in the absence of carbogen. The mean signal intensity changes in different regions of interest were

highly reproducible in all tumors (results not shown). The signal intensity changes in the second experiment were all within the range of signal intensity changes of the first experiment ± 1.5 SD.

A

B

C
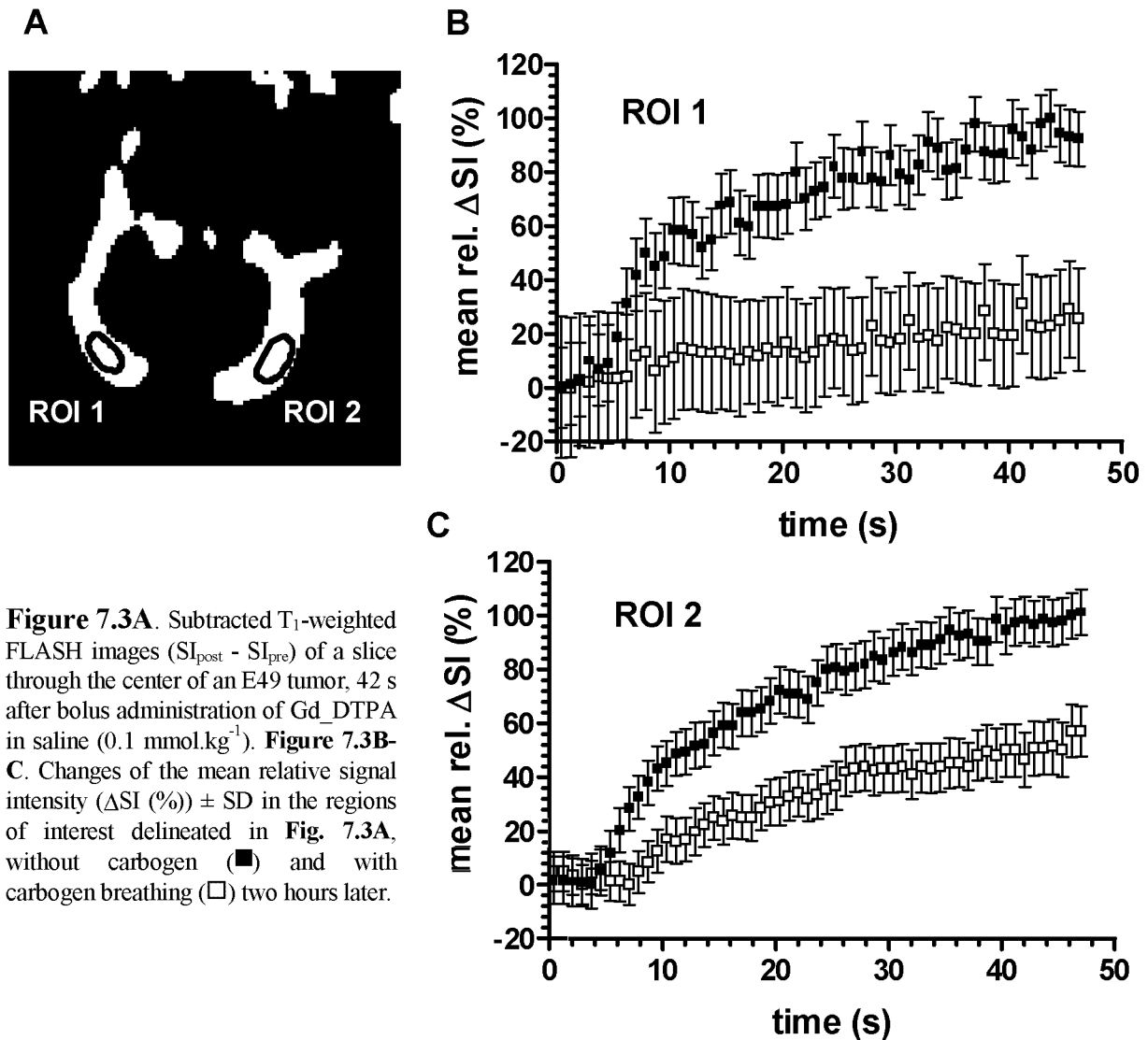
Figure 7.3A. Subtracted T_1-weighted FLASH images (SI_{post} - SI_{pre}) of a slice through the center of an E49 tumor, 42 s after bolus administration of Gd_DTPA in saline (0.1 mmol.kg^{-1}). **Figure 7.3B-C.** Changes of the mean relative signal intensity (ΔSI (%)) ± SD in the regions of interest delineated in **Fig. 7.3A**, without carbogen (■) and with carbogen breathing (□) two hours later.

^{31}P-MRS studies of changes in the bioenergetic status and pHmrs of tumor tissue during carbogen breathing.

^{31}P-MR spectra of whole tumor volume were obtained without carbogen, 13 min and 29 min after initiation of carbogen breathing (Figure 7.4). The NTP and PCr peaks decreased and the P_i peak increased during carbogen breathing. Figure 7.5 shows mean P_i/NTP ratio changes (%) of 5 tumors as a function of time (min) in comparison with baseline P_i/NTP ratios (100 %). P_i/NTP ratios started to increase and became significantly different from baseline values after 13-min carbogen breathing (see p-values in the legend of Fig. 7.5). Simultaneous with the increase of the P_i/NTP ratio, the pHmrs decreases significantly after 13 and 29 min carbogen breathing (see second y-axis of Fig. 7.5). In muscle tissue of the hindlimb (n = 3) no significant P_i/NTP ratio

changes were observed (p > 0.1) for both time points. After 13 and 29 min carbogen breathing the mean $\Delta(P_i/NTP)$ of all experiments was 108 ± 5.7 %. The pH_{mrs} decreased significantly after 29 min carbogen breathing: the mean change of the pH_{mrs} was - 0.14 $\pm$ 0.03 in muscle tissue.
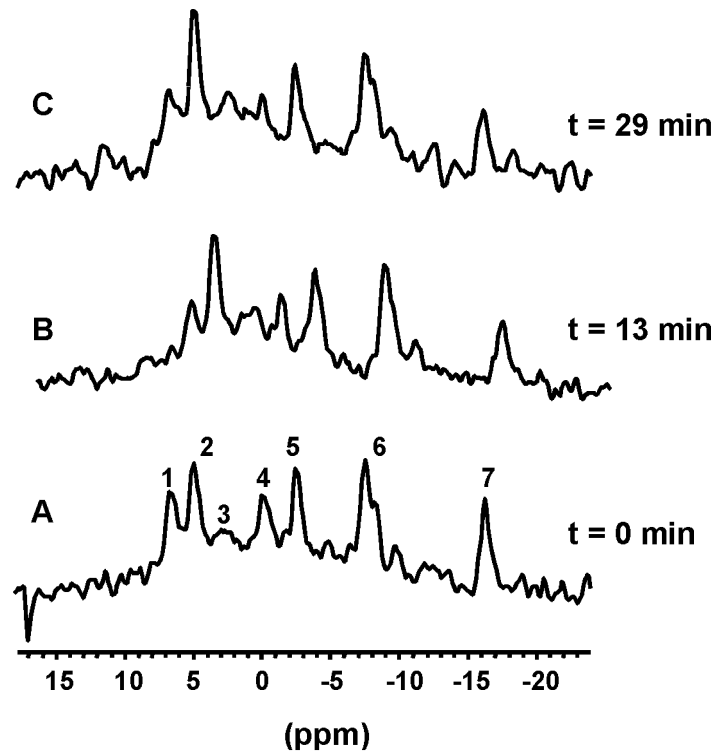
Figure 7.4 ^{31}P-MR spectra of an E49 tumor without carbogen: t = 0 (**Fig. 7.4A**), and during carbogen breathing at t = 13 min (**Fig. 7.4B**) and 29 min (**Fig. 7.4C**). Peak assignments of ^{31}P-MR spectra: 1. Phosphomonoesters, 2. P_i, 3. Phosphodiesters, 4. PCr, 5. γ-phosphate of NTP, 6. α -phosphate of NTP, 7. β-phosphate of NTP. NTP refers to the following nucleoside triphosphates: adenosine -, guanosine -, uridine - and cytidine-triphosphate. ^{31}P-MRS cannot distinguish these nucleoside phosphates, because the phosphates groupes are all equivalent. The NTP peaks are predominantly the three phosphorus nuclei of ATP with smaller contributions from the others (49).
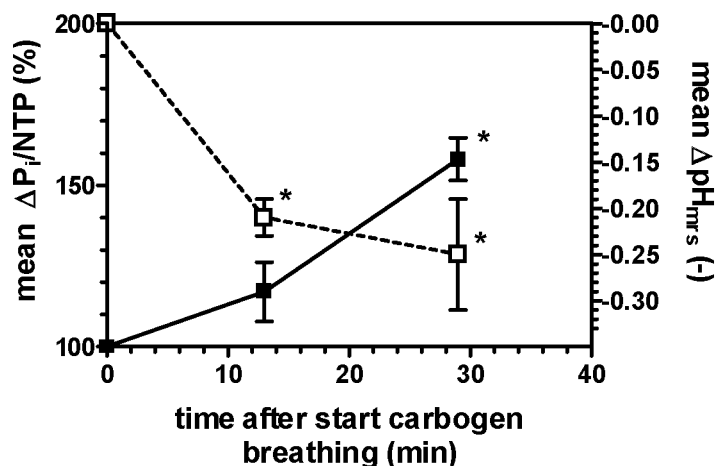
Figure 7.5 Changes of the mean P_i/NTP ratio in percentage $\pm$ SEM (%) (■) and mean pH_{mrs} $\pm$ SEM (□) in 5 mice during carbogen breathing at t = 13 min and t = 29 min. The significant changes are indicated with an asterics. The p-values (paired t-test) are: t = 13 min, Δ (P_i/NTP) : p > 0.1, Δ pH_{mrs}: p < 0.01, t = 29 min, Δ (P_i/NTP) : p < 0.01, Δ pH_{mrs}: p < 0.05.

Discussion

In this study a set of complementary noninvasive monitoring techniques have been used to probe the effects of carbogen breathing on the physiological profile of human glioma xenografts. The different methods were not used in sequence on the same individual tumor; however, experimental conditions, size and implantation site did not vary significantly among the different series. Therefore, average changes of physiological parameters in different tumors per series of experiments can be compared.

After carbogen breathing the oxygenation status of different blood and tissue compartments was ameliorated. Arterial blood gas analyses showed an increase of the hemoglobin saturation and the blood O_2 tension during carbogen breathing. The increase of the arterial hemoglobin saturation is in agreement with NIRS measurements, which showed a significant increase of the mean $[O_2Hb]$ and simultaneously a decrease of the mean $[HHb]$ in tumor blood for a range of different O_2/CO_2 mixtures. It should be noted that both methods measure different blood quantities: besides changes of the $[O_2Hb]$ in arterial blood, NIRS also detects modifications of the $[O_2Hb]$ in capillaries and venous blood (35). In other studies comparable effects of carbogen breathing on the oxyhemoglobin concentration of tumor blood have been observed. Using functional MR-imaging Robinson et al (13, 36) and Howe et al (37) reported large signal intensity increases in GH3 prolactinomas grown in the flank of rats after 5 min carbogen breathing. A part of the signal intensity increase in tumor regions was attributed to an increase of the $[O_2Hb]$. Further Fenton (5) observed cryo-spectrophotometrically in sarcoma and in squamous cell carcinoma xenografts an increase of the hemoglobin saturation in perfused tumor capillaries after 7-min carbogen breathing. In the present NIRS study a CO_2 content of 4 % in the breathing gas mixture seemed to be sufficient for a maximum effect on the mean $[O_2Hb]$. This CO_2 content is lower than the 5 % CO_2 content of carbogen, which has been used as a standard mixture in other experimental and clinical studies (3-6, 13, 14).

When hemoglobin became completely saturated during carbogen breathing, the pO_2 in arterial blood increased significantly. In oxygen-dependent phosphorescence quenching studies Torres Filho et al (38) found in blood vessels of human colon adenocarcinoma (grown in dorsal skin chambers) and in arterioles of subcutaneous tissue a pO_{2blood} increase of ~ 150 % after carbogen breathing in comparison with baseline values in anesthetized mice. This is comparable to the increase of pO_{2blood} observed in the present study. Furthermore, Cerniglia et al (39) showed with a similar technique an increase of the intravascular oxygen tension during carbogen breathing in subcutaneous 9L-Glioma tumors. The pO_{2blood} increase varied among tumors and was greater with carbogen compared with 100 % oxygen. This is comparable to the results of the present NIRS studies where no detectable changes of the $[O_2Hb]$ in tumor blood were observed during breathing of 100 % O_2. Breathing of a CO_2/O_2 gas mixture seems a more effective way of increasing the $[O_2Hb]$ and the pO_{2blood} than breathing of 100 % O_2.

Simultaneous to the increase of the $[O_2Hb]$ and pO_{2blood}, the $pO_{2/tissue}$ as measured by ^{19}F-MR relaxometry increased significantly. It should be noted that the PFCs became sequestered in well-perfused regions of the tumor; thus, $pO_{2/tissue}$ changes were mainly observed in these regions (Chapter 5 and ref. 23). The oxygen tension in tissue depends on the balance between the O_2 supply and O_2-consumption rates of tumor cells; thus, a $pO_{2/tissue}$ increase can be due to an increase of the O_2 supply, but may also be due to a decrease of O_2-consumption rates. Given the fact that breathing of 100 % oxygen did not cause a significant increase of the $[O_2Hb]$, but a gas mixture of CO_2 and O_2 did, the CO_2-component of carbogen may affect the $pO_{2/tissue}$ via modifications of the O_2-consumption rates of tumor cells. A decline of the O_2-consumption rate of cells may also result in an increase of the $pO_{2/tissue}$ and $[O_2Hb]$ in capillaries

and venous blood.

The CO_2-component of carbogen increased the CO_2 blood tension (pCO$_{2blood}$), which resulted in a drop of pH$_{blood}$ and pH$_{mrs}$. During carbogen breathing a significant decrease of the Gd_DTPA-uptake rate in the extracellular space of perfused tumor regions was measured in all tumors studied. This uptake rate depends on tumor blood perfusion (TBP) in the perfused tumor microvessels, the permeability surface area (PS-product) of these vessels and the tracer distribution volume (40, 41). Can the observed acidification of tumor blood and tissue affect one of these parameters in such a way that the Gd_DTPA-uptake rate in perfused tumor regions decreases? Carbogen breathing is not expected to have any effect on the tracer distribution volume, which is a part of the extracellular volume in the region of interest containing perfused vessels. Furthermore, it is unlikely that the permeability of the tumor vessels altered by carbogen breathing. However, the CO_2-component of carbogen has a vasodilating effect on vessels possessing responsive smooth musculature (13, 36); thus, carbogen may increase the surface area of perfused vessels (S). An increase in the surface area might result in a larger PS-product and thus in an increase of the Gd_DTPA uptake (41), but this was not observed in perfused tumor regions. Moreover, no detectable increase in perfused tumor areas was observed in subtracted T_1-weighted FLASH images during carbogen breathing, which is in agreement with the results of the NIRS experiments, where no significant increase was observed in the [tHb] (~ blood volume). This probably means that populations of constricted tumor vessels, if present, are not strongly dilated by carbogen. In studies reported by Torress Filho et al (38) and Dewhirst et al (42) no important changes were observed in the mean tumor vessel diameter during carbogen breathing. The most plausible explanation for the decreased Gd_DTPA uptake in perfused tumor regions is a decreased blood perfusion. The tumor vasculature of subcutaneously or intramuscularly implanted rodent tumors in flank or hindlimb is mostly parallel to the host tissue vasculature (8). Vasodilator agents such as hydralazine and nitroglycerin were found to decrease the blood perfusion in such rodent tumors as measured by ^{1}H-MRI studies of the Gd_DTPA uptake (18, 43) and by laser Doppler flow studies (10). Simultaneously hydralazine was found to increase blood perfusion in muscle tissue (18, 43). The CO_2-component of carbogen has a similar effect as the vasodilatory agents. A drop in pHblood and pHtissue mediates the vasodilating effect of this component on normal host vessels with responsive smooth muscle. The mode of action of these vasodilators is often referred to as the steal effect because, by dilating normal reactive vasculature, a drop in blood pressure will cause a lower blood flow through vessels which are in parallel to the host vascular bed and lack the contractile capability such as most tumor vessels (8-10).

Simultaneous to the decline of the TBP the P$_i$/NTP ratios of all tumors were found to increase. This increase was not significant during the first 13 min, in agreement with studies by Koutcher et al (44) and Howe et al (47), but became significant after 13-min carbogen breathing. Although, the effect of carbogen on TBP was only analyzed in the last 42 s of a 6 min carbogen breathing period, the constant increase of the P$_i$/NTP ratio during a breathing period of 29 min suggests that the reduction of TBP is a more permanent effect of carbogen breathing. The reduction of the TBP (steal effect) may result in a decreased supply of substrates for energy metabolism in tumor cells, which leads to a decrease of the bioenergetic status of the whole tumor as expressed by an increase of the P$_i$/NTP ratio. In muscle tissue a decrease of the P$_i$/NTP ratio or improvement of the bioenergetic status due to an increased blood perfusion was not observed, because the blood perfusion was already adequate for the supply of substrates and O_2. We speculate that tumor cells with an oxidative energy metabolism will consume less O_2 when the supply of substrates such as glucose decreases. Consequently, in regions with oxygen consuming glioma cells the pO$_{2/tissue}$ and [O$_2$Hb] in mainly venous blood may increase.

In preliminary immunohistochemical studies we detected hypoxic regions at distances of approximately 100 µm from perfused capillaries, which indicates that populations of glioma cells in our tumor model consume oxygen (19, 45, 46). If tumor cells do not consume oxygen, then equilibrium between the oxygen tensions in blood and tissue will appear, and no hypoxic cells would be detectable.

Apart from a nutrient-limited decrease of oxidative energy metabolism in tumor cells, the reduction of the O_2-consumption rate of tumor cells may also be due to another mechanism. Simultaneous to the increase of the P_i/NTP ratio the pH_{mrs} decreases significantly. This acidification of the tumor may inhibit the glycolytic rate (11, 12) and can contribute to a decrease of O_2-consumption rates of tumor cells with an oxidative energy metabolism, which may increase the P_i/NTP ratio. In addition, this acidification may also have an effect on the oxygen affinity of hemoglobin (Bohr effect); a lowering of the pH in blood and tissue shifts the blood oxygen dissociation to the right, so that the oxygen affinity is decreased, which favours oxygen unloading in tissue (47). In contrast, the $[O_2Hb]$ in tumor blood actually increased, indicating that the effect of the CO_2-component on O_2-consumption rates of tumor cells is more important.

Preliminary immunohistochemical analyses of the effect of carbogen on human larynx carcinoma xenografts transplanted in the same mice and location as the human glioma xenografts in the present study showed a strong decrease of hypoxic regions in whole tumor sections. Simultaneously, a significant decrease of perfused vessels and proliferating cells was observed (48). These results are in agreement with the decrease of TBP, bioenergetic status and simultaneous increase of the tumor tissue oxygenation observed in the present study.

Conclusions. The observation that oxyhemoglobin concentration in tumor blood and oxygen tensions in arterial blood and tumor tissue increase while tumor blood perfusion and bioenergetic status decrease during carbogen breathing may seem contradictory. It appears that this reflects different effects of the O_2 - and CO_2-components of carbogen on the physiology of the host and tumor. As 100 % O_2 breathing alone did not result in a detectable increase of the $[O_2Hb]$ in tumor blood, the observed increase of the latter and the oxygen tension in tumor tissue during carbogen breathing appear to be mediated by the CO_2-component of carbogen. Therefore, we speculate that the CO_2-component of carbogen may have an indirect effect on the $[O_2Hb]$ and the tissue oxygen tension via an inhibition of oxidative energy metabolism. The latter may be explained by two different mechanisms: 1) The CO_2-component has a vasodilating effect on host vessels. When the tumor vasculature lacks responsive smooth musculature and is in parallel to the vasculature of the host tissue, tumor blood perfusion reduces, which is known as the steal phenomenon. This causes a decrease of the substrate supply for oxidative energy metabolism and consequently reduces the O_2-consumption rate of cells. 2) The acidification of tumor tissue may inhibit the glycolytic rate, which can have a similar effect on the O_2-consumption rates of tumor cells.

References

1. Thomlinson RH, Gray LH. The Histological Structure of some Human Lung Cancer and the possible Implications for Radiotherapy. *Br J Cancer* **9**: 539-549 (1955).

2. Denekamp J. Does physiological hypoxia matter in cancer therapy?, in "The Biological Basis of Radiotherapy" (Steel GG, Adams GE, Peckham MJ, Eds.): pp 139-155, Elsevier, Amsterdam, New York, Oxford (1983).

3. Chaplin DJ, Horsman MR, Aoki DS. Nicotinamide, Fluosol DA and Carbogen: A Strategy to Reoxygenate Acutely and Chronically Hypoxic Cells In-vivo. *Br J Cancer* **63**: 109-113 (1991).

4. Honess DJ, Bleehen NM. Perfusion Changes in the RIF-1 Tumor and Normal Tissues after Carbogen and Nicotinamide, Individually and Combined. *Br J Cancer* **71**: 1175-1180 (1995).

5. Fenton BM. The Effects of Carbogen and Nicotinamide on Intravascular Oxyhemoglobin Saturations in SCCVII and KHT Murine Tumors. *Br J Cancer* **71**: 945-949 (1995).

6. Kaanders JHAM, Pop LAM, Marres HAM, Liefers J, van den Hoogen FJA, van Daal WAJ, van der Kogel AJ. Accelerated radiotherapy with carbogen and nicotinamide (ARCON) for laryngeal cancer. *Radiother Oncol* **48**: 115 – 122 (1998).

7. Thews O, Kelleher DK, Vaupel PW. Modulation of Spatial O_2 Tension Distribution in Experimental Tumors by Increasing Arterial O_2 Supply. *Acta Oncologica* **34 (3)**: 291-295 (1995).

8. Hirst DG. Review: Tumor Blood Flow Modifications for Therapeutic Benefit: Is this Approach Ready for Clinical Application? in "The Gray Laboratory Annual Report" (Michael B, Hance M, Eds.): pp. 14-17, Northwood Middlesex, UK (1989).

9. Vaupel PW. Blood Flow, Oxygenation, Tissue pH Distribution and Bioenergetic Status of Tumors, in "Ernst Schering Research Foundation Lecture 23", pp. 13-14, Information and Standards Medical Scientific Publications, Berlin (1994).

10. Zlotecki RA, Baxter LT, Boucher Y, Jain RK. Pharmacologic Modifications of Tumor Blood Flow and Interstitial Fluid Pressure in a Human Tumor Xenograft: Network Analyses and Mechanistic Interpretation. *Microvasc Res* **50(3)**: 429-443 (1995).

11. Dobson GP, Yamamoto E, Hochachka PW. Phosphofructokinase control in muscle: nature and reversal of pH-dependent ATP inhibition. *Am J of Physiology* **250**: R71-R76 (1986).

12. Buchalter SE, Crain MR, Kreisberg R. Regulation of lactate metabolism in-vivo. *Diabetes/Metabolism reviews* **5(4)**: 379 - 391 (1989).

13. Robinson SP, Rodrigues LM, Ojugo ASE, McSheehy PMJ, Howe FA, Griffiths JR. The response to carbogen breathing in experimental tumor models monitored by gradient-recalled echo magnetic resonance imaging. *Br J Cancer* **75(7)**: 1000 - 1006 (1997).

14. Griffiths JR, Taylor NJ, Howe FA, Saunders MI, Robinson SP, Hoskin PJ, Powell MEB, Thoumine M, Caine LA, Baddeley H. The response of human tumors to carbogen breathing, monitored by gradient-recalled echo magnetic resonance imaging. *Int J Radiation Oncology Biol Phys* **39(3)**: 697-701 (1997).

15. Jöbsis FF. Noninvasive, infrared monitoring of cerebral and myocardial oxygen suffiency and circulatory parameters. *Science* **198**: 1264-1267 (1977).

16. Chance B, Borer E, Evans A, Holtom G, Kent J, Maris M, McCully K, Northrop J, Shinkin M. Optical and nuclear magnetic resonance studies of hypoxia in human tissues and tumors. *NY Acad Sci* **551**: 1-16 (1989).

17. Dardzinski BJ, Sotak CH. Rapid Tissue Oxygen Tension Mapping Using ^{19}F Inversion-Recovery Echo-Planar Imaging of Perfluoro-15-Crown-5-Ether. *Mag Res Med* **32**: 88-97 (1994).

18. Su M-Y, Wang Z, Roth GM, Lao X, Samoszuk MK, Nalcioglu O. Pharmacokinetic Changes Induced by Vasomodulators in Kidneys, Livers, Muscles, and Implanted Tumors in Rats as Measured by Dynamic Gd_DTPA-Enhanced MRI. *Mag Res Med* **36**: 868-877 (1996).

19. van der Sanden BPJ, Rijken PFJW, Heerschap A, Bernsen HJJA, van der Kogel AJ. In-vivo ^{31}P-Magnetic Resonance Spectroscopy and Morphometric Analyses of the Perfused Vascular Architecture of Human Glioma Xenografts in Nude Mice. *Br J Cancer* **75(10)**: 1432-1438 (1997).

20. Bernsen HJJA, Rijken PFJW, Oostendorp T, van der Kogel AJ, Vascularity and perfusion of human gliomas xenografted in the athymic nude mouse. *Br J Cancer* **71(4)**: 721-726 (1995).

21. Okada E, Firbank M, Delpy DT. The Effect of Overlying Tissue on the Spatial Sensitivity Profile of Near-Infrared Spectroscopy. *Phys Med Biol* **40**: 2093-2108 (1995).

22. Colier WNJM. Near Infrared Spectroscopy: Toy or Tool? : An Investigation on the Clinical Applicability of Near Infrared Spectroscopy. PhD-thesis: pp. 12-16, University of Nijmegen, the Netherlands (1995).

23. van der Sanden BPJ, Heerschap A, Simonetti AW, Rijken PFJW, Peters HPW, Stüben G, van der Kogel AJ. Characterization and validation of noninvasive oxygen tension measurements in human glioma xenografts by ^{19}F-MR relaxometry. *Int J Radiation Oncology Biol Phys*: in press (1999).

24. Silver MS, Joseph RI, Hoult DI. Highly Selective $\pi/2$ and π Pulse Generation. *J Mag Res* **59**: 347-351 (1984).

25. Wedeking P, Eaton S, Covell DG, Nair S, Tweedle MF, Eckelman WC. Pharmacokinetic Analyses of Blood Distribution of Intravenously Administered [153]Gd-Labeled Gd(DTPA)[2-] and [99m]Tc(DTPA) in rats. *Mag Reson Imaging* **8**: 567-575 (1990).

26. Hittmair K, Gomiscek G, Langenberger K, Recht M, Imhof H, Kramer J. Method for the Quantitative Assessment of Contrast Agent Uptake in Dynamic Contrast Enhanced MRI. *Mag Res Med* **31**: 567-571 (1994).

27. van der Sanden BPJ, de Graaf RA, Rijken PFJW, Peters JPW, Heerschap A, Nicolay K, van der Kogel AJ. A Comparative Study of Dynamic [1]H-MRI Studies of Gd_DTPA Uptake, Perfused Vessel Distribution and Hypoxic Areas in Human Glioma Xenografts in "Proc., ISMRM, 5th Annual Meeting, Vancouver, 1997." p. 1087.

28. Okunieff P, Ramsay J, Tokuhiro T, Hitzig BM, Rummeny E, McFarland E, Neuringer LJ, Suit HS. Estimation of Tumor Oxygenation and Metabolic Rate Using ^{31}P-MRS : Correlation of Longitudinal Relaxation with Tumor Growth Rate and DNA Synthesis. *Int J Radiation Oncology Biol Phys* **14**: 1185-1195 (1988).

29. Evelhoch JF, Crowley MG, Ackerman JJH. Signal-to-Noise Optimalization and Observed Volume Localization with Circular Surface Coils. *J of Mag Res* **56**: 110 124 (1984).

30. Moon RB, Richards JH. Determination of Intracellular pH by ^{31}P-Magnetic Resonance. *J Biol Chem* 248: 7276-7280 (1973).

31. Seo Y, Murahami M, Watari H, Imal LY, Yoshizaki K, Nishihawa H, Morimoto T. Intracellular pH Determination by ^{31}P-NMR Technique. *J Biochem* **94**: 729-733 (1983).

32. Altman PL, Dittmer DS. in "Biology Data Book, 2nd Ed., Federation of American Societies for Experimental Biology 3" (Altman PL, Dittmer DS, Eds.): p. 1603, Bethesda, Maryland (1974).

33. Altman PL, Dittmer DS. in "Biology Data Book, 2nd Ed., Federation of American Societies for Experimental Biology 3" (Altman PL, Dittmer DS, Eds.): p. 1594, Bethesda, Maryland (1974).

34. Rijken PFJW, Bernsen HJJA, van der Kogel AJ. Application of an Image Analyses System to the Quantitation of Tumor Perfusion and Vascularity in Human Glioma Xenografts. *Microvascular Res* **50**:141-153 (1995).

35. Belardinelli R, Barstow TJ, Porszasz J, Torrance K. Skeletal muscle oxygenation during constant work rate exercise. *Med Sci Sports Exerc* **27**: 512-519 (1995).

36. Robinson SP, Howe FA, Griffiths JR. Noninvasive Monitoring of Carbogen-Induced Changes in Tumor Blood Flow and Oxygenation by Functional Magnetic Resonance Imaging. *Int J Radiation Oncology Biol Phys* **33(4)**: 855-859 (1995).

37. Howe FA, Robinson SP, Griffiths JR. Modification of Tumor Perfusion and Oxygenation Monitored by Gradient Recalled Echo MRI and ^{31}P MRS. *NMR in Biom* **9**: 208-216 (1996).

38. Torres Filho IP, Leunig M, Yuan F, Intaglietta M, Jain RK. Noninvasive Measurement of Microvascular and Interstitial Oxygen Profiles in Human Tumor in SCID Mice. *Proc Natl Acad Sci USA* **91**: 2081-2085 (1994).

39. Cerniglia GF, Wilson DF, Pawlowski M, Vinogradov S, Biaglow J. Intravascular oxygen distribution in subcutaneous 9L tumors and radiation sensitivity. *J Appl Physiol* **82(6)**: 1939-1945 (1997).

40. Larsson HBW, Stubgaard M, Frederiksen JL, Jensen M, Henriksen O, Paulson OB. Quantitation of Blood-Brain Barrier Defect by Magnetic Resonance Imaging and Gadolinium-DTPA in Patients with Multiple Sclerosis and Brain Tumors. *Mag Res Med* **16**: 117-131 (1990).

41. Tofts PS, Kermode AG. Measurement of the Blood-Brain Barrier Permeability and Leakage Space using Dynamic MR Imaging. 1. Fundamental Concepts. *Mag Res Med* **17**: 357-367 (1991).

42. Dewhirst MW, Ong ET, Rosner GL, Rehmus SW, Shan S, Braun RD, Brizel DM, Secomb TW. Arteriolar oxygenation in tumor and subcutaneous arterioles: effects of inspired air oxygen content. *Br J Cancer* **74 (suppl.)**: S242-S246 (1996).

43. Belfi CA, Paul CR, Shan S, Ngo FQH. Comparison of the Effects of Hydralazine on Tumor and Normal Tissue Blood Perfusion by MRI. *Int J Radiation Oncology Biol Phys* **29(3)**: 473-479 (1994).

44. Koutcher JA, Alfieri AA, Kornblith AB, Devitt ML, Cowburn D, Ballon D, Kim JH. Changes in Radiation Sensitization Induced by Fluosol-DA as Measured by ^{31}P- Nuclear Magnetic Resonance Spectroscopy. *Cancer Res* **50**: 7252-7256 (1990).

45. Hodgkiss RJ, Jones G, Long A, Parrick J, Smith KA, Stratford MRL, Wilson GD. Flow cytometric evaluation of hypoxic cells in solid experimental tumors using fluorescence immunodetection. *Br J Cancer* **63**: 119-125 (1991).

46. Kennedy AS, Raleigh JA, Perez GM, Calkins DP, Thrall DE, Novotny DB, Varia MA. Proliferation and hypoxia in human squamous cell carcinoma of the cervix: First report of combined immunohistochemical assays. *Int J Radiation Oncology Biol Phys* **37(4)**: 897-905 (1997).

47. Stryer L. in "Biochemistry 2nd Ed." (Freeman WH, Eds.): pp. 69-70, New York, San Francisco (1981).

48. Bussink J, Kaanders JHAM, Rijken PFJW, Peters JPW, Hodgkiss RJ, Marres HAM, van der Kogel AJ. Vascular architecture and microenvironmental parameters in human squamous cell carcinoma xenografts: effects of carbogen and nicotinamide. *Radiother Oncol*: in press (1998).

49. Evanochko WT, Sakai TT, Ng TC, Krishna NR, Kim HD, Zeidler RB, Ghanta VK, Brockman RW, Schiffer LM, Braunschweiger PG, Glickson JD. NMR study of *in vivo* RIF-1 tumors: analyses of perchloric acid extracts and identification of 1H, 31P and 13C resonances. *Biochim Biophysic Acta* **805**: 104 - 116 (1984).

Chapter 8

Summary/ Samenvatting

Summary

The aim of the study, described in this thesis, was to analyze physiological and biochemical parameters, which are related to the oxygenation status of human glioma xenografts. Noninvasive magnetic resonance (MR) methods and immunohistochemical analyses of the vascular architecture were used for this purpose. This information is important before the start of a radiotherapy treatment, since local oxygen tensions influence the radiosensitivity of a tumor. Furthermore, MR-techniques may help to develop and test treatment modulations in order to improve the oxygen tension in tumor tissue. The magnetic resonance studies included: 1) the direct analyses of the oxygen tension in tumor tissue, 2) the evaluation of physiological parameters, which determine the supply of oxygen, and finally 3) the analyses of biochemical parameters (e.g. bioenergetic status), which are related to the supply of oxygen. Most MR-experiments were followed by quantitative immunohistochemical analyses of the perfused and total vascular bed, hypoxic cells and necrotic regions. This unique comprehensive approach permits to compare physiological and biochemical parameters with quantitative morphometric analyses.

In **chapter 1**, the different parameters, which affect the local oxygen tension in tumor tissue, and the magnetic resonance methods and other techniques, which have been used in this thesis to probe these parameters are described.

In **chapters 2–4**, the tracer-uptake rates of the clinical *diffusible* tracer Gd and the *freely diffusible* tracer HDO have been analyzed in gliomas growing in rat brain or in the flank of nude mice. The tracer-uptake rate in tumor tissue is related to physiological processes, which determine the supply of oxygen and nutrients (tumor blood perfusion, diffusive transport across the capillary endothelium into the extravascular volume). **Chapter 2** gives a short review of two pharmacokinetic models, which have been used for the interpretation of uptake rates of Gd and HDO in (tumor) tissue. The parameters of these models are only defined in regions with a high-density of perfused microvessels. In these regions, tracer-uptake rates can be related to physiological parameters such as tumor blood perfusion (TBP) and PS_p-product, when pharmacokinetic models are fitted to tracer-uptake curves. The PS-product is a product of the vascular permeability (P) and the total perfused vascular surface-area (S_p), and determines the diffusive transport across the capillary endothelium. In **chapter 3**, Gd-uptake rates were analyzed with a high spatial and temporal resolution in 9L-gliomas growing in rat brain. The uptake rates had a positive correlation with the perfused microvessel density (N_p) and vascular surface-area (S_p). The latter correlation indicates that variations in the TBP and/or vascular permeability did not affect the Gd-uptake rate in these glioma tumors. However, these parameters may still affect the Gd-uptake rate, when they are modulated. For instance, in **chapter 7**, a decrease of the TBP caused a large decline of the Gd-uptake rate. Without modulations of TBP and/or vascular permeability, Gd-uptake studies may be of additional value to pathology in the evaluation of a therapy, if the latter affects the perfused microvessel density or surface-area, such as an anti-angiogenic therapy.

Chapter 4 describes global ^{2}H-MRS studies of HDO-uptake in the total volume of 2 human glioma xenograft lines with a heterogeneously (E49) and homogeneously (E98) perfused vascular architecture. This MR-technique was introduced approximately 10 years ago, to measure tumor blood perfusion, but is difficult to apply in the clinic due to the low MR-sensitivity of ^{2}H-spins and toxicity of high dose HDO. In chapter 4, the uptake of HDO has been measured with a high temporal resolution in the total tumor volume (global), and could not be detected locally in perfused regions of the tumor as in dynamic ^{1}H-MRI studies

of the Gd-uptake. Thus, the time to reach an equilibrium between the HDO concentration in the vascular and extravascular compartment was also controlled by diffusive transport of the tracer from perfused into nonperfused regions of the tumor. These processes were more dominant in heterogeneously perfused tumors with large distances between perfused microvessels. In such tumors, global HDO-uptake studies cannot be used to analyze TBP, but provide information on the diffusion geometry of a tumor. Here, the uptake rate of HDO is related to diffusion-limited supply of oxygen, nutrients and drugs to the tissue.

In general, tracer-uptake studies are related to the perfusion and diffusion-limited supply of oxygen and other substrates. However, direct measurements of the oxygen tension in tissue are still important, because the latter depends on the balance between the oxygen supply and demand of tumor cells, which is determined by the oxygen consumption rates.

Chapter 5 reports the characterization and validation of noninvasive oxygen tension measurements in the human glioma xenograft line E49 with slice-selective ^{19}F-MR relaxometry. The perfluorocarbon compound perfluoro-15-crown-5-ether was used as oxygen sensor. De T_1-relaxation rate of fluor spins in this oxygen sensor has a linear relationship with the local oxygen tension in regions of the tumor, in which the sensor accumulates. The distribution and accumulation of the sensor depends on the mode of injection: e.g. after i.v. injection perfluoro-15-crown-5-ether sequester in the perfused tumor rim. Thus, only in these perfused regions throughout the MR-slice oxygen tension and oxygen tension changes are measured. In perfused regions of the tumor, oxygen tensions as probed by ^{19}F-MR relaxometry were comparable to oxygen tension values as measured with oxygen electrodes (Eppendorf). The latter method is the most frequently applied technique for detection of local and global oxygen tensions, and therefore it was used for validation of the oxygen tensions as detected by ^{19}F-MR relaxometry.

Currently, perfluorocarbon compounds are not available for clinical use, but this situation may change in the near future.

The balance between the oxygen and nutrient supply via blood perfusion and diffusive transport in tissue, and the consumption of oxygen and nutrients by the cells determine the bioenergetic status of a tumor. The P_i/NTP ratio is a measure of the bioenergetic status, and can be detected with ^{31}P-MRS. In heterogeneously perfused tumors many cells are not adjacent to functional capillaries, and have difficulties to maintain their bioenergetic status due to the lack of oxygen and nutrients. Therefore, the aim of the study presented in **chapter 6** was to analyze the correlation between the P_i/NTP ratio of the whole tumor, and distances between perfused capillaries (diffusion geometry) in the same heterogeneously (E49) and homogeneously perfused (E98) tumor lines as examined in other studies (chapter 4). A linear correlation was found between the P_i/NTP ratio and the percentage of intercapillary distances larger than 200 μm. Calculations of the oxygen and glucose gradient length in glioma tissue using the Krogh cylinder model, and immunohistochemical analyses of distances between perfused and chronically hypoxic regions, suggested that the correlation between the P_i/NTP ratio and the percentage of intercapillary distances larger than 200 μm was possibly related to a transition of an aerobic energy metabolism to an anaerobic energy metabolism. The glioma cells with an aerobic energy metabolism tried to maintain their NTP synthesis via an intensified anaerobic glycolysis, which claimed the stock of glucose. These results indicate that the diffusion-limited supply of oxygen (and glucose) is the major determinant of the bioenergetic status in both tumor lines.

In a clinical setting, ^{31}P-MRS measurements can be used to the study the global bioenergetic status of tumor and/or the local bioenergetic status in different regions of large tumor.

In **chapter** 7, the different MR-techniques presented in chapter 4, 5 and 6 were used and combined to study the effect of carbogen (5% CO_2 and 95% O_2) breathing on the physiological profile of the E49 tumor line. Carbogen breathing has been introduced to decrease the fraction of chronically hypoxic cells by increasing the saturation of hemoglobin with oxygen and by increasing the amount of dissolved oxygen in blood plasma. During carbogen breathing, we observed that the oxyhemoglobin concentration in tumor blood and oxygen tensions in arterial blood and tumor tissue increase, while simultaneously tumor blood perfusion and bioenergetic status decrease. It appears that this reflects different effects of the CO_2-component of carbogen on the physiology of the host and the tumor.

We speculated that the CO_2-component of carbogen might have an indirect effect on the [O_2Hb] and the tissue oxygen tension via an inhibition of oxidative energy metabolism. The latter may be explained by two different mechanisms: **1)** The CO_2-component has a vasodilating effect on host vessels. When the tumor vasculature lacks responsive smooth musculature and is in parallel to the vasculature of the host tissue, tumor blood perfusion reduces, which is known as the steal phenomenon. This causes a decrease of the substrate supply for oxidative energy metabolism and consequently reduces the O_2-consumption rate of cells. **2)** The acidification of tumor tissue may inhibit the glycolytic rate, which can have a similar effect on the O_2-consumption rates of tumor cells.

Samenvatting

Het onderzoek dat is beschreven in dit proefschrift had als doel om fysiologische en biochemische parameters te analyseren, die gerelateerd zijn aan de oxygenatie status van primaire hersentumoren (gliomas). Voor dit doel is gebruik gemaakt van niet-invasieve magnetische resonantie (MR) technieken en immunohistochemische analyse methoden. Informatie over deze parameters is belangrijk, omdat lokale zuurstofspanningen de gevoeligheid van een tumor voor radiotherapie mede bepalen. Verder kunnen MR-technieken helpen bij de ontwikkeling en het testen van therapie modulaties, die ingezet kunnen worden voor de verbetering van de zuurstofspanning in tumorweefsel.

De MR-studies omvatten: 1) direkte bepalingen van de zuurstofspanning in tumorweefsel, 2) evaluaties van fysiologische parameters, die de zuurstof aanvoer in tumoren bepalen, en tenslotte 3) analyses van biochemische parameters (bioenergetische status) die gecorreleerd zijn met de aanvoer van zuurstof. De MR-studies werden in de meeste gevallen gevolgd door kwantitatieve immunohistochemische analysen van het geperfundeerde en totale vaatbed, hypoxische cellen en necrotische gebieden. Door deze unieke en uitgebreide aanpak werden fysiologische and biochemische parameters gerelateerd aan kwantitatieve morfologische analyses.

In **hoofdstuk 1** wordt aangeven welke parameters de lokale zuurstofspanning in tumor weefsel bepalen en hoe deze gemeten zijn.

In **hoofdstuk 2 t/m 4** worden tracer-opname studies in gliomas beschreven met diffundeerbare tracers, zoals het klinische contrast middel gadolinium (Gd) en zwaar-water. De tracer-opname snelheid in tumor weefsel is gerelateerd aan fysiologische processen, die de zuurstof en nutriënten aanvoer bepalen (bloed perfusie, diffusie transport over vaatendotheel naar extravasculaire ruimte). **Hoofdstuk 2** geeft een overzicht van twee farmacokinetische modellen, die gebruikt zijn bij de interpretatie van de opname snelheden van Gd en zwaar-water in (tumor)weefsel. De parameters van deze farmacokinetische modellen zijn alleen bepaald in regio's met een hoge dichtheid van geperfundeerde capillairen. Door een farmacokinetisch model te fitten aan een tracer-opname curve kunnen snelheidsconstanten van de curve gerelateerd worden aan fysiologische parameters, zoals tumor bloed perfusie (TBP) en het PS_p-product. De laatste parameter is een product van de vaatpermeabiliteit (P) en het totale geperfundeerde vaatoppervlak (S_p), en bepaalt de tracer transportsnelheid door het vaatendotheel. In **hoofdstuk 3,** werden Gd-opname snelheden in 9L-glioma tumoren in ratten hersenen geanalyseerd met een hoge temporele en ruimtelijke resolutie. De opname snelheid van Gd heeft een positieve correlatie met de geperfundeerde vaatdichtheid (N_p) en geperfundeerde vaatoppervlak (S_p). De laatste correlatie duidt erop dat variaties in de TBP en vaatpermeabiliteit (P) geen invloed hebben op de opname snelheid van Gd in deze gliomas. Echter, dat wil niet zeggen dat deze parameters niet de Gd-opname snelheid kunnen bepalen wanneer ze veranderd zouden worden. In *hoofdstuk 7* werd een sterke afname van de Gd-opname snelheid veroorzaakt door een afname van de TBP. Zonder modulaties kunnen niet-invasieve Gd-opname studies in aanvulling op pathologisch onderzoek gebruikt worden om de effecten van een tumor therapie te meten, wanneer deze alleen invloed heeft op de geperfundeerde vaatdichtheid en oppervlak, zoals een anti-angiogenese therapie.

Hoofdstuk 4 beschrijft globale ^{2}H-MRS studies van zwaar-water (HDO) opname in het totale volume van 2 humane glioma xenograft lijnen met een heterogeen (E49) en homogeen (E98) geperfundeerde vaatverdeling. Deze MR-techniek werd ongeveer 10 jaar geleden geïntroduceerd om bloed perfusie te meten in tumoren, maar is ongeschikt voor klinische toepassingen o.a. door de lage MR-gevoeligheid van deuterium spins en de toxiciteit van HDO bij hoge dosis. Door de lage MR-gevoeligheid kon alleen de totale opname van HDO in het totale tumor volume (globaal) gemeten worden met een hoge temporele resolutie door gebruik van ^{2}H-MRS. Dus de opname van HDO kon niet lokaal gemeten worden in geperfundeerde gebieden van de tumor met een hoge ruimtelijke en temporele resolutie, zoals bij dynamische ^{1}H-MRI studies van de Gd-opname. Daarom werd de tijd om evenwicht te bereiken tussen de concentratie van HDO in de vasculaire en extravasculaire ruimte van het tumor weefsel ook bepaald door diffusie transport processen van de tracer vanuit geperfundeerde tumor gebieden naar niet-geperfundeerde gebieden. Deze processen speelde een grote rol in heterogeen geperfundeerde tumoren met lange diffusie afstanden tussen de geperfundeerde vaten. In deze tumoren, kan deze MR-techniek zeker niet gebruikt worden om bloed perfusie te meten, maar geeft wel inzicht in de diffusie geometrie van een tumor. De opname snelheid van HDO is gerelateerd aan diffusie-gelimiteerde opname van zuurstof, nutriënten en drugs in tumorweefsel.

In het algemeen geven tracer-opname studies indirect informatie over de aanvoer van zuurstof en substraten naar tumorweefsel. Echter directe bepalingen van de zuurstofspanning in weefsel blijven belangrijk, omdat deze niet alleen bepaald wordt door de zuurstof aanvoer, maar ook door de zuurstof vraag van de cellen ofwel zuurstof consumptie.

Hoofdstuk 5 beschrijft de karakterisatie en validatie van niet-invasieve zuurstofspanning metingen in de humaan glioma xenograft lijn E49 met behulp van plak-selektieve ^{19}F-MR relaxometrie studies, waarbij perfluoro-15-crown-5-ether als zuurstofsensor was gebruikt. De T_1-relaxatie snelheid (T_1^{-1}) van fluor spins van deze zuurstofsensor heeft een linaire relatie met de lokale zuurstofspanning in tumor gebieden waar deze sensor ophoopt. Deze ophoping is afhankelijk van de manier waarop injectie plaatst vindt. Bijvoorbeeld, perfluoro-15-crown-5-ether accumuleerde 3 dagen na i.v. injectie in geperfundeerde gebieden aan de rand van de tumor, zodat alleen in deze gebieden (verdeeld over de MR-plak) zuurstofspanningen of veranderingen in zuurstofspanningen gemeten kunnen worden (hoofdstuk 7). In geperfundeerde gebieden waren zuurstofspanningen, zoals gemeten met ^{19}F-MR relaxometrie, vergelijkbaar met zuurstofspanningen gemeten met Eppendorf O_2-elektroden. Deze laatste techniek wordt het meest gehanteerd om lokale zuurstofspanningen te meten en is daarom gebruikt om de zuurstofspanningen van de ^{19}F-MR relaxometrie metingen te valideren.

Op dit moment zijn er nog geen zuurstofsensoren beschikbaar voor klinische toepassingen, maar verwacht wordt dat dit in de toekomst wel het geval zal zijn.

De balans tussen zuurstof en nutriënten aanvoer via bloed perfusie en diffusie transport in weefsel, en de consumptie van zuurstof en nutriënten door cellen bepaalt de bioenergetische status van een tumor. De P_i/NTP ratio is een maat voor de bioenergetische status van een tumor en kan bepaald worden met ^{31}P-MRS.

In heterogeen geperfundeerde tumoren, waarbij grote populaties cellen ver verwijderd zijn van functionele vaten, hebben veel cellen mogelijk moeite met het handhaven van hun bioenergetische status door gebrek aan zuurstof en substraten voor het energie metabolisme. Daarom werd in **hoofdstuk 6** een correlatie onderzocht tussen P_i/NTP ratio van de hele tumor en intercapillairen afstanden tussen geperfundeerde capillairen (diffusie geometrie) in dezelfde heterogeen (E49) en meer homogeen geperfundeerde (E98) tumor lijnen uit hoofdstuk 4. Er werd een lineaire correlatie gevonden tussen de P_i/NTP ratio en het percentage intercapillaire afstanden boven de 200 μm. Door berekeningen van diffusie afstanden van zuurstof en glucose in glioma weefsel met behulp van een Krogh cilinder model en immunohistochemische analyses van afstanden tussen geperfundeerde gebieden en chronisch hypoxische gebieden, kon aannemelijk worden gemaakt dat de correlatie tussen de P_i/NTP ratio en het percentage intercapillaire afstanden boven de 200 μm mogelijk te maken heeft met een overgang van een aëroob naar anaëroob energie metabolisme. De glioma cellen met een aëroob energie metabolisme proberen waarschijnlijk de NTP synthese te handhaven via anaërobe glycolyse, waardoor de glucose voorraad sneller afneemt. Blijkbaar is diffusie-gelimiteerde opname van zuurstof (en glucose) de belangrijkste factor voor het handhaven van de bioenergetische status in de bestudeerde tumorlijnen.

In de kliniek zijn ^{31}P-MRS experimenten bruikbaar voor de bestudering van de globale bioenergetische status van een tumor, maar ook in voornamelijk grote tumoren kunnen lokale gebieden geanalyseerd worden.

In **hoofdstuk 7** zijn de MR-technieken uit de hoofdstukken 4, 5 en 6 gebruikt en gecombineerd om de effecten van carbogeen (5% CO_2, 95% O_2) beademing op het fysiologische profiel van tumorlijn E49 te bestuderen. Carbogeen beademing werd geïntroduceerd met het doel om de fractie chronisch hypoxische cellen te laten afnemen door de hemoglobine saturatie met zuurstof en de hoeveelheid opgeloste zuurstof in het bloed plasma te verhogen. Tijdens carbogeen beademing, werd een toename gevonden van de oxyhemoglobine concentratie in tumor bloed en de zuurstofspanningen in weefsel, tegelijkertijd namen de tumor bloed perfusie en de bioenergetische status af. Het bleek dat dit veroorzaakt werd door verschillende effecten van de CO_2-component van carbogeen op de fysiologie van de gastheer en de tumor.

We speculeerde dat de CO_2-component van carbogeen mogelijk een indirect effect heeft op de oxyhemoglobine concentratie en de weefsel oxygenatie via een remming van de oxidatieve ademhaling. Dit werd uitgelegd via twee verschillende mechanisme: **1)** De CO_2-component heeft een vasodilaterende werking op de vaten van het gastweefsel. Wanneer de vaten van de tumor niet kunnen reageren op de CO_2-component en wanneer ze parallel lopen met het vaatbed van de gastheer, dan zal de tumor bloed perfusie afnemen door een zogenaamd "steal effect" (bloed wordt gestolen uit de tumorvaten). Dit veroorzaakt een daling van substraat aanvoer voor het oxidatieve energie metabolisme en resulteert logische wijze in een afname van de zuurstofconsumptie van de tumorcellen. **2)** De verzuring van het tumor weefsel kan mogelijk de glycolyse snelheid remmen wat eenzelfde effect heeft op de zuurstofconsumptie snelheid van de tumorcellen.

Scheikunde faculteit KUN, Vakgroep Biofysische Chemie.
Voordat we eind 1997 de beschikking kregen over een horizontale *in vivo* NMR opstelling, hebben we veel gewerkt in de biofysische chemie groep van Prof. Dr. Cees Hilbers. Binnen deze groep, wil ik graag Jan van Os bedanken voor het in de lucht houden van de oude 200 MHz Bruker spectrometer. Je kent NMR spectrometers door en door en je hebt me vele malen geholpen bij technische problemen. Gerda Nachtegaal en Jos Joordens hartelijk dank voor jullie hulp bij de sequentie programmering en de dataverwerking. Als laatste wil ik ook Prof. Cees Hilbers bedanken voor alle rand voorwaarden, die hij heeft geschapen om *in vivo* NMR mogelijk te maken in een *in vitro* NMR groep.

Medische faculteit KUN, Vakgroep Fysiologie.
Bij de interpretatie van de *in vivo* NMR data heb ik gelukkig veel ondersteuning gehad van Dr. Louis Hoofd van de afdeling fysiologie. Beste Louis, hartelijk dank voor jouw hulp bij voornamelijk de contrast-opname studies. Je hebt me een goed gevoel gegeven over de fysiologische parameters, die de opname van contrast middelen in weefsel kunnen bepalen en tegelijkertijd heb je me altijd de beperkingen van de modellen voorgehouden. Beste Dr. Willy Colier, ik wil jou hartelijk bedanken voor jouw ondersteuning bij de 'near-infrared spectroscopy' metingen en de discussies over de zin en onzin van het commentaar van referenten op onze metingen. Verder wil ik zeker Jos Evers niet vergeten te bedanken voor alle ondersteuning bij bloed en NIRS analyses.

Utrecht

***In vivo* NMR faciliteit van het Bijvoet centrum RUU, Vakgroep Scheikunde.**
Beste Prof. Dr. Klaas Nicolay, hartelijk dank voor jouw hulp bij de MR-metingen op jullie afdeling en de snelle, goede bijdragen aan de correcties van artikelen. Verder wil ik de volgende mensen bedanken voor hun samenwerking en intensieve begeleiding: Dr. Robin de Graaf, Dr. Annette van der Toorn, Koos Tamminga, Gerard van Vliet en Henk-Jan Muller.

Delft

Technische Natuurkunde TUD, Vakgroep Spin-imaging.
Beste Dr. Wim Bovée en Dr. Tom Rozijn, op het laatste moment is het ons toch gelukt om alle voorwaarden voor goede NMR studies aan het intracerebrale glioma rat te verenigen. Ik wil jullie hartelijk bedanken voor de goede ondersteuning en werk sfeer, waarbij we altijd ons best deden om elkaar te begrijpen. Van jullie grondige en professionele aanpak heb ik veel geleerd. Wim, verder bedankt voor het nauwkeurig en snel corrigeren van dit boekje als lid van de manuscriptcommissie. Je hebt er nog veel onnauwkeurigheden en fouten uit kunnen halen.

Buitenland
- Department of Radiation Oncology and Toxicology, UNC school of Medicine, Chapel Hill, NC, USA.
Dear Prof. Jim Raleigh, we thank you for kindly providing the bioreductive chemical probe PIMO and the scientific discussions on the results of the immunohistochemical staining experiments.
- Brookhaven National Laboratory, Upton, New York, USA. Dear Dr. Jeffrey A. Coderre, you made the first experiments on the 9L-glioma tumors growing in Fischer rats possible. Thank you!
- CRC Gray Laboratory, Mount Vernon Hospital, Northwood, Middlesex, UK. Dear Dr. Richard Hodgkiss, thank you for your bioreductive chemical probe NITP, which was very valuable for our first staining experiments of hypoxic cells.
- Department of Radiotherapy, University Hospital Essen, Germany. Dear Dr. Georg Stüben, thanks for your help with the Eppendorf O_2-electrode measurements, and the useful discussions on our paper presented in chapter 5.

Institut Curie, Biophysique Moléculaire, Orsay, France
 Chers Dr. J-M. Lhoste et Dr. Andreas Volk, je ne pourrais pas terminer cette thèse sans vous adresser quelques mots. Vous m'avez appris les méthodes de la RMN *in vivo*. Cette formation a été à la base de mes recherches à Nimègue et de la rédaction de ce livre. Je vous remercie et je n'oublierai jamais votre part dans ma formation.

Lieve ouders, Maarten, verdere familie en vrienden, vele dank voor alle steun, belangstelling en begrip in de afgelopen jaren.

Tenslotte, lieve Nathalie, de GT's hebben eindelijk hun boekjes af. Je bent de afgelopen jaren onmisbaar voor mij geweest. Je hielp me bij het relativeren van het werk en de nodige ontspanning. We zijn onze promoties uiteindelijk gaan zien als een normale baan met vele mogelijkheden en kansen. We hebben er veel benut en het beste tussen ons naar boven gehaald.

Boudewijn Petrus Johannes van der Sanden was born on February 23st 1965 in Tilburg, the Netherlands. He grew up in Nijmegen and Den Bosch, where he graduated from High School (Atheneum B, Jeroen Bosch College, Den Bosch) in 1984. In the same year, he started the study (Cell) Biology at the Agriculture University of Wageningen. Where, he obtained his master degree in Biochemistry and Plant Cell Biology in 1990. From Januari 1990 to October 1991, he worked as a junior scientist at the Department of Molecular Biophysics (INSERM U.350) at the Cancer Institute Curie in Paris. Here, Dr. A. Volk and Dr. J-M Lhoste trained him in *in vivo* Magnetic Resonance Spectroscopy on tumors.

In November 1990, he married with Nathalie S.L. Piva in Dives sur Mer, France.

In octobre 1991, they moved to Maarssen, the Netherlands and he became a member of the Clinical and Experimental Magnetic Resonance Spectroscopy group of Prof. Dr. A. Heerschap at the Department of Radiology at the Academic Hospital Nijmegen. He worked as a KWF-fellow on the project entitled 'Prediction and Evaluation of the Radiation Response of Gliomas by Magnetic Resonance Spectroscopy and its Correlation with Tumor Vascularization'. This project was the result of a collaboration with the Radiobiology group of Prof. Dr. A.J. van der Kogel at the Department of Radiotherapy. The project was prolonged in februari 1996 until februari 2000. Most results of both projects are descibed in this PhD-thesis.

B.P.J. van der Sanden, P.F.J.W. Rijken, A. Heerschap, H.J.J.A. Bernsen and A.J. van der Kogel. In vivo ^{31}P magnetic resonance spectroscopy and morphometric analyses of the perfused vascular architecture of human glioma xenografts in nude mice. *British Journal of Cancer* **75(10):** 1432 - 1438, 1997.

W.M.M.J. Bovée, T.H. Rozijn, **B.P.J. van der Sanden** and A. Heerschap. NMR perfusion and metabolic imaging and some examples on brain tumors. *Cellular and Molecular Biology* **43(5):** 675 – 689 (1997).

T.H. Rozijn, **B.P.J. van der Sanden**, A. Heerschap, J.H.N. Creyghton and W.M.M.J. Bovée. Influence of the pharmacokinetic model on the quantification of the Gd-DTPA uptake rate in brain tumors using direct T_1 measurements. *Magnetic Resonance Materials in Biology, Physics and Medicine (MAGMA)* **6**: 37 – 43 (1998).

B.P.J. van der Sanden, A. Heerschap, L. Hoofd, A.W. Simonetti, K. Nicolay, A. van der Toorn, W.N.J.M. Colier and A.J. van der Kogel. Effect of Carbogen Breathing on the Physiological Profile of Human Glioma Xenografts. *Magnetic Resonance in Medicine*: in press (1999).

B.P.J. van der Sanden, H.J.A. in 't Zandt, L. Hoofd, R.A. de Graaf, K. Nicolay, P.F.J.W. Rijken, A.J. van der Kogel and A. Heerschap. Global HDO-uptake as measured by ^{2}H-MRS is related to the perfused capillary distribution in Human Glioma Xenografts. Submitted for publication, 1999.

B.P.J. van der Sanden, A. Heerschap, A.W. Simonetti, P.F.J.W. Rijken, H.P.W. Peters, Georg Stüben and A.J. van der Kogel. Characterization and validation of noninvasive oxygen tension measurements in human glioma xenografts by ^{19}F-MR relaxometry.
International Journal of Radiation Oncology Biology Physics: in press (1999).

B.P.J. van der Sanden, T.H. Rozijn, P.F.J.W. Rijken, H.P.W. Peters, A. Heerschap, A.J. van der Kogel and W.M.M.J. Bovée. Gd_DTPA-uptake rates are linearly related to the perfused microvessel density and surface-area in 9L-glioma in rat brain. Submitted for publication, 1999.